Master's thesis

NTNU
Norwegian University of Science and Technology
Faculty of Natural Sciences
Department of Physics

Prestegård, Astrid

Shape Dependency in Functionalization of Gold Nanoparticles for Biosensing Applications

Master's thesis in Applied Physics and Mathematics
Supervisor: Ruth Catharina de Lange Davies
Co-supervisor: Sulalit Bandyopadhyay and Katharina Zürbes
July 2022

NTNU
Norwegian University of
Science and Technology

Prestegård, Astrid

Shape Dependency in Functionalization of Gold Nanoparticles for Biosensing Applications

Master's thesis in Applied Physics and Mathematics
Supervisor: Ruth Catharina de Lange Davies
Co-supervisor: Sulalit Bandyopadhyay and Katharina Zürbes
July 2022

Norwegian University of Science and Technology
Faculty of Natural Sciences
Department of Physics

NTNU
Norwegian University of
Science and Technology

Preface and Acknowledgements

This thesis marks the end of my master's degree in Applied Physics and Mathematics at the Norwegian University of Science and Technology (NTNU), Trondheim. The work was carried out spring of 2022 in collaboration with The Department of Chemical Engineering and The Particle Engineering Research Centre. All experimental work was performed at the Particle Engineering Core Facilities at the Department of Chemical Engineering and in the cleanroom facilities of NTNU NanoLab.

First, I want to thank my team of supervisors for guiding me through the long and very educational process of writing a master's thesis. A big thank you to Sulalit Bandyopadhyay for sharing your knowledge and for your time and guidance throughout this thesis. Thank you to my co-supervisor, Katharina Zürbes. I appreciate our fruitful discussions, your valuable feedback and practical tips in the labs, and especially your moral support. A great thanks also go to the other members of the Particle Engineering and Hydrometallurgy Research team, and especially to Karthik Ranghutan, Hammad Farooq, Nesrine Bali, and Muhammad Bilal. It's been inspiring to be part of an interdisciplinary research team with such talented researchers and fellow master's students. I value the feedback and discussions I have had with many of you.

I also would like to thank Ruth Catharina de Lange Davies for being my internal supervisor from the Department of Physics, allowing me to perform my master's thesis with the Department of Chemical Engineering.

Finally, I want to thank my friends, family, the house mates of Gløshaugveien 3B, and office mates for supporting me through this process.

Astrid Prestegård
Trondheim, July 2022

Abstract

The COVID-19 pandemic demonstrated the need for robust, affordable, and reliable biosensors. Anisotropic Au NPs show remarkable plasmonic properties and are therefore considered strong candidates for improving today's biosensor technology. Such anisotropic Au NPs can be synthesized using the seed-mediated growth synthesis route. The method employs CTAB surfactant in a two-step method, in which seeds are synthesized in the first step under high supersaturation and grown further under milder supersaturation into anisotropic shapes. However, the resulting Au NPs need to be surface functionalized for tailoring them for specific applications. Understanding the effect of surface functionalization on the physicochemical properties and developing surface functionalization methods are therefore vital for improving biosensor technology. The overall aim of the thesis was to contribute to the understanding of surface functionalization of CTAB coated Au NPs, and especially investigate if it followed any shape-dependent trends.

First, four different Au NPs were synthesized and characterized using a CTAB-mediated seeded growth synthesis route. In addition, one citrate-coated Au NPs were synthesized with Turkevich method for comparison.

Then the determination of Au concentration with MP-AES, Zetaview, and UV-vis was studied. Concentration metrics could be an improved way of adapting surface functionalization protocols to new samples. With MP-AES, Au concentration showed a maximum standard deviation of $0.01 mg/ml$ and was limited by polydispersity and inhomogeneous dispersions within the sample. With UV-vis, Au concentration could be determined from the absorbance at 400 nm when Au NPs had similar sizes and surface chemistries.

Hydrodynamic diameter is a convenient tool to monitor surface chemistry changes. A robust protocol for reproducible measurements of anisotropic Au NPs was therefore needed. A study of two rod-shaped Au NPs at various dilutions and detection angles

showed that it is crucial to get to know the sample of interest and indicated that surfactant stabilized Au NPs should be measured at lowest possible dilution factor.

A two-step PEG and MUA functionalization protocol were then optimized and checked for reproducibility using rod-shaped Au NPs with an aim to replace the CTAB on the surface of the NPs. The highest yield and largest change in zeta potential were found using 2.56 mg/ml PEG and 20 mM MUA. These conditions were applied to the five Au NPs, and no clear shape dependencies were found. The thesis also discusses if better preservation of LSPR-peaks is possible or if the different axes of rotations due to anisotropy, non-uniform coating, size enlargement, and the polydispersity of the samples make it impossible. Further studies of colloidal stability, the reactivity of carboxy groups, and sonication methods were suggested.

Finally, the Au NPs were biotinylated and applied in a model biosensing system with streptavidin. No signs of aggregation with increasing amounts of streptavidin were found for spherical Au NPs. In contrast, a maximum shift of 13 nm was found in the longitudinal LSPR-peak position when 75 nM Streptavidin was added to the rod-shaped Au NPs. The study indicated that the model biosensing system could become a valuable tool for testing and researching the refractive index sensitivity of Au NPs with carboxyl groups if further optimized. Results indicate that further optimalization should focus on improving the colloidal stability of the Au NPs in buffer solution. This could include researching the binding strength of PEG and MUA to the Au NPs.

Sammendrag

Covid-19 pandemien har demonstrert nødvendigheten av billige, robuste og sensitive biosensorer. Gull-nanopartikler av anisotrope former har unike optiske egenskaper, og har derfor potensiale til å radikalt forbedre dagens biosensor teknologi. For å fremstille slike partikler står «Seed mediated growth» frem som en anerkjent og effektiv metode. Dessverre har de fremstilte partiklene CTAB på overflaten, noe som gir utfordringer med stabilitet i anvendelser. Nanopartiklene må derfor funksjonaliseres videre. Bedre forståelse av hvordan overflate-funksjonalisering endrer egenskapene til gull nanopartikler, og utvikling av robuste og effektive metoder for overflate-funksjonalisering er derfor viktig for fremskritt i biosensor teknologi. Hovedmålet i denne masteroppgaven er å bidra til forståelsen av overflate funksjonalisering av CTAB-belagte Gull-Nanopartikler, og spesielt undersøke om funksjonaliseringen avhenger av formen til partiklene.

Først ble fire gull-nanopartikkel prøver fremstilt og karakterisert ved å bruke «CTAB-mediated seeded growth synthesis route». I tillegg ble en citrate-belagt gull-nanopartikkel prøve fremstilt ved Turkeivch metode.

Deretter ble karakterisering av konsentrasjon med metodene MP-AES, Zetaview og UV-vis studert. Ulike måleenheter for konsentrasjons kan være en forbedret måte å tilpasse overflate funksjonaliserings protokoller til nye nanopartikkel prøver. MP-AES viste et maksimalt standard avvik på 0.01 mg/ml, og oppløsningen var begrenset av polydisersitet og inhomogene dispersjoner i prøvene. UV-Vis kunne brukes til å måle konsentrasjon når nanopartiklene hadde lik størrelse og overflatekjemi. Hydrodynamisk diameter er et praktisk verktøy for å overvåke hvordan overflatekjemien endrer seg. En robust protokoll for reproduserbare målinger av anisotrope gull nanopartikler var derfor av interesse. To stavformede nanopartikkel prøver ble derfor målt ved ulike fortynninger og deteksjonsvinkler, og studien konkluderte med surfaktant stabiliserte nanopartikler bør måles med lavest mulig fortynningsfaktor for mest mulig reproduserbare målinger.

En to trinns protokoll for PEG and MUA overfalte funksjonalisering ble optimalisert

ved å bruke stavformede gull nanopartikler. Målet var å erstatte CTABen på overflaten med PEG. Den høyeste effektiviteten ble funnet ved bruk av 2.56 mg/ml PEG og 20 mM MUA. Denne protokollen ble anvendt på de fem gull nanopartiklene. Det ble ikke påvist noen avhengighet til form. Oppgaven diskuterer om det er mulig å ta bedre vare på de optiske «LSPR»-egenskapene til prøvene, eller om uhomogen overflate funksjonalisering, økt størrelse og polydispersitet gjør dette umulig. Videre studier av stabilitet, reaktiviteten til karboksylgruppene og sonikerings metoder ble foreslått.

Til slutt ble biotin bundet til de funksjonaliserte gull nanopartiklene, og testet i et modell biosensor system med streptavidin. Runde gullnanopartikler viste ingen tegn til aggregering ved økende mengder streptavidin. Til forskjell viste stavformede nanopartikler et maksimalt rødskift på 13 nm i den longitudinale «LSPR-peak»-en ved 75 nM streptavidin. Dette indikerer at modell biosensor systemet kan bli et verdifullt verktøy for testing av refraktiv indeks sensitivitet for karboksyl funksjonaliserte gull nanopartikler. Resultatene i studien tilsa at forbedring av partiklenes stabilitet i buffer bør være hovedfokuset i videre utvikling. Dette bør inneholde forskning på bindingsstyrken av PEG og MUA til gull-nanopartiklene.

Acronyms and Abbrevations

Abs_{400}	Absorbance at 400 nm
$AgNO_3$	Silver nitrate
AsA	Ascorbic Acid
Au	Gold
CTAB	Hexadecyltrimethylammonium bromide
DLS	Dynamic Ligth Scattering
ELS	Electrophoretic Light Scattering
FCC	Face Center Cubic
$HAuCl_4$	Chloroauric acid
ICP-MS	Inductively Coupled Plasma Mass Spectrometry
LSPR	Localized Surface Plasmon Resonance
MP-AES	Microwave Plasma Atomic Emission Spectrometer
MUA	11-Mercaptoundecanoic-acid
$NABH_4$	Sodium Borohydride
NPs	Nanoparticles
NRs	Nanorods
NSs	Nanospheres
OA	Oleic Acid
PB	Phosphate Buffer
PBT	Phosephate Buffered Tween
PEG	Poly(ethylene glycol)
PTA	Particle Tracking Analysis
rpm	Rounds per minute
SEM	Scanning Electron Microscope
STEM	Scanning Transmission Electron Microscope
TA	Tannic Acid
TEM	Transmission Electron Microscope
UV-Vis	Ultraviolet–Visible Spectroscopy
ZP	Zeta potential

Contents

1 Introduction

1.1 Motivation

In the last two years, we have lived through the coronavirus pandemic. The novel virus, COVID-19, was first identified in Wuhan, China, in December of 2019 and would later spread across the globe. The respiratory virus seemed unstoppable and gave symptoms ranging from undetectable to deathly. According to World Health Organization, the virus has, as of June 2022, caused more than 6.3 million deaths, making it one of the deadliest viruses in history[1]. Testing, quarantine, and isolation have been critical strategies to stop the spread of the virus, clearly illustrating how vital it is to have quick and reliable covid-tests. This is further shown in a statistical study by *Terriau et al.* looking at the correlation between mortality and test rates in different regions of mainland France[2]. The study concludes that three fewer deaths were observed for each additional 2000 covid-tests conducted.

Covid tests are just one example of a biosensor and why biosensors are important. A biosensor is defined as a device that converts a biological response into a measurable signal[3]. The first biosensor, an oxygen detection device, was invented in 1956 by Clarks[4], and biosensors have since then evolved to become a vital part of our everyday lives. Other well-known examples of biosensors are pregnancy tests and glucose monitoring sensors. However, the biosensor also finds application in drug discovery, biomedicine, diagnostics, food safety, environmental monitoring, and more[5].

In the quest to make better biosensors, many look towards nanomaterials and Gold (Au) Nanoparticles (NPs) in particular. Nanomaterials, in general, have the advantage of high surface area, allowing them to bind an increased amount of bioreceptor unit on the surface[5]. Au NPs are recognized for their biocompatibility, optical, and electrical characteristics, as well as relatively simple synthesis and modification.[6]. This has allowed for biosensors with detection limits down to picomolar scale[7].

The most sensitive optical properties can be found in Au NPs of anisotropic shapes, such as rods[3]. The first version of the seed-mediated growth synthesis method to make such anisotropic Au NPs was published in 2001 by Jana et al.[8]. Over the last twenty years, the method has been extensively studied by numerous research groups, modifying the method to synthesize Au NPs in an extensive range of shapes and sizes with high yield, promising for numerous biomedical applications. The method utilizes CTAB-surfactant as a "shape-directing" reactant to control particle shape, and also as a stabilizer to protect the final particles from aggregation[7]. However, surface functionalization with CTAB causes a challenge for the applications; NPs are only stable when suspended in an aqueous CTAB solution at low pH[7]. Furthermore, it has been shown that excess CTAB molecules are cytotoxic, making them unsuitable for *in vivo* applications. Surface functionalization is therefore needed for further applications.

This thesis studies functionalization with PEG and MUA of CTAB coated Gold NPs of five different shapes and sizes. The surface functionalization of gold NPs affects the properties of the NPs. The overall aim of the thesis was to contribute to the understanding of surface functionalization of CTAB coated Au NPs, and especially investigate if it follows any shape-dependent trends.

1.2 Research Objectives

In order to learn more about shape dependency in functionalization of Au NPs, five main research milestones were set;

1. Synthesize Au NPs of different shapes
2. Optimize robust protocols for characterization of hydrodynamic diameter for anisotropic Au NPs with Dynamic Light Scattering (DLS)
3. Develop and compare methods for determination of concentration of Au NPs
4. Optimize and apply protocol for surface functionalization with PEG and MUA
5. Test and compare biosensing properties for PEG/MUA functionalized Au NPs of different shapes in a model biosensing system with Biotin and Streptavidin

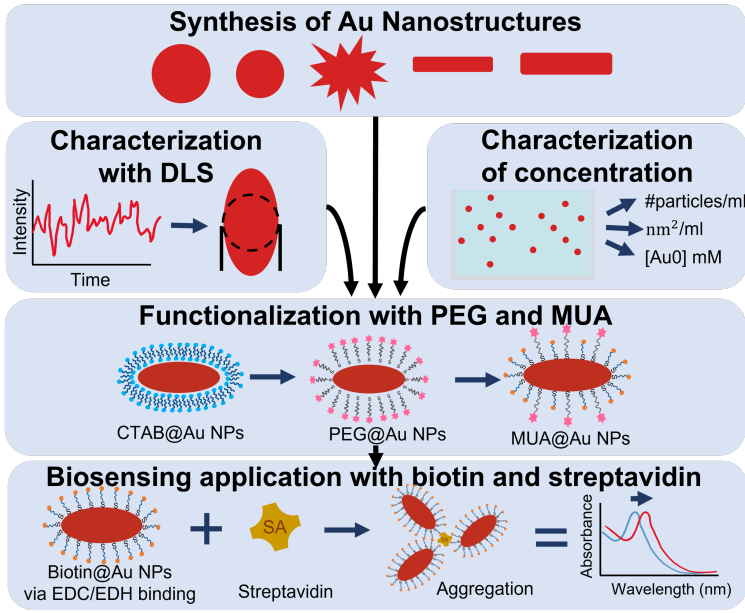

Figure 1.2.1: Reasearch objectives illustrated.

2 Theoretical Framework and Literature Review

This chapter will establish the theoretical framework needed to understand this work and put it into the context of previous works. The first sections will establish key concepts of Au NPs, such as their physiochemical properties and synthesis methods. Next, the characterization of Au NPs will be described, and challenges in characterization with Dynamic Light Scattering and of concentration is discussed. Then, previous work in litterature on surface functionalization is outlined, and discussed. The last part of this chapter will present key concepts of biosensing applications, with a particular focus on the model biosensing system tested in this thesis.

2.1 Gold Nanoparticles

The Offical Jornal of European Union (2011/696/EU), classifies a material as "nanomaterial" or "nanoparticle", if it contains particles in unbound state, and at least 50% of the particles making up the material has one or more dimension in the range of 1 - 100 nm. Materials of this scale have properties remarkably different from the properties of the same element in bulk. At the nanoscale, quantum effects dominate the physiochemical properties, and classical mechanics turn insufficient in describing the behavior of the particles[5]. As a result, properties, such as melting point, fluorescence, electrical conductivity, magnetic permeability, and chemical reactivity, turn shape and size-dependent.

The small size and tunable properties give NPs of different materials extensive applications. Nanoparticles are typically classified into metal NPs, ceramic NPs, and polymeric NPs. This thesis studies metallic nanoparticles made of gold element. Gold

NPs are especially recognized for unique optical properties, stability, biocompatibility, straightforward surface modification, and relatively easy synthesis prosedure[6].

2.1.1 Plasmonic Properties

A very distinct feature of Au NPs is the strong color difference between samples of NPs with different shapes and sizes. Figure 2.1.1 show the color of three different Au NP samples synthesized in this thesis; 20 nm spherical NPs giving the ruby color on the top, rods giving a brown color in the middle, and 55 nm spiky particles giving a grey sample solution on the bottom. These unique optical properties of Au NPs arise from the local surface plasmon resonance effect (LSPR).

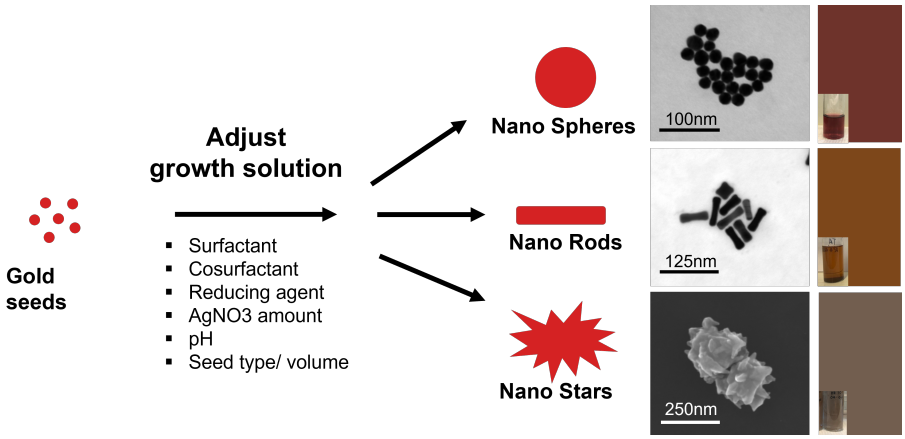

Figure 2.1.1: Changes in the growth solution of the seed-mediated growth synthesis route can give Au NPs of a wide range of sizes and shapes. Illustration made after inspiration from graphical abstract in [9] and Figure 7 in [10].

LSPR-effect is observed in nanomaterials of all noble materials. The noble materials have highly conductive free surface electrons. When incident light of a specific frequency interacts with the NPs, it will induce a collective coherent oscillation of these free surface electrons, leading to an enhanced electric field on the surface and, as a result, strong absorption of light at this specific frequency. For Au NPs, the wavelength where this LSPR-peak is observed is dependent on the shape, size, and dielectric environment of the NP-solution[11]. The main difference is seen between NPs of isotropic shapes, for example, spheres, and anisotropic shapes, for example, rods. Figure 2.1.2 illustrates this difference. The anisotropic particles have more than one axis for resonance oscillations to occur and show, as a result, two or more peaks in the absorption spectra.

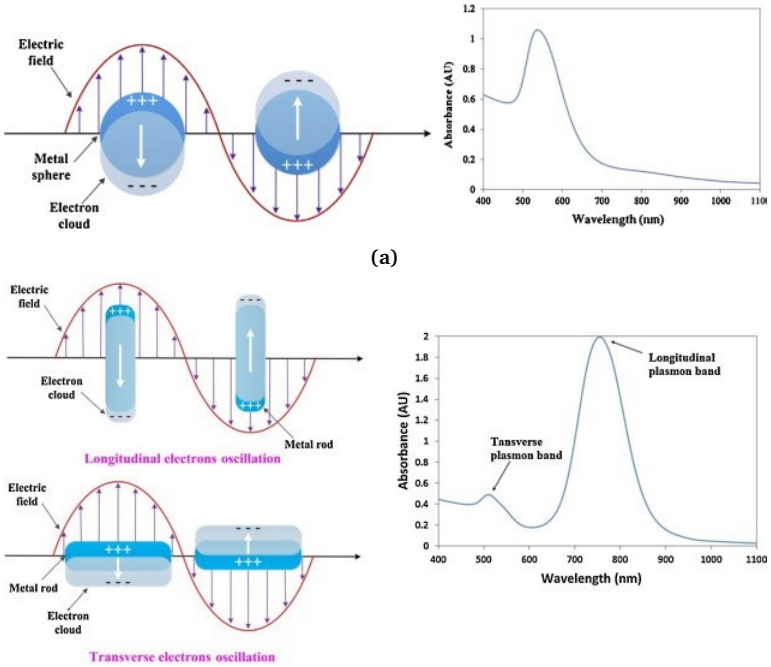

Figure 2.1.2: The optical properties of plasmonic nanoparticles (NPs) are shape and size-dependent. This figure illustrates the difference between NPs of isotropic and anisotropic shapes. Subfigure A) illustrates the LSPR-effect and resulting absorbance spectra for a spherical particle. Subfigure B) shows that a rod-shaped particle has two axes for the oscillations two occur and have, as a result, two corresponding LSPR-peaks. The Figure is adapted from [7].

2.1.2 Synthesis of Gold NPs

Back in 1857, Faraday began synthesizing gold colloids[12]. However, the real breakthrough for synthesis of Au NPs of anisotropic shapes was in 2001, when Jana et al. published the first article describing the seed-mediated growth synthesis route[8]. Numerous research groups have explored the seed-mediated growth synthesis protocol in the last two decades, tweaking the method for better shape control and higher yield. As illustrated in Figure 2.1.1, different additives and modifications to the growth solution have allowed a wide range of shapes. Other examples of shapes are nanorods with tunable rations[13, 14, 15], nanotriangles [16], and nanowires[17], to name a few.

A schematic of the method is shown in Figure 2.1.3. It is a two-step process, separating the process of nucleation and growth. First, a small monodisperse seeds of 1.5 nm diameter[8] is generated by gold precursor ($HAuCl4$) and strong reducing agent ($NaBH4$), in the presence of a stabilizing agent (CTAB). The second step introduces this seed into a growth solution consisting of gold precursor ($HAuCl4$), stabilizing and shape directing agent (CTAB), additives (Silver nitrate ($AgNO3$)), and mild reducing agent (Ascorbic acid (AsA)). The particles are then left to grow overnight and removed from the growth solution by centrifugation.

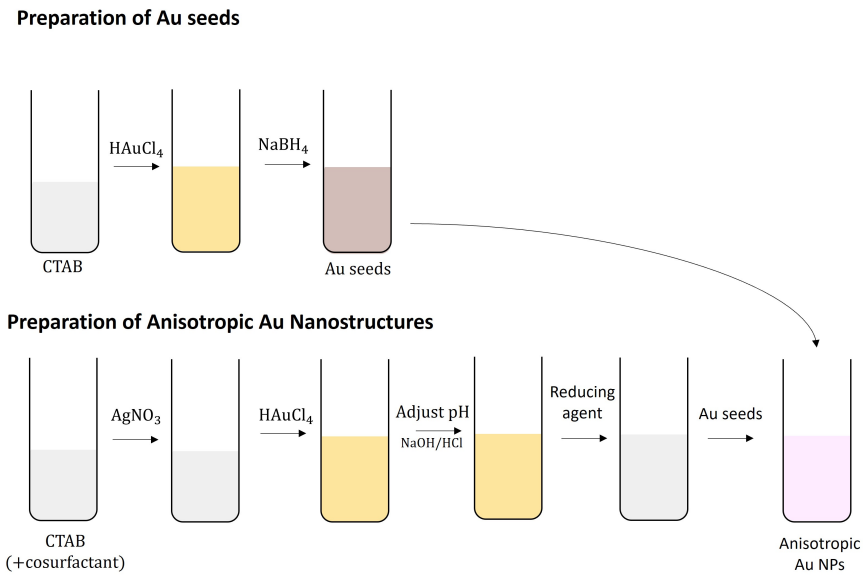

Figure 2.1.3: Schematic showing how synthesis of CTAB coated anisotropic Au NPs were done. Protocol from [18].

2.2 Charaterization of Nanomaterials

Characterization of synthesized Au NPs is vital to nanoparticle reasearch, synthesis quality control, and more. Figure 2.2.1 presents different physiochemical properties important for the final properties of an Au NP sample. This section will review the various characterization techniques used in this thesis; their working principle, advantages and limitations. Based on the reasearch objectives, section 1.2, the section will especially focus on the determination of Au concentration in solution, and measurement of hydrodynamic size of Au NRs. Experimental work on these subjects will be presented in Results and Discussion.

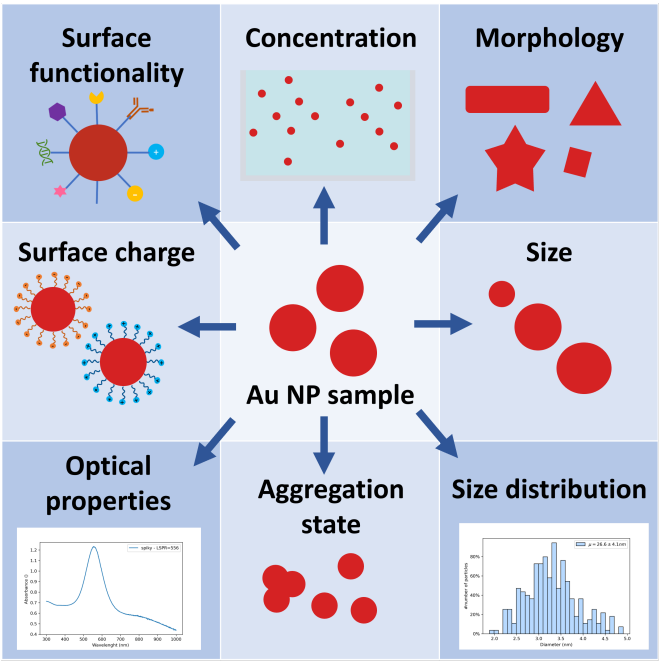

Figure 2.2.1: Charaterization is mapping of Au NP properties. This figure illustrate the most central properties of Au NPs. Figure made with strong inspriation from figure 14 in reference [19]. DNA and antibody illustrations are from flaticon.com.

2.2.1 Ultraviolet-Visible (UV-Vis) Spectroscopy

UV-Vis spectroscopy is used to study the optical properties of Au NPs. As illustrated in Figure 2.2.2, monochromatic light, with an intensity I_0, is sent through the sample,

and the intensity of the transmitted light, I, is measured. This measurement is typically repeated for wavelengths 1100 nm to 300 nm. Prior to the measurement, the absorbance of the solvent, typically water, is measured and used as a baseline. The resulting absorbance spectra are plotted with absorbance as a function of wavelength.

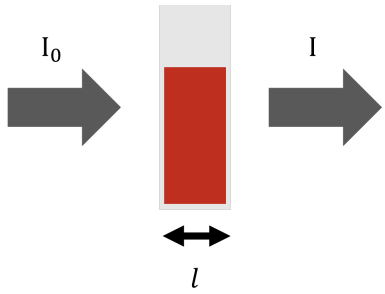

Figure 2.2.2: In UV-Vis spectroscop incident light, with an intensity, I0, is sent through a sample, and the resulting intensity of the transmitted light, I, is measured. Figure from previous work[20].

Theoretically, Beer-Lambert Law describes the absorption of monochromatic light[5]:

$$A = -\log_{10}(\frac{I}{I_0}) = \alpha c l$$

I_0 is the intensity of the incident light, I is the intensity of the transmitted light, α is the extinction coefficient, c is the concentration of the photo-active sample, and l is the optical path length of the sample. The equation only holds under conditions where absorbers act independently from each other, and to meet these criteria, samples measured with UV-Vis should be diluted to an absorbance of $I \leq 1.5$[21]. At concentrations higher than this, scattering between NPs occurs, and Beer-Lambert Law is invalid.

The optical properties are dependent on the shape, size, concentration, refractive index, and chemical environment of NPs. Especially the plasmon peak is sensitive to many parameters such as size, size distribution, surface modification, and aggregation[6], and the absorbance spectrum of a sample will give a researcher indications of all these factors. However, the factors can not be determined simultaneously, and accurate measurements of these properties are best examined through complementary characterization techniques. The spectra should primarily be used to examine relative changes in particle properties, either as quality control or as a comparison between similar synthesis procedures[22]. A clear advantage of UV-Vis is its high measurement repeatability and reproducibility[23]. The technique is straightforward, with little to no sample preparation steps, giving little room for user errors, making it especially good

for synthesis quality control.

Concentration with UV-Vis

The idea of selecting of wavelength where the main contribution to absorbance comes from interband transitions in metallic gold, which could be used to determine the amount of gold in solution regardless of the size and shapes of Au NPs, has been studied elaborately through many publications. However, in my thesis work, we found it challenging to understand and unravel how and whether this was possible to do or not. This literature review is written based on references [24], [25], [26], [27], [28] and [29], and aims, together with the experimental work, to conclude how and if concentration of Au NPs can be determined with UV-Vis spectroscopy.

Hendel et al.[24] represent the first breakthrough in the quantitative use of UV-Vis absorbance spectra to characterize Au NPs. Their article presents a theoretical framework based on Mie Theory to determine the size of spherical Au NPs from LSPR-position and particle concentration from absorption at 450, including an extensive number of tables and calibration plots directly giving the user size and concentration from UV-Vis spectra without performing calculations. Mie theory is a complete mathematical description of the physics of scattering of electromagnetic waves by homogeneous spherical particles[30].

Khlebtov[25] extended this work by comparing Hendels Mie theory simulations to T-matrix simulations and an extensive collection of experimental data. T-matrix simulations are another method for describing the scattering of electromagnetic waves by homogeneous spherical particles with computational techniques. The article focused on the effect of dielectric constants and polydispersity in size and concentration measurements from UV-Vis. The work concludes that particle shape and polydispersities significantly influence the absorbance at the plasmon peak. Furthermore, they showed that absorbance at 450 nm to determine concentration gave less impact on shape effects and lower uncertainties across various-shaped Au NPs.

The next significant addition comes ten years later with Shard et al[28]. The work expands on Haiss and Klebstov, using both Mie theory and T-matrix. Key points from this article are;

1. The plateau region between 405 and 450 nm is the least affected by the size, shape, or aggregation of Au NPs. Their figure with calculated extinction coefficients for randomly oriented spherical are shown in Figure 2.2.3.

2. Number concentration, and molar concentration can be calculated by the following equations:

$$C_N = \frac{4A}{\pi D_s^2 Q_{ext} l}(ln10) \tag{2.2.1}$$

$$C_M = \frac{2AD_s\rho}{3Q_{ext}l} \tag{2.2.2}$$

Where A is the absorbance, l is the measured path length, and D_S is the diameter of a sphere with the same volume as the particle. Q_{ext} is the extinction efficiency found via T-matrix simulations. These equations show that concentration depends on NP size and that molar concentration is preferred because it reduces shape dependency.

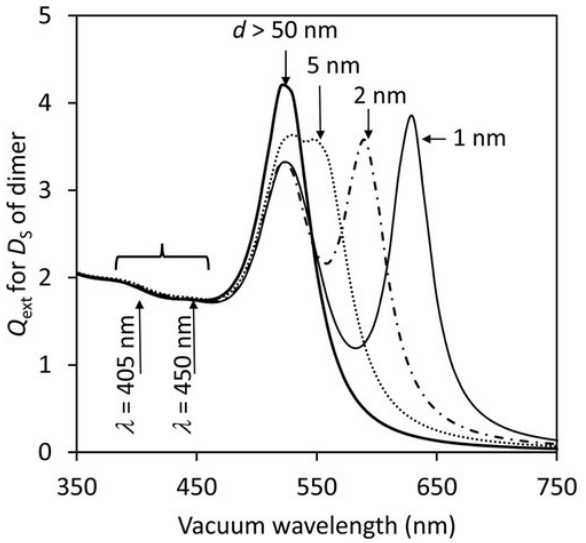

Figure 2.2.3: Shard[22] show that Plateau region 405 to 450 nm is not affected by size, shape or aggregation, and can be used to extract concentration.

In addition to these theoretical contributions, table 2.1 summarizes the most central experimental works of the last ten years. These conclusions will be tested and discussed in the Results and Discussion section.

Table 2.1: Summary table of experimental work

Reference	**Conclusion**
Hendel et al. [26]	* Au concentration can be determined reliably via Abs_{400} for systems with similar size and surface chemisty. * Using the assumption of full precursor reduction for comparison.
Scarabelli et al. [16]	* ICP-MS analysis showed that Au concentration can be determined reliably via Abs_{400} for both Au NRs and NSs. * An absorbance of 1.2 corresponds to Au concentration = 0.5 mM.
Shard [28]	* Theoretically calculates the formula of particle concentration and mass concentration * Shows that concentration is dependent on particle diameter also in the plateau region * Experimental work is compared to ICP-MS measurements
Roach et al. [29]	* Determine Au concentration by measuring absorbance of digested Au NPs * Confirms with Atomic spectrophotometer

2.2.2 Electron Microscopy

Electron microscopy (EM), is important for investigating the final morphological features, such as size and shape, of Au NPs. EM allows for resolution down to 0.2 nm in TEM mode depending on the microscopy settings and composition of the sample[31].

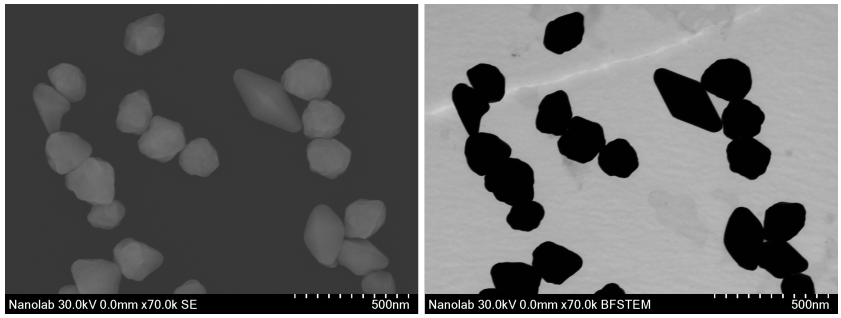

Figure 2.2.4: S(T)EM images taken with SEM mode left and BF-TEM mode right. SEM-mode give more information on morphological features of Au NP surface, while TEM mode give sharp edges suited for measuring particle size.

In EM, a focused, high-energy beam of electrons is directed toward a sample. The beam of electrons interacts with the sample through different processes, and the resulting signal is detected and presented as an image. Two main modes are used; Scanning Electron Microscopy (SEM), detecting scattered electrons with a detector above the sample, and Transmission Electron Microscopy (TEM), detecting the electrons transmitted through the sample. In this thesis, scanning (transmission) electron microscopy (STEM), a microscope including both SEM and TEM mode, is used. Figure 2.2.4 shows the difference between an image taken in SEM-mode and TEM-mode.

EM is a powerful technique, however, it is important to address that the technique has some challenges in extracting statistically meaningful data. First of all, the technique observes a few hundred or thousand particles, whereas, in reality, the sample normally has up to $\sim 10^{14}$ particles per ml. This means that the statistical representability is limited and that STEM measurements often can be biased[32]. Furthermore, it has been documented that shape segregation by drying is an occurring phenoenon[33]. This means that biproducts can accumulate in particular areas and are either over or underestimated based on the area of the grid counted. Lastly, there is a risk that the particle properties change as a result of drying[34], or as a result of three-dimensional (3D) NPs being projected onto two-dimensional (2D) images.

To improve STEM measurements higher number of particles from multiple locations

on the grid and using images with different magnifications. Other characterization techniques should also be used complementary to report the size distribution and polydispersity of the population. Other limitations are that the technique is expensive and time-consuming compared to other techniques.

2.2.3 Dynamic Light Scattering (DLS) and Electrophoretic Light Scattering (ELS)

DLS and ELS are typically conducted in the same instrument setup and are used to give information on particle size and surface charge, respectively

Dynamic light scattering (DLS)

DLS is based on measuring the Brownian motion of particles in suspension. Figure 2.2.5 shows the schematic of a conventional DLS setup; A sample with particles moving under Brownian motion is illuminated with a laser beam, and the intensity of the scattered laser light is detected by a detector. As the Figure shows, larger NPs diffuse slower and scatter more light, while smaller particles move faster and scatter less light. The detected light intensity is analyzed with respect to their fluctuations and translated into the autocorrelation function g_2.

Figure 2.2.6 presents a typical correlation function and also what information can be extracted from the function. The auto-correlation functions is translated into the average translational diffusion coefficients via the Siegert relation[36]:

$$g_2(\tau) = 1 + \beta \left|\exp(-Dq^2\tau)\right|^2$$

$g_2(\tau)$ is the intensity correlation function, τ is the lag time, q is the scattering vector, β is the coherence factor describing the solid angle of the detector, and D is the translational diffusion coefficient.

The diffusion coefficient is further related to the hydrodynamic diameter (H_d) by assuming the shape of a perfect sphere and using the Stokes-Einstein equation[5]:

$$D = \frac{k_B T}{3\pi\eta D_h} \tag{2.2.3}$$

k_B is the Boltzmann constant, T is the temperature, and η is the dynamic viscosity of the solvent.

The hydrodynamic diameter, H_d, is, as a result, the diameter of the perfect sphere that diffuses with the same diffusion coefficient, as the measured NP. The concept is

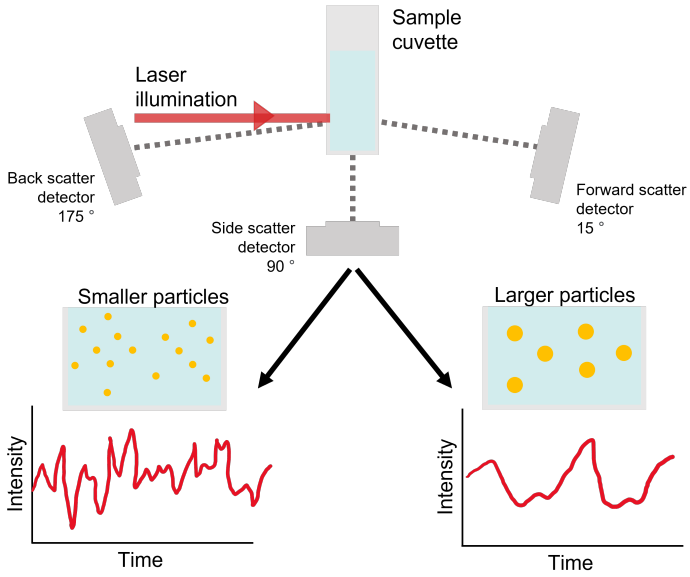

Figure 2.2.5: In dynamic light scattering, laser light is sent towards a sample of nanoparticles moving with Brownian Motion. The resulting intensity, after interaction with the sample, is measured with a detector either at 15°, 90°, or 175° angle, and used to find the size of the nanoparticles. Smaller particles move faster and scatter less light, while large particles move slower and scatter more ligth. The Figure is made with inspiration from [35]

illustrated in Figure 2.2.7.

In polar solvents, such as water, particles with a surface charge cause the formation of an electric double layer[38]. The size of this layer depends on the temperature, ionic strength (pH), viscosity of solvent, and particle-particle interactions. As a result, deviation from the geometric diameter, as measured with electron microscopy, can become significant. However, it is worth noting that some argue that the hydrodynamic diameter is a more relevant measure in further applications or functionalization. A study of 21 Au NP types with different surface chemistires and shapes, concluded that physiocemical properties of Au NPs in biological applications are mainly accounted for by their hydrodynamic diameter and their zeta-potential[39]. The Figure also illustrates the resulting hydrodynamic diameter of an aggregated sample and an anisotropic sample.

Determination of particle size and particle size distribution with DLS is based on the assumption that only the Brownian motion of the particles influences the scattering of laser light signals. The technique also assumes the particle shape of a perfect sphere.

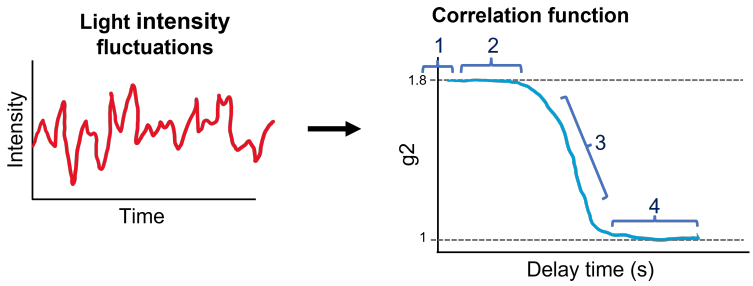

Region 1	• Offset from g2(t=0) = 1.8 is caused by noise • Concentration is too high or too low
Region 2	• How well particles correlate to them self over time • Small particles move faster and correlate faster • Large particles move slower and correlate over longer time
Region 3	• Slope gives polydispersity of particle population • Monodisperse sample = sharp slope • Polydisperse sample = weak incline
Region 4	• Elevated baseline or noise in the base line is an indication on dust, aggregated NPs, or non spherical NPs

Figure 2.2.6: Intensity fluctuations is detected by a detector and translated into the correlation function, g_2. How the fluctuation signal correlates give the information on size and size-distribution, as indicated by the Figure and table. This Figure is based on "Particle Charaterization by Dynamic Light Scattering (DLS) - A guide to Anton-Paar LiteSizer500" a presetation given by Hammad Farooq, Core Engineer at Particle Engineering Core Facility, and reference [37].

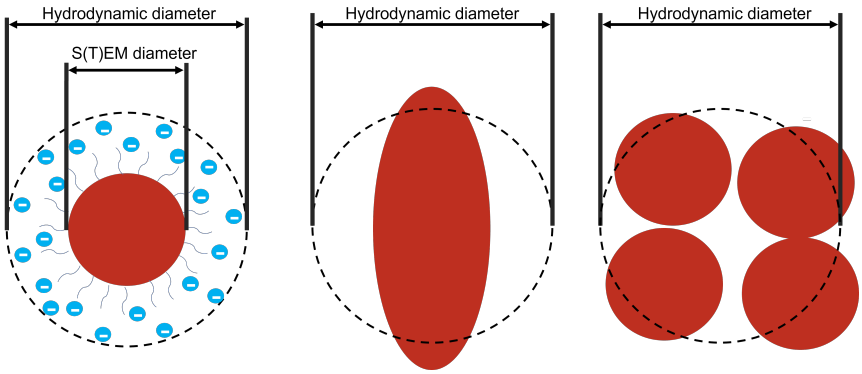

Figure 2.2.7: The diameter measured by DLS correspond to the diameter of a sphere that diffuses in the same way as the sample. If the NP-population is eiter aggregated or anisotropic, then the hydrodynamic diameter don't give comparable results. Illustation after [40] .

However, other factors can influence the signal;

Particle concentration can be a large contribution to change in laser intensity signal. If the particle concentration is too high, concentration effects will dominate the intensity signals, and Brownian motion is no longer primarily reflected[38]. In these cases, size and size distributions can appear random. The high concentration can cause multiple scattering within the sample, and non-random spatial movement in the sample due to collisions and concentration gradients in the system. Sample preparations are therefore essential to minimize the impacts of these factors. The g_2 correlation function at region 1, as illustrated in Figure 2.2.6, can be used to optimize the sample concentration, aiming at a value of g_2 at time $= 0$ sec as close as possible to 1.8 for Au NPs[37]. Homogeneous sample concentration can be ensured by establishing a dispersion routine, for example, by using a vortex and sonicator for a set amount of time.

Particle morphology is also vital to understanding a DLS measurement. DLS relies on the assumption of a perfect sphere that only moves with its Brownian motion. However, as any anisotropy is included in its shape, the particle will also move with a rotational Brownian motion caused by one or multiple rotational axes in the particle shape. The formation of particle clusters, through agglomeration, aggregation, or sedimentation, will also change how the particles move. Also, here, the g_2 correlation function is a good tool for quality control. As shown in Figure 2.2.6, region 4, the tail of the correlation function, contains detail on how well the particle dispersion is. Furthermore, the fit between the correlation function experimental data, and the calculated model, can be used to discuss the validity of the measurement.

The polydispersity of the sample also greatly influences the measurement. The level of polydispersity is indicated in the slope of the correlation function, as illustrated in Figure 2.2.6. The DLS initially uses intensity weighted size distributions, and since large particles scatter more light, the larger particles of a population will be overestimated. However, with more advanced software, many DLS setups allow conversions from intensity weighted size distribution into volume and number weighted distributions. This conversion is found to be simple from a mathematical point of view. However, some literature argues that the conversion amplifies the noise and artifacts in the resulting size distribution[38]. Therefore, comparing the different weighting methods can be a good solution to get meaningful DLS data from a polydisperse sample.

The previous paragraphs discussed the effect of particle concentration, particle morphology, and polydispersity on DLS measurements. Choosing a detection angle where these factors influence the signal as little as possible, making the Brownian motion the primary factor of scattering, is, therefore, a key point to getting good quality

measurements. Table 2.2, adapted from reference [38], discusses the advantages and disadvantages of choosing forward, standard, and backscattering angles. However, some newer setups even come with continuous detection angles and software to choose the optimum detection angle for each sample.

Table 2.2: Summary table of pros, cons and usage of the three most common measurement angles in DLS set-ups. The table is adapted from [38].

	Forward	**Sideward**	**Backscattering**
Pro	* Most accurate * Hardly any impact by Brownian motion	* Interlaberatory comparison * High signal quality * Less artifacts	* Supressed impact of multiple scattering * Reduced sensitivity to rare coarse particles * Variable measurement volume
Con	* Very sensitive to any noise (dust, agglomerates, contaminants) *Increased measurement time * Large impact of multiple scattering	* Large impact of multiple scattering * Significant impact of Brownian rotation for anisotropic particles	* Significant impact of Brownian rotation for anisotropic particles * Wall scattering gives extra noise and artifacts
Use	Monodisperse NPs	Dilute polydisperse samples with low turbidiy	Polydisperse samples with turbidity

Hydrodynamic diameter of anisotropic Au NPs

The research team lacked an optimized protocol for DLS measurement of anisotropic Au NPs, such as rods. Litterature on this was also very hard to find. Therefore, the results and discussion section contains a study comparing DLS measurements of two different sized Au NRs acquired at different scattering angles and dilutions. The acquired data will be presented and compared to the literature as explained in this section with an aim to find optimum measurement conditions.

Electrophoretic Light Scattering (ELS)

ELS can be used to measure the zeta potential (ZP) of a NP sample. The ZP give information on the surface charge and can be used to evaluate the stability of the

synthesized NPs and change in surface chemistry[5]. The principle is similar to DLS, but in ELS, the cell containing the sample has electrodes. As an electric field is applied through the sample holder, particles with a net charge migrate towards the oppositely charged electrode. This particle motion causes a Doppler shift effect in the laser signal. The particle electrophoretic mobility is determined from the detected laser signal frequency distribution and related to the ZP[41].

The physical meaning of the ZP is illustrated in Figure 2.2.8. As illustrated in the Figure, zeta potential depends on the chemical equilibrium between the NPs and their solvent and is not a property of NPs alone. Any variation in the solvent, such as salts or increased dilution, would affect this equilibrium and consequently the measured zeta potential.

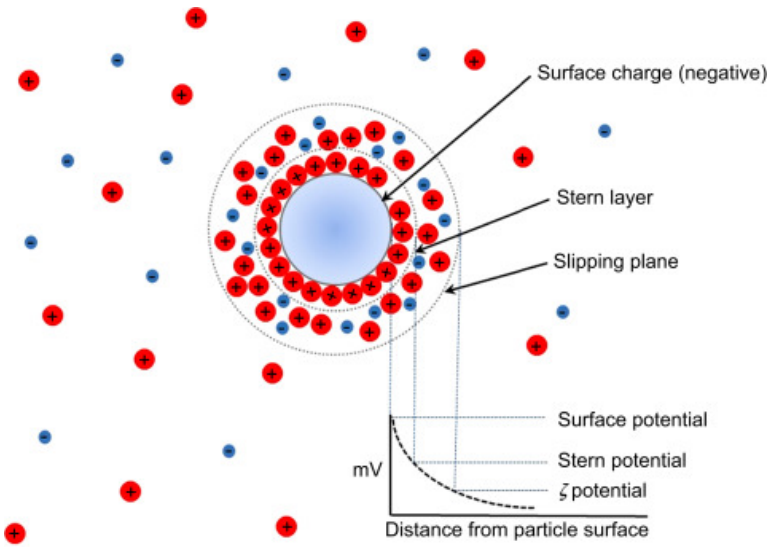

Figure 2.2.8: Zetapotential (ZP), is the electrical potential in the slippingplane, meaning the charge that develops between the NP and the solvent. This figure illustrates this physical meaning of Zetapotential (ZP). The figure is from [42].

Ultimately, as systematic dilutions and identical solvents are used, ELS represents rapid, accurate, and highly reproducible results[43].

2.2.4 Particle Tracking Analysis (PTA)

Particle Tracking Analysis (PTA), also known as Nanoparticle Tracking Analysis, can be used to find hydrodynamic diameter, size distribution, and particle number concentra-

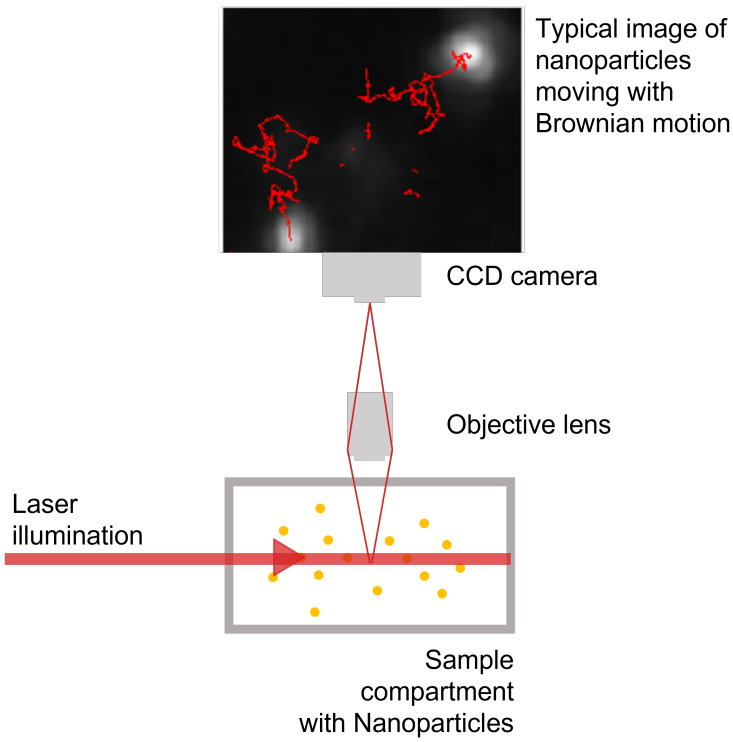

Figure 2.2.9: A simplified Nanoparticle tracking analysis set up is shown in this figure. The technique is based on tracking the borwnian movement of NPs between image frames taken with the CCD camera. The figure is made with inspiration from [44] and [45]. The typical image of tracking of nanoparticles moving with Brownian motion is Figure 2 in [44].

tion of an NP sample. Figure 2.2.9 shows the schematic of a PTA device. The device uses a laser to illuminate the NP sample solution. This allows a conventional optical microscope fitted with a CCD camera, with an analytical software package, to track the Brownian motion of each particle. The average distance each particle moves between image frames is automatically calculated, and by measuring the sample temperature and knowing the solvent viscosity, the Stokes-Einstein equation(equation 2.2.3) can be used to find the diffusion coefficient and the hydrodynamic diameter of the NPs. PTA is also used to find the particle concentration; the sample volume is known, and the measurement counts the number of particles in the volume.

A major challenge of PTA is that the system settings depend on the sample's light-scattering properties. As the size and refractive index of the NP sample change, the

measurement settings need to be optimized[23]. If these settings are set wrongly, the presence of certain particles can be ignored or overestimated. Furthermore, the dilution of the sample has to be adjusted to meet an optimum count rate per frame of the system. As a result, the measurement technique needs a skilled operator, and results will be dependent on individual judgment and experience. Futhermore, it is a particle counting method, just as S(T)EM, and comes as a result, with the same challenges in achieving statistically viable results[46]. To ensure representability, a sufficient number of particles must be analyzed.

There are different opinions of measurement reproducibility and accuracy in literature[46]. An article by Vasco et al.[45] shows that the technique can offer a better resulting estimate of particle size and particle size distribution than the conventional DLS technique. In the article, measurements with PTA and DLS are compared to EM measurements. PTA measurements track each individual particle and will therefore not suffer from the overestimation of bigger particles by intensity measurements like DLS measurements. However, when PTA practice between different laboratories and also different users within the same laboratories are compared particle counting methods are found to have the lowest reproducibility, with measured between-labs variability of 46% for PTA [23]. The article also showed that the method had a positive bias, with 71 % of laboratories significantly overestimating the number concentration of the particles: up to over four times the nominal value.

Other advantages of PTA are that it requires a small sample volume for analysis, it is cheap and relatively easy and quick(compared to MP-AES and S(T)EM).

2.2.5 Microwave Plasma Atomic Emission Spectrometer (MP-AES)

Microwave Plasma Atomic Emission Spectrometer (MP-AES) can be used to determine the concentration of specific ions in solution. MP-AES is an atomic emission technique, meaning that the technique detects characteristic emissions spectra as an atom returns from an excited state into the ground state.

Figure 2.2.10 shows a schematic of a typical setup for an MP-AES. The sample is introduced into the system and changed into an aerosol using a nebulizer and a spray chamber. The aerosol is then sent to the hot plasma, where it dries, decomposes, and is atomized. As the atoms return to lower energy states, they emit light at wavelengths characteristic to the element. An optical system picks up the emitted light and registers the intensity at a specified wavelength range. Before sample measurement, the emission of a set of standards made from the same element is measured, and linear regression is

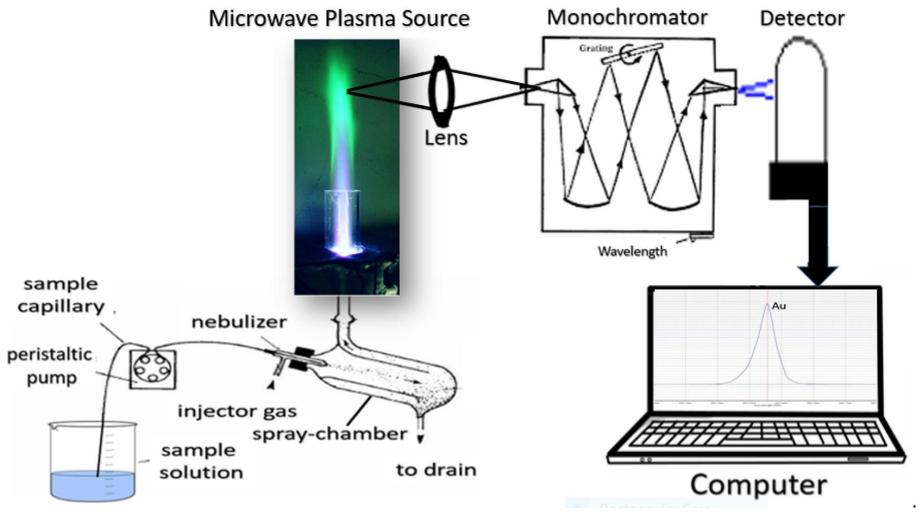

Figure 2.2.10: Schematic of MP-AES set up, from [47].

used to make a calibration curve. The final concentration of the sample is quantified by comparing the measured intensity to the standard curve[48]. Prior to the measurement of mass concentration of NPs, the NPs must be digested into metal ions in solution. This typically takes one to two days.

The main advantage of MP-AES, pointed to in the literature is the high sensitivity of MP-AES. Many studies, [47, 49, 50] conclude that detection limits of MP-AES are comparable to that of Inductively coupled plasma mass spectrometry (ICP-MS) measurement. At the same time, the technique is more economical due to its reliance on nitrogen gas for plasma instead of argon.

However, a challenge found in our research group is the technique's sensitivity to dirt and other contaminants. This results in more frequent downtime than any other instrument at our core facility, and also different intensity profiles in measurements from week to week. Therefore, the result and discussion section includes a section exploring the reproducibility of MP-AES measurements.

2.3 Surface Functionalization

Advances in surface functionalization facilitate the exploration of new and more advanced biomedical applications for Au NPs[51]. Surface functionalization changes the surface chemistry, such as solubility, stability, and surface charge, and can ultimately allow for specific recognition of a target species [6].

Au NPs synthesized through the seed-mediated growth synthesis method, as described in section 2.1.2, has a positively charged CTAB layer on the surface. The CTAB surfactant is essential in the synthesis, both as a structure-directing agent allowing NPs to grow into different shapes and also to stabilize and protect the NPs against aggregation. However, the stability of CTAB capped NPs is unsatisfactory for many applications. The CTAB-capped Au NPs are only stable in CTAB aqueous solution with lower pH, and several different conditions, such as high salt content, low CTAB concentration, or organic additives, can cause serious aggregatiopn[7]. Furthermore, it has also been shown that excess CTAB can be cytotoxic for in vitro applications[52].

Figure 2.3.1 illustrates the two main approaches taken to functionalize CTAB coated Au NPs; surface encapsulation and ligand exchange. This section outlines methods for functionalizing CTAB coated Au NPs, followed by a detailed description of the method modified and studied in this thesis.

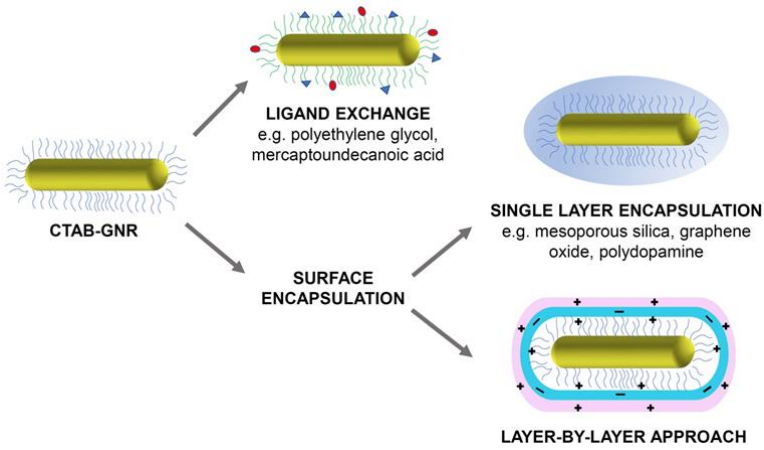

Figure 2.3.1: Illustration of the most common strategies for surface functionalization theories of CTAB coated Au NPs. Figure from [53].

2.3.1 Surface Covering

As illustrated in figure 2.3.1, surface covering aims to encapsulate the CTAB-layer by introducing one or more additional coatings. There are three common ways of achieving this; *Electrostatic interaction* between the positive charged CTAB-layer and an anionic polyelectrolyte is an easy and common way of achieving this. Poly (sodium 4-styrene sulfonate) (PSS) and poly(acrylic acid) (PAA) are two common anionic polyelectrolytes used for surface covering[7]. Further functionalization can be done through hydrophobic interaction for PSS-coating and carboxy group for PAA-coating. *Layer-by-layer* is another method commonly used. The technique offers excellent versatility in adjusting to specific applications of interest, such as incorporating drugs into the layers[53]. The thickness of layers is reported anywhere from 7 nm to 40 nm. The third type of surface covering method is *coating with hard inorganic materials*. Silica and silver are often used[7].

Surface coverage methods offer straightforward synthesis methods with versatile further modification. The disadvantage of surface covering is that the remaining CTAB on the surface is concerning. It is believed that the coverage is sufficient to make the NPs biocompatible, however, detailed studies have not yet confirmed this[53]. It is also not documented how these thick layers affect the optical properties of Au NPs for biosensing applications.

2.3.2 Ligand Exchange

Ligand exchange aims to replace the CTAB-layer with other organic ligands or biomolecules. Thiols have a very strong affinity toward gold. Therefore, to replace CTAB, thiolated ligands are popularly used, binding to the Au NP-surface via the strong Au-S bond. Multiple reviews[6, 7, 53] rank ligand exchange with thiolated ligands as the most popular method. Two main methods are presented in literature reviews;

Thiol-terminated polyethyleneglycol (PEG) are available commercially with a large range of functional groups on the other end at a low cost[53]. PEG is a water-soluble compound, making these methods straightforward, typically adding the PEG into the Au NP solution and letting it incubate for a given period of time. The solution is then cleaned for excess PEG by centrifugation. A challenge of this method is that the PEG is quite large in size. The size makes it difficult for the PEG to diffuse through the dense CTAB layer, resulting in incomplete removal of CTAB[7]. This is especially challenging for Au NRs where CTAB is densely packed on the 111 facet. Furthermore, the large size of the PEG-SH also increases the distance from the analyte to Au NP-surface, reducing

the sensitivity if used as an LSPR-based biosensor[7].

11-mercaptoundecanoic acid (MUA) is another popular ligand for the surface functionalization of Au NPs. The molecule is a much smaller thiol-terminated ligand, allowing for higher LSPR sensitivity and complete removal of CTAB[54]. The molecule has a carboxylic group, making further functionalization via EDC/NHS coupling easy[7]. Coating with MUA gives biocompatibility without changing the shape and size of the NP[53]. However, a considerable challenge of MUA functionalization is that MUA is not water-soluble. The CTAB-coated Au NPs are highly unstable in organic solvents, and as a result, functionalization with MUA has trouble with irreversible aggregation. Reviews, such as [7], point out that several approaches to solve this problem have been published, but that the review authors and other researchers still observe significant aggregation of the Au NPs following their procedure. The review furthermore lists three "working" approaches for MUA functionalization. The first solution[55], uses an ionic exchange resin to prevent aggregation in the Au NPs. They argue that this is elegant and effective but appears to be time-consuming and complex to operate. Next, the review presents their own work[56], using alkaline pH and no organic solvents, to enable MUA functionalization in a fully aqueous environment.

PEG and MUA Functionalization

The third option the review lists is combining PEG and MUA functionalization into a two-step procedure. The method was first published by Thierry et al.[37, 57], and the final modified protocol is illustrated in figure 3.3. PEG is used in the first step to replace the majority of CTAB surfactants, introducing stability in the Au NPs in the presence of an organic solvent. In the second step, MUA is introduced to remove the remaining CTAB and replace some of the PEG. The method has given a robust straightforward method of overcoming the challenges in functionalization with the two molecules by themselves.

The surface functionalization with PEG and MUA will be studied in this thesis. As described in section 1.2, the aim with the thesis is to study the shape dependency in surface functionalization of Au NPs for biosensing applications. This method with PEG and MUA was chosen for this study for several reasons. First of all, the method is documented as a straightforward and robust method for surface functionalization, also documented and developed within the research group[18]. Next, the protocol has two steps where shape dependency can be looked at. The grafting density of PEG-functionalization has already been documented to be affected by surface chemistry

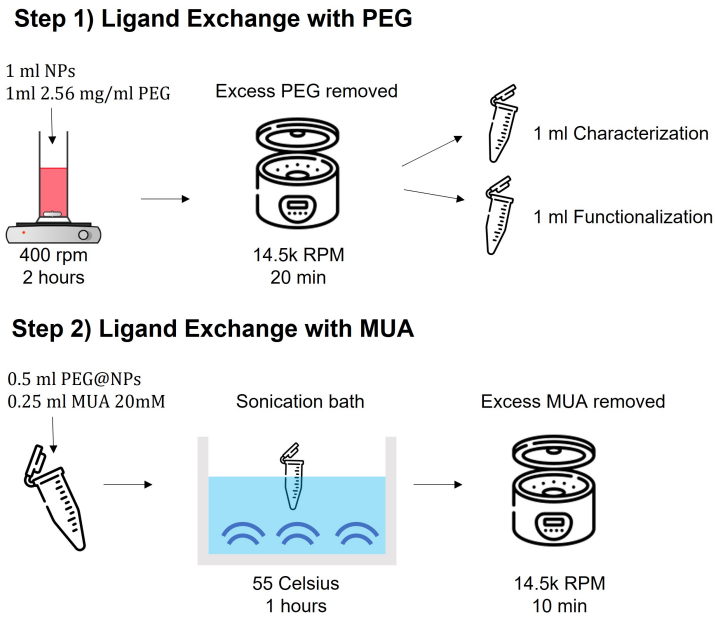

Figure 2.3.2: Schematic of the adapted protocol for MUA and PEG functionalization of Au NPs. Eppendorf and centrifuge icons are from Flaticon.com.

and shape [58]. Lastly, the carboxy groups from MUA make it suitable for testing with model protein biosensing systems.

2.4 Biosensing Applications

The color change in home pregnancy tests is an example of the use of Au NPs in biosensing applications. More generally, biosensors show importance in clinical diagnosis, food and water safety, environmental monitoring, and more[7]. This section will shortly describe what a biosensor is, how we can describe the performance of a biosensor, and applications based on refractive index-based biosensors.

2.4.1 What is a Biosensor?

A biosensor is defined as a device that converts a biological response into a measurable signal[3]. Figure 2.4.1 shows a schematic of a typical biosensor as presented by Bhalla et al.[4]. Starting from the left;

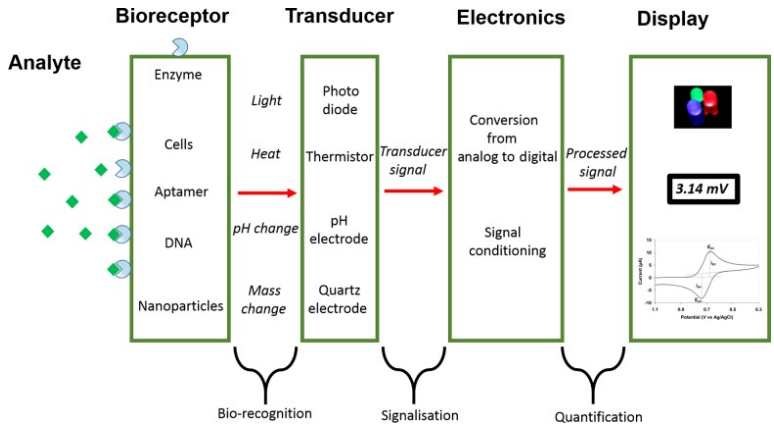

Figure 2.4.1: Schematic of the elements making up a biosensor. Figure from [4].

The *Analyte*, is the substance of interest for detection. *Bioreceptor* is the biological moiety that specifically recognizes the analyte. The bioreceptor is typically antibodies or enzymes, and in many NP-based biosensors the biorecptor is bound to the NPs. Next, the *Transducer* is the element that covert the biological recognition into a measurable signal. Most transducers produce an electrical or optical signal proportional to the amount of analyte bound to the bioreceptor. The signal from the trancuser is then picked up and processed by *Electronics*, and lastly, presented to the user on a *Display*. The output could, for example, be a number or a graph.

2.4.2 Performance of a Biosensor

Several factors determine the performance of a biosensor. Some key concepts are; *Selectivity*, the ability of a biosensor to detect the analyte of interest from other substances and contaminants in a sample[4]. *Sensitivity*, the minimum amount of analyte that a biosensor can detect, defining the limit of detection for a biosensor. And, *Reproducibility*, the ability of a biosensor to give the same results after measurement under the same condition[59].

Furthermore, scaling up from laboratory development and proof-of-concept, to a commercial biosensor is challenging. In addition to a good balance between high Selectivity, Sensitivity and Reproducibility, a biosensor should be fast and easy to use at a low cost. The lab concept should be possible to scale up into a practical, robust tool that could be used under many conditions, and preferrably by unskilled or semiskilled operators. The biosensors should also be biocompatible, nontoxic, nonantigenic, portable, and stable[60].

2.4.3 Refractive Index Based Biosensors

Nanotechnology has been utilized to enhance the performance of biosensors. NPs offer a large surface-area-to-volume ratio, allowing to immobilize increased amounts of the analyte, amplifying the analytical signal, and improving sensitivity. Particularly the LSPR-properties of Au NPs can provide a very sensitive probe to detect changes in the surrounding dielectric environment[3]. Figure 2.4.2 illustrates the working principle of LSPR-based sensors. As an analyte bind to the NP surface, a shift in the LSPR-position is induced and detected by the biosensor.

The shift in LSPR-peak position can theoretically be expressed as follows[7];

$$\Delta\lambda = m\Delta n[1 - exp(\frac{-2d}{l_d})] \tag{2.4.1}$$

Where, m is the bulk refractive index, Δn is the change in refractive index, d is the thickness of the adsorbed layer on the NP, and l_d is the characteristic electro-magnetic field decay length.

Depending on the origin of LSPR changes, it is distinguished between two types of refractive index-based sensors; aggregation sensors and refractive index sensors[3]; In *aggregation-based biosensors*, introducing the analyte induces colloidal aggregation in the NPs, resulting in a broadening of the LSPR-peak and absorbance spectra. The LSPR shift is extremely sensitive and can be used to make label-free colorimetric assays

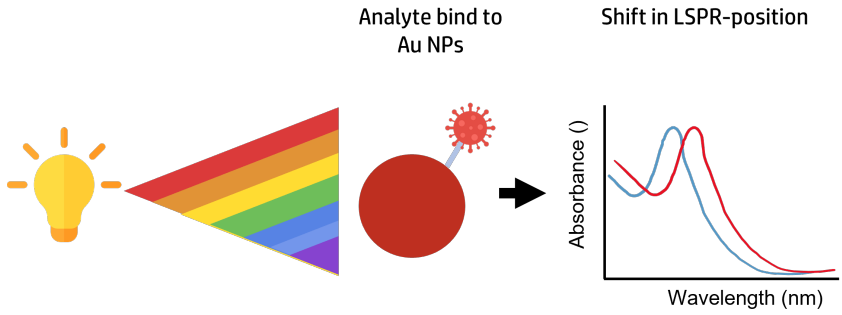

Figure 2.4.2: Working principle of a refractive index based biosensor. When analytes bind to the Au NPs, the local chemical environment of the NPs changes, inducing a shift in the LSPR-peak position.

that can be visualized with the "naked" eye[3]. Reference [61] use thiol-modified antisense oligonucleotide capped Au NPs, to create an aggregation-based biosensor for SARS-CoV-2. Viral RNA induces aggregation, following a color change in the assay, with a selectivity limit of detection of 0.18 $ng/\mu l$.

Biosensors based on refractive index LSPR shifts, are generally less sensitive than aggregation-based biosensors[3]. However, these biosensors allow for compatibility with recent advances in nano-optics such as multiplexing or microfluidics and in-flow assays. Furthermore, a broader versatility in functionalization chemistries is available.

The sensitivity of the refractive index is largely influenced by NP size and shape[3, 62]. A popular metric for describing the sensitivity of the refractive index for a certain nanomaterial is *nm/RIU*. The unit describes the shift in LSPR peak position per unit change in the refractive index of the surrounding medium[63]. Refractive index sensitivity generally increases as Au nanoparticles elongate and their apexes get sharper. An example of this is illustrated in figure 2.4.3. Ellipsoidal-shaped Au NPs of aspect ratio five show 5-10 times larger refractive index sensitivity than spherical Au NPs[3].

2.4.4 Biosensing with Biotin and Streptavidin

Model proteins are often used in the proof of concept for biosensing platforms. That means using simple molecule such as a dye or a protein to show that a biosensing design is working. One of the most well-known test systems are the biotin-streptavidin model couple. The first demonstration of monitoring of biomolecular interactions with UV-Vis spectroscopy was done with biotin linked to Au NPs self-assembled onto a monolayer

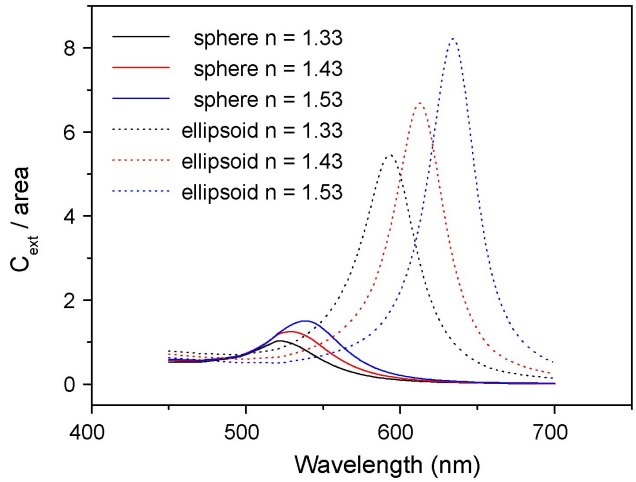

Figure 2.4.3: As Au NPs elongate, the refractive index sensitivity increase. This figure show that Ellisoidal shaped Au NPs of aspect ratio 5, show 5-10 times larger shifts in LSPR-peak position as the refractive index sensitivity, compared to spherical Au NPs. Figure from reference [3].

on glass. The spectrophotometric sensor showed concentration-dependent binding and a detection limit of 16 nM for streptavidin[64].

Figure 2.4.4 shows the possible interactions of Streptavidin with Biotinylated Au NPs as illustrated by reference[65]. As Streptavidin is introduced to the system, it can induce NP aggregation or result in a monolayer coverage on the surface. The Au NPs in this thesis will be tested with a biotin-steptavidin system as presented by Aslan et. al[65].

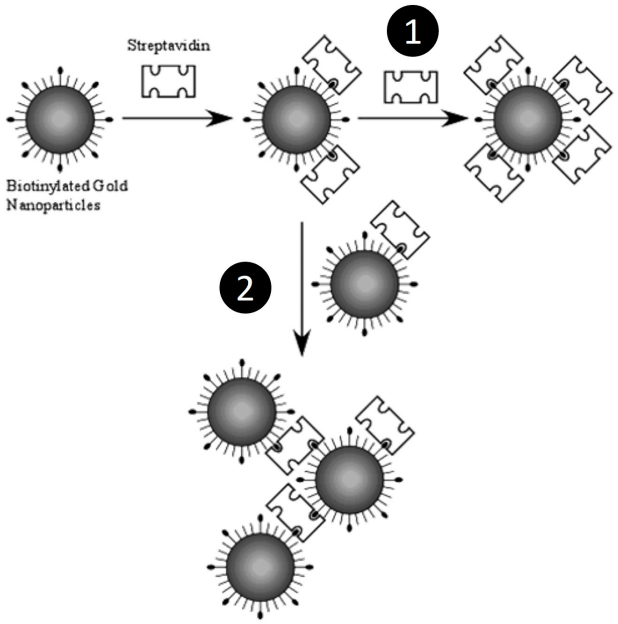

Figure 2.4.4: When streptavidin is introduced into a sample of Biotinylated Au NPs, two modes of interactions appear. 1) Formation of streptavidin monolayer on the Au NPs, or 2) Aggregation of Au NPs. Figure modified from reference [65]

3 Materials and Methods

3.1 Chemicals

All chemicals used in this thesis are listed in Table 3.1, and were used without further modifications. Distilled de-ionized water (MQ water) was produced by Simplicity Millipore water purification system, and used in all experiments.

Table 3.1: Chemicals used during this thesis with abbrevation, purity and supplier.

Name	Abbreviation	Purity	Supplier
Biotinyl-3,6,9,-trioxaundecanediamine	BA	-	Pierce
D-(-)-Isoascorbic acid	AsA	$\geq$ 98%	Alfa Aesar
Ethanol, 2-(2-aminoethoxy) ethanol	AEE	98%	Sigma-Aldrich
Ethanol		96%	VWR chemicals
Hexadecyltrimethylammonium bromide	CTAB	$\geq$99%	Acros Organics
Hydrochloric acid	HCl	37%	VWR chemicals
Gold(III) chloride trihydrate	$HAuCl_4$	$\geq$ 99.9%	Sigma-Aldrich
Nitric acid	HNO_3	-	-
N-hydroxysuccinimide	NHS	98%	Sigma-Aldrich
N-3-(Dimethylaminopropyl)-N'-ethylcarbodiimide	EDC	Technical grade	Sigma-Aldrich
Oleic acid	OA	$\geq$ 99%	Sigma-Aldrich
O-[2-(3-Mercaptopropionylamino)ethyl]-O'-methylpolyethylene glycol	PEG-SH	5000 Da	Sigma-Aldrich
Polyethylene glycol sorbitan monolaurate	TWEEN 20	$\geq$ 40.0%	Sigma-Aldrich
Potassium phosphate monobasic buffer	PB	$\geq$ 99.5%	Fluka
Silver nitrate	$AgNO_3$	$\geq$ 99.0%	Sigma-Aldrich
Sodium borohydrate	$NaBH_4$	$\geq$ 98.0%	Sigma-Aldrich
Sodium citrate dihydrate	NaCit	$\geq$ 99%	Sigma-Aldrich
Sodium hydroxide	NaOH	$\geq$ 99%	Sigma-Aldrich
Tannic acid	TA	-	Sigma-Aldrich
Streptavidin	-	unconjugated	Merck
11-mercaptoundecanoic acid	MUA	98%	Sigma-Aldrich

3.2 Synthesis of Gold Nanostructures

3.2.1 Synthesis of Citrate Coated Au NPs - Turkevich Method

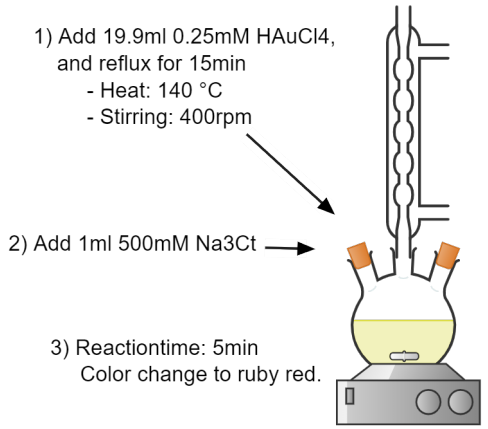

Figure 3.2.1: Schematic showing Turkevich Method used to make Citrate coated Au NPs. Method from [66], figure from my own previous work[20].

Citrate-coated Au NPs were synthesized with Turkevich method. The protocol was adapted from Wuitschick et al.[66]. Set-up, and work flow is shown in Figure 3.2.1.

A three-necked round bottom flask with a conical magnetic stirring bar was set up in a heating mantle and connected to a condenser. Then, 19.9 ml of 0.25 mM $HAuCl_4$ was added. The solution was then refluxed at 140 $^{\circ}C$ for 15 minutes with stirring at 400 rounds per minute (rpm). Boiling in the solution should be observed in this step. Next, 1 ml of 500 mM NaCit was added quickly, and the solution was left to react for 5 minutes, giving the solution a color change to ruby red. The RBF was then lifted from the heating jacket and left to cool down.

3.2.2 Synthesis of CTAB Coated Au NPs - Seed-Mediated Growth Method

Silver Assisted seed-mediated growth synthesis route, from Bandyopadhyay et al.[18], was used to make CTAB coated Au NPs. Seed type, cosurfactant, pH and weak reducing agent were varied to obtain the different shapes. All synthesis conditions are listed in Table 3.2. A schematic of the protocol is shown in Figure 2.1.3.

It is a two-step process, and the first step is to make the seeds. In a 50 ml glass vial with a magnetic stirrer, 364.5 mg of CTAB was dissolved in 5 ml of MQ-water by heating at 75 $^{\circ}C$ and stirring at 400 rpm. Once dissolved, the vial was transferred to a 25 $^{\circ}C$ heat plate. Next, 5 ml of 0.5 mM $HAuCl4$ was added, and stirred at 750 rpm for 7 minutes. Then, 1.6 ml freshly prepared 3.75 mM $NaBH_4$ was added. The solution was left to react for 2 minutes before the magnetic stirrer was removed. The seed solution was used after 30 minutes.

Table 3.2: Synthesis conditions for the CTAB coated Au Nanostructures made for this master thesis. Synthesis conditions for CTAB@Au NP are from previous work by Jibin Antony (Ph.D. candidate), CTAB@Au NR OA are from [18], CTAB@Au NR TA are from previous work by Katharina Zürbes (co-supervisor and Ph.D. candidate), and spiky nanostructures are from my own previous work[20].

Sample	**Surfactants**	**AgNO3**	**pH**	**Reducing agent**	**Seed**
CTAB@Au NSs	1.2g CTAB	-	10.7	AsA 96 μl	-
CTAB@Au NRs OA	1.2g CTAB + 24 mg OA	750 μl	-	AsA 96 μl	CTAB
CTAB@Au NRs TA	1.2g CTAB	750 μl	-	TA 750μl 0.1 M	CTAB
CTAB@Au NPs Spiky	1.2g CTAB + 20 μl OA	750 μl	10	AsA 96 μl	Citrate

In a typical growth solution, 1.2 g of CTAB, sometimes with a cosurfactant, was dissolved in 15 ml of MQ-water by heating at 75 $^{\circ}C$. As the solution turned clear, the temperature of the heating plate was reduced to 35 $^{\circ}C$. Next, once cooled to 35 $^{\circ}C$, 750 μl 4 mM $AgNO_3$ was added and stirred for 15 minutes. Then, 15 ml 1 mM $HAuCl_4$ was added, giving the growth solution a yellow color, and stirred for another 15 minutes. The stirring was next increased to 1000 rpm, and the pH was adjusted according to the desired synthesis conditions. 135 μl of weak reducing agent AsA was then added, resulting in an immediate color-change to clear. Lastly, after 30 seconds, 96 μl of the seed solution was added, left to react for 30 seconds, and the stirring bar was removed. The solution was then left overnight at 35 $^{\circ}C$. The day after, the NPs were removed from the growth solution and excess CTAB by two rounds of 30 minutes centrifugation at 14.5k rpm. Lastly, the NPs were redispersed to 5 ml with MQ-water.

3.3 Functionalization of Gold Nanostructures

A two-step ligand exchange with MUA and PEG was used to increase the stability and add carboxy groups to the surface of the Au NPs. The method was introduced in section 2.3.2 and is adapted from Thierry et al.[57] and Bandyopadhyay et al.[18].

A schematic of the method is shown in Figure 2.3.2. In the first step, a small glass vial with a magnetic stirrer bar was set up on a stirring plate. 1 ml of Au NPs and 1 ml of PEG solution 2.56 mg/ml were stirred at 400 rpm at room temperature for 2 hours. The magnetic stirrer was then removed, and the sample solution was transferred into two small Eppendorf tubes, each holding 1 ml of sample solution. Excess PEG was removed by centrifugation with Minispin at 14,5k rpm for 20 min and redispersed in 1 ml MQ water. One of the two samples was used for characterization and one for further functionalization.

In the second step, a 20 mM MUA solution was prepared by dissolving in 50 % ethanol and 50 % MQ water. 500 μl of the PEGylated Au NPs and 250 μl of 20 mM MUA were then added to a 2 ml Eppendorf tube and vortexed for 5 seconds. The sample solution was left to react for 1 hour in a sonication bath at 55 Celcius. A floating Eppendorf tube holder was used in this step. Every 15 minutes, the sample solution was checked for sedimentation and shortly vortexed. Lastly, the particles were cleaned from ethanol and excess MUA by centrifugation with Minispin at 14,5k rpm for 20 min and redispersed in 1 ml MQ water.

3.4 Model Biosensing System with Biotin and Streptavidin

The protocol for biotinylation of Au NPs was modified from publications by Aslan et al.[65] and Hinman et al.[67]. A schematic of the method is presented in Figure 3.4.1.

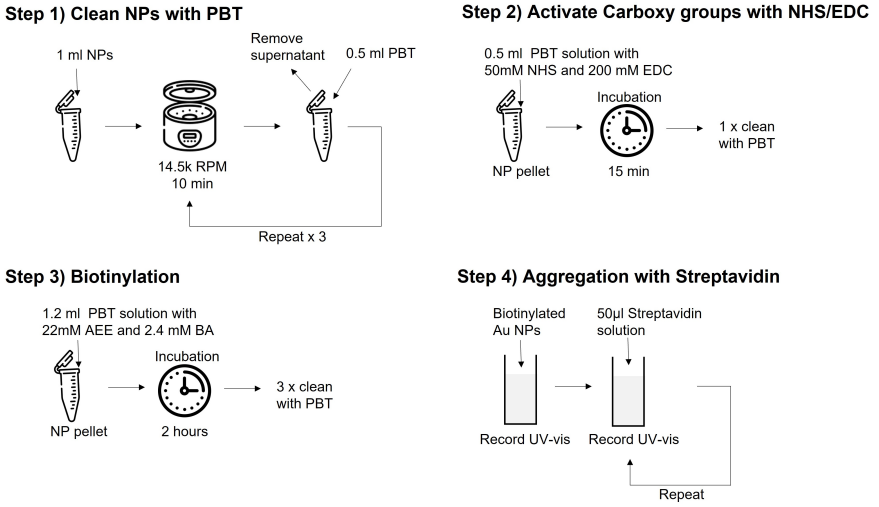

Figure 3.4.1: Schematic of model biosensing system with Biotin and Streptavidin. Protocol is adapted from [65], and [67]. Eppendorf and centrifuge icons are from Flaticon.com.

First, buffer solutions were prepared. Potassium phosphate monobasic buffer (PB), was prepared to 10 mM, and the pH was adjusted to 7 by dropwise adding 0.25 M NaOH. Phosphate buffered Tween (PBT) was prepared by weighing in Tween 20 and diluting with the PB solution to 1.82 mg/ml.

Before starting biotynelation, 1 ml of the PEG and MUA functionalized NPs were first cleaned three times by centrifugation and resuspension with 0.5 ml PBT. This was found to be enough NPs to meet the absorbance of 0.3 used by reference [65]. After the final centrifugation step, the NPs were redispersed with 0.5 ml of freshly prepared 50 mM N-hydroxysuccinimide (NHS) and 200 mM N-3-(Dimethylaminopropyl)-N'-ethylcarbodiimide (EDC) in PBT, and left to react for 15 minutes. The resulting solution was centrifuged and redispersed with 0.5 ml of PBT and then again centrifuged. This NP pellet was resuspended in 1.2 ml freshly prepared 22 mM Ethanol, 2-(2-aminoethoxy) ethanol (AEE) and 2.4 mM Biotinyl-3,6,9,-trioxaundecanediamine (BA) solution in

PBT for 2 hours. The final biotinylated Au NPs were cleaned three times through centrifugation and resuspension with PBT.

All centrifugation in this protocol was done in 1.5 ml Eppendorf tubes with Minispin at settings 14,5k rpm and 10 minutes. Resuspension was done by sonicating and flushing the particles simultaneously. For UV-Vis characterization NPs were redispersed with 1 ml PBT. For DLS and ELS, NPs were diluted with 2 ml PBT.

3.5 Characterization

3.5.1 Ultraviolet-visible (UV-vis) spectroscopy

Agilent Cary 60 UV-vis spectrophotometer was used to aquire absorbance spectra. The samples were measured from 300 to 1000 nm.

3.5.2 Scanning (Transmission) Electron Microscopy (S(T)EM)

Electron microscopy (EM) images were obtained using Hitachi High-Tech SU9000 Scanning (Transmission) Electron Microscope at Nanolab NTNU. Acceleration voltage of 30 kV and current of 15 or 20 μA was used. Samples were prepared by dropping 40-100 μl of NP-solution on a carbon-coated copper grid from Electron Microscopy Sciences. ImageJ was used for image processing, measuring minor and major axis of 200 - 300 particles per sample, from at least 3 different images at different magnifications. The resulting size are presented as average with standard deviation as uncertainty.

3.5.3 Litesizer

Anton Paar Litesizer 500 was used with Dynamic light scattering (DLS), to find hydrodynamic diameter (H_d) with electrophoretic light scattering (ELS) to find Zetapotential (ZP).

3.5.4 Zetaview

Table 3.3: Measurement saettings used for Zetaview Particle tracking analyzer.

Setting	
Minimum brightness	25
Max area	100
Min area	5
Trace lenght	15
Nm / class	30
Classes / decades	69
Sensitivity	60
Framerate	30
Shutter	100

Particle Metrix ZetaView, Particle tracking analyzer, was used to measure particle concentration and hydrodynamic diameter. Samples were diluted to meet optimum measurment conditions of 100 - 200 particles per frame. Other settings were kept constant as presented in Table 3.3.

3.5.5 MP-AES

Agilent 4210 MP-AES Optical Emission Spectrometer, with an Agilent SPS 4 Autosampler, was used to measure particle concentration (mg/l). Nine standards of concentration, 0, 0.38, 0.75, 1.13, 1.50, 2.25, 3.00, 4.50 and 6.00 mg/l was used to make the calibration curve.

Digestion of Au NPs to Au ions, were done after[68]. In a small vial, 0.5 ml of Au NP into 4.5 ml Aquaregia (3:1 volume HCl:HNO3). The mixture was left to digest for 2 days, and diluted with 15 ml MQ water. For future use by new master students and other in the Particle Engineering Reasearch group, Appendix B present a detailed description of the method, including important HSE-measures that should be taken.

4 Results and Discussion

With an overall goal to study the shape dependency in functionalization of Au NPs, the research objectives, as presented in Section 1.2, were formed. These research objectives structures this Results and Discussion chapter; The first part presents the synthesis and characterization of Au NPs of five different shapes. This is followed by a second and third part studying the Characterization of Au NPs, more precisely determination of Au concentration and hydrodynamic diameter of anisotropic Au NPs, respectively. The fifth part establishes surface functionalization with PEG and MUA of Au NPs and discusses the shape dependency in this functionalization. Lastly, in the 6th and final part, the Au NPs are applied in a model biosensing system with Biotin and Streptavidin.

4.1 Synthesis of Au Nanostructures

Four CTAB-coated Au NPs and one citrate-coated Au NPs were synthesized for this master thesis. An "engineering approach" and synthesis conditions based on previous works were applied to synthesize these nanostructures. Important criteria for these Au NPs were distinct LSPR-peak and colloidal stability. The CTAB-coated Au NPs were made following the procedure and synthesis conditions in Section 3.2.2, and the citrate-coated Au NPs were made following the procedure in Section 3.2.1.

Representative STEM images of all NPs are shown in 4.1.1. The STEM sizes and morphologies were found using image analysis as described in section 3.5.2. Table 4.1 shows the results, and appendix A presents the images with corresponding size distributions. The images reveal two spherical structures, referred to as Citrate@Au Nanospheres (NSs) and CTAB@Au NSs, two rod-shaped structures, CTAB@Au NRs OA and CTAB@Au NRs TA, and one spiky structure, CTAB@Au NPs Spiky.

The optical properties of the Au NPs were studied with UV-Vis spectroscopy, and absorbance spectra are presented in Figure 4.1.2. Section 2.1.1 discussed how the optical

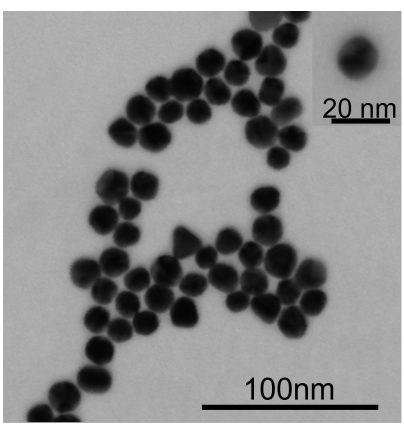

(a)

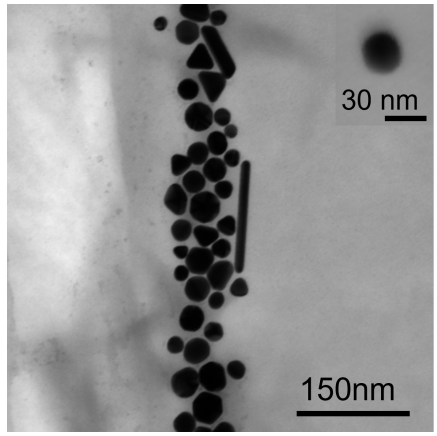

(b)

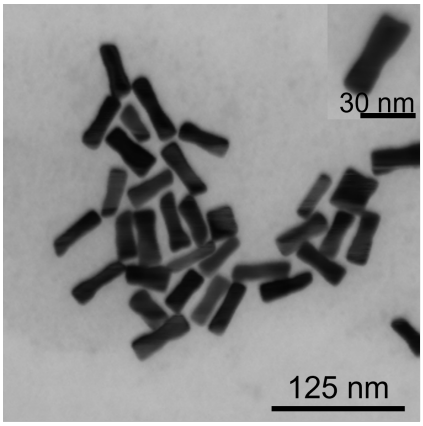

(c)

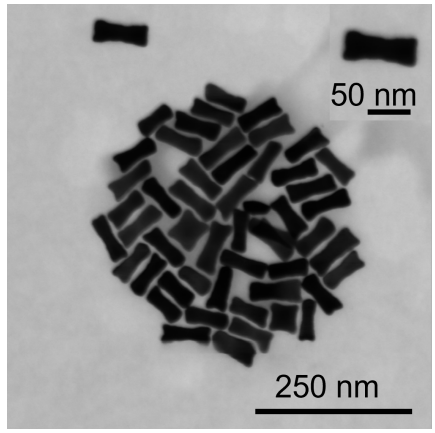

(d)

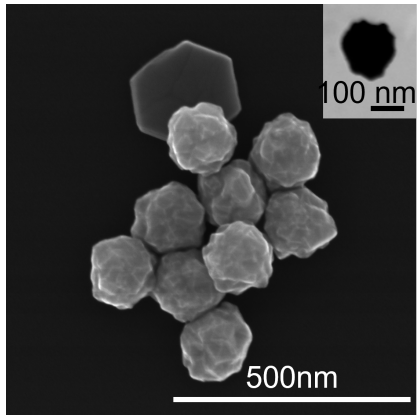

(e)

Figure 4.1.1: Representative scanning transmission electrion microscopy (STEM) images of the different shaped Au NPs. Subfigure A) is Citrate@Au NSs, B) is CTAB@Au NSs, C) is CTAB@AU NRs OA, D) CTAB@Au NRs TA, and E) CTAB@Au NPs Spiky.

properties of Au NPs are dependent on the shape, size, and dielectric environment of the NP-sample, and Figure 2.1.2 showed the difference between the absorbance spectra of Au NPs of isotropic and anisotropic shapes. Figure 4.1.2 show that both Citrate@Au NSs and CTAB@Au NSs exhibit the single LSPR-peak, typical of isotropic Au NPs. Compared to Citrate@Au NSs, CTAB@Au NSs have a broader peak at a more redshifted position. As confirmed with STEM imaging, this points to larger sizes and greater polydispersity. The two rod-shaped structures have two distinct LSPR-peaks corresponding to longitudinal and transverse oscillations in the electron clouds, as described in Figure 2.1.2. The final structure, CTAB@Au NPs Spiky, features an LSPR peak that is formed like a plateau and spans 550–750 nm. The sample has a bimodal distribution of triangular plates, as seen in Figure 4.1.1 and Appendix A. The spiky NPs' STEM size also exhibits a considerably high standard deviation of 24 nm. Both factors contribute to the LSPR-broadening and redshift in position.

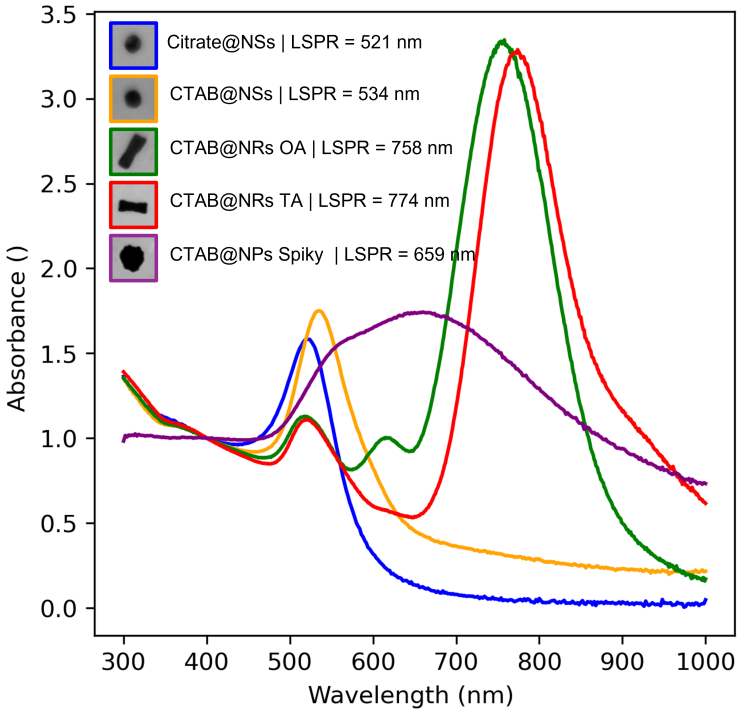

Figure 4.1.2: Absorbance spectra and LSPR position of the Au NPs. Each spectra are nomralized to them self at 400 nm.

The zeta-potentials and hydrodynamic diameters are shown in table 4.1. When compared to STEM sizes, Au NRs exhibit reduced DLS sizes, and Au NSs exhibit larger DLS sizes. The experimental work on DLS measurements of anisotropic Au NRs, which will be described later in this thesis, is consistent with these findings. The DLS method is based on assuming the form of a perfect sphere.

Table 4.1: Summary table showing the characteristics of five different Au NPs. Average diameter (d) and aspect ratio (AR) are found with Scanning (transmission) electron microscopy. Hydrodynamic diameter (H_d) and Zetapotential (ZP) is found using Litesizer.

Sample	**D (nm)**	**AR**	**H_d (nm)**	**ZP (mV)**
Citrate@Au NSs	17	-	125	- 24.8
CTAB@Au NSs	28	-	65	34.8
CTAB@AU NRs OA	43	3	13	24.7
CTAB@Au NRs TA	71	3	37	15.4
CTAB@Au NPs Spiky	153	-	159	29.2

Citrate@Au NSs was made based on the Turkevich synthesis procedure, with molar ratio $[NaCit]/[HAuCl4] = 10$. The protocol is well established and has proven to be robust and reproducible through many publications[66]. In reference [66], Table 1, a STEM size of 9.3 ± 0.4 nm is reported for a similar molar ratio. Another article, reference [69], studies the size effect of different molar ratios in Turkevich synthesis. The reference reports LSPR-peak as 520 nm and the same STEM size of 9 nm as the previous article. Both these reported sizes are significantly smaller than the 17 nm found in this thesis. As seen in Table 1 reference [66], this could mean that the molar ratio was larger than planned, either from a higher NaCit concentration or a lower $HAuCl_4$ concentration. The reaction times used in this thesis were significantly shorter than in these articles. Furthermore, user bias in STEM size can also influence the results. All these three factors could justify the differences in STEM size. However, most importantly for the work of this thesis, with a distinct LSPR peak and the high zeta potential indicating stability, Citrate@Au NSs align with the criteria for further functionalization.

The seed mediated-growth synthesis route is designed to gain control over anisotropic growth by separating the nucleation and the growth process. To make CTAB coated spheres, synthesis conditions had to be altered to allow isotropic growth. However, the interplay of the parameters has made it hard to unravel the direct effect of each parameter[70]. After input from Jibin Antony (Ph.D. candidate), the CTAB@Au NSs

were made using seed-mediated growth protocol with growth solution without $AgNO_3$ at high pH and without seeds. The high pH gives a high reduction potential and fast growth. It is discussed that $AgNO_3$ promotes for anisotropic growth[70]. The chemical was therefore left out. The resulting Au NPs, as seen in STEM images Figure 4.1.1 and Appendix A.2, consist of primarily spheres as well as some rods. The polydispersity is prominent, both in LSPR spectra Figure 4.1.2, but also through STEM imaging. Bruns uses similar synthesis conditions of pH 11 without $AgNO_3$, but with seeds[68]. The publication (Figure 13a) shows that these NPs are more monodisperse. Using seeds could be a better approach. Nevertheless, it was concluded that it would be interesting to see the effect of polydispersity in functionalization.

CTAB@Au NRs OA was made via a seed-mediated growth approach employing a binary surfactant mixture with CTAB and OA. The synthesis conditions were chosen after Bandyopadhyay et al[18]. The synthesis yielded similar structures compared to the reported STEM size, absorbance spectra, and zeta-potential in their publication. The cosurfactant OA has a double role as a reducing agent and promotes the dog-bone-like morphologies in the tips.

CTAB@Au NRs TA was made using an alternative reducing agent of TA. The synthesis yielded a longer Au NR of the same aspect ratio as CTAB@Au NRs OA. Polydispersity is comparable in the two samples. The structure was chosen to see if using an alternative reducing agent influences further surface functionalizing.

CTAB@Au NPs Spiky was made after my previous work[71]. Spiky structures are shown to be great candidates for biosensing with Surface-Enhanced Raman Scattering[72]. Here Turkevich seeds were employed in a growth solution of binary surfactant mixture with CTAB and OA at pH 10, and Au NPs with spiky surfaces were obtained.

Ultimately, this thesis's results align with previous work; Seed-mediated growth and Turkevich are robust methods to produce stable Au NPs. However, small changes in synthesis conditions can give differences in final morphology. - A major challenge of Au NPs in applications.

4.2 Concentration of Gold Nanoparticles

Au NPs exist as clumps of atomic gold Au(0) in solution, and there are two main ways of describing a sample's gold concentration; *Molar concentration* is the total concentration of gold element per liter in solution, and *particle number concentration* is the number of particles in solution. Furthermore, *Surface area concentration*, not commonly used, measured in nm^2/ml, could especially be relevant for surface functionalization and biosensing applications. Determining particle concentration or gold concentration in solution is vital for research, applications, and industrial exploitation. Examples are determining the yield of Au NPs when studying their growth mechanisms, studying Au NP uptake into the cell, or to ensure reproducibility in synthesis. In this thesis concentration determination is mainly used to support the optimalization of surface functionalisation protocols.

4.2.1 Measurement Repeatability with MP-AES

Section 2.2.5 discussed how MP-AES reproducibility in measurement has been of concern in our research group. Therefore, a small study on measurement reproducibility was carried out. There were primarily two factors of concern. 1) Would there be variations caused by polydispersity and inhomogeneous dispersions within NP samples, and 2) would there be any effect of dirt, contamination, and usage when measurements were done with a 1-month time difference, including several downtimes and repairs? Detection limits were also of interest.

Digestion and measurement with MP-AES were done following the protocol as described in section 3.5.5, and the resulting concentrations are presented in Table 4.2 and Figure 4.2.1. Repetitions 2 and 3 were done in the same session, employing the same calibration standard curve. Repetition 1 was done in a previous session.

The resulting concentrations show overall good correlation. Standard deviations for all measurements are less than $0.01 mg/ml$. Differences are systematically larger between samples measured during different sessions.

Balaram[47] report detection limit of Au element to $1.8 ng/ml$. In contrast, the findings of this study suggest that concentration measurements of Au NPs are valid down to $0.01 mg/ml$. This could seem like a significant disagreement with Balaram[47]. However, it is important to bear in mind that detection limit is found using commercial gold standard measuring Au ions, and not Au NPs. The standard deviation between samples is arguably more likely to come from differences within the Au NP populations

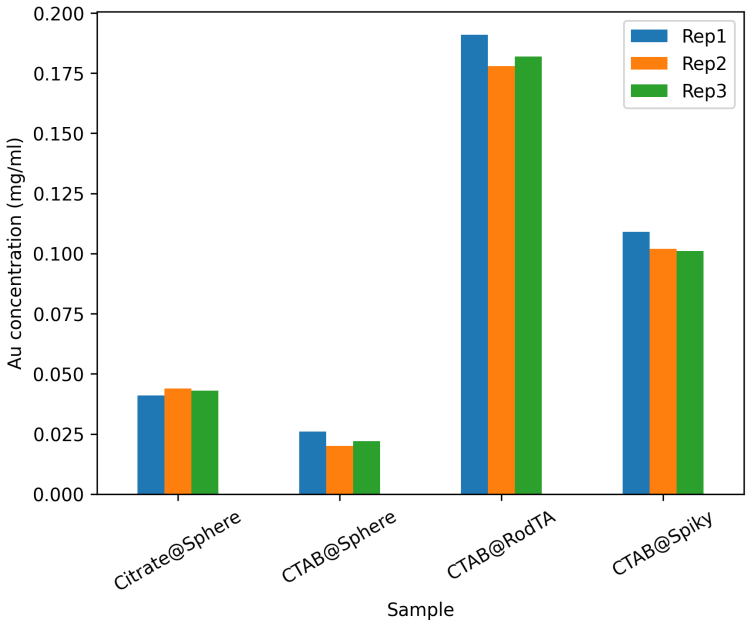

Figure 4.2.1: Bar plot showing the measured Au concentration (mg/ml). Rep2 and Rep3 were measured in the same session, using the same standard curve calibration. Rep1 was done in a previous session. Table 4.2 show number values.

than the apparatus's sensitivity limit. This argument is further strengthened by the fact that the most monodisperse Au NPs, Citrate@Au NPs, also has the smallest standard deviation of 1 $\mu g/ml$.

4.2.2 Particle Number Concentration and Surface Area Concentration

Surface area concentration could be particularly useful for surface functionalization but also for other applications. Furthermore, a publication by Xia et al. shows that the coverage density of PEG depends on the initial surface chemistry and shape of the Au NPs[58]. This section compares four different methods of obtaining surface area concentration. The comparison is made by measuring the five different shaped Au NPs as preseted in section 4.1. The motivation of this work was to support the optimization of the surface functionalization protocol.

The surface area concentration is particle number concentration multiplied by

Table 4.2: Concentration of Au in mg/ml, measured with MP AES. Rep2 and Rep3 were measured in the same session, using the same standard curve calibration. Rep1 was done in a previous session. Repeats are missing for CTAB@Au NRs OA because of a sample spill accident, thereby missing sample volume.

Sample	Rep1	Rep2	Rep3	Std
Citrate@Au NSs	0.041	0.044	0.043	±0.001
CTAB@Au NSs	0.026	0.020	0.022	±0.002
CTAB@Au NRs OA	0.160	-	-	-
CTAB@Au NRs TA	0.191	0.178	0.182	±0.006
CTAB@Au NPs Spiky	0.109	0.102	0.101	±0.004

surface area. Three methods were used to find the particle number concentration. First, PTA was used to obtain the metric directly. Measurement procedures were described in section 3.5.4. Next, the Au concentration of the NPs was also measured by MP-AES, as described in section 3.5.5. This concentration was then combined with size measurements from DLS or STEM to find the volume, and the density of face-center-cubic (FCC) gold of $19.3 kg/dm^3$, to find particle concentrations. A detailed description of these calculations can be found in Appendix C. Figure 4.2.2 compares the particle concentrations obtained through these three different methods.

For surface area concentrations, the particle number concentrations presented over are multiplied by the surface area per NP as measured with DLS and STEM. The geometrical approximations and calculations are presented in Appendix C. Figure 4.2.3 presents the resulting surface area concentrations.

Comparing particle volumes from STEM and DLS, see Figure C.1.1 appendix C, there is a clear distinction between the spherical NPs and the rod-shaped NPs. Compared to STEM, the spherical NPs are overestimated with DLS, while the rod shapes particles are underestimated. The volume of the spiky structure is similar for STEM and DLS. This same trend is propagated to particle concentrations with MP-AES. CTAB@Au NRs OA demonstrates this trend with a measured particle concentration of magnitude 10^12 when estimated with MP-AES+DLS, compared to 10^9 when estimated with Zetaview, see Figure 4.2.2.

Section 2.2.4 addressed that overestimating particle concentration is a normal and recurring phenomenon using PTA. The section also discussed a study on measurement reproducibility of the number concentration of Au NPs. The study reported that 71 % of laboratories in showed a positive bias[23]. In contrast, the PTA method exhibits

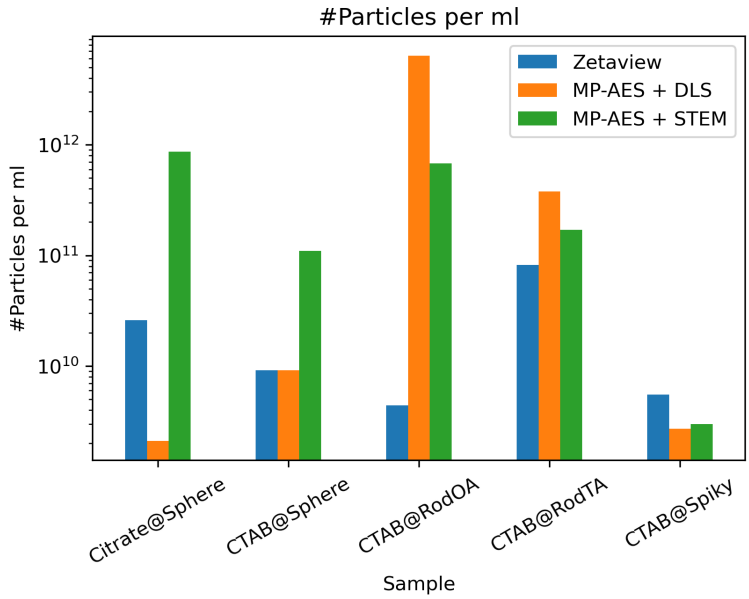

Figure 4.2.2: Particle number concentration found through three different methods.

the lowest particle number concentration in three of the five shapes, Figure 4.2.2. For Au NPs spiky, PTA is in the same order of magnitude and slightly higher than the two MP-AES methods. For Citrate@Au NSs, it has a value that falls between the two MP-AES techniques. Taking the literature into account, this could indicate that all concentrations of this study are positively biased. A commercial bead with a known concentration would have complemented the study well.

Ultimately, particle number and surface area concentration both show significant differences when acquired with different methods. CTAB@Au NPs spiky, the largest spherical Au NP sample, showed the closest correlations in methods. In contrast, small spherical NPs and anisotropic NRs both showed differences in the size range of multiple magnitudes.

4.2.3 Au Concentration with UV-vis

The different published methods to measure UV-vis were summarized in Table 2.1. A set of 14 different NPs was measured with UV-vis and compared to MP-AES measurements to evaluate these methods. Appendix D presents an overview of the NPs used in this section. Briefly, the five different shapes synthesized for this thesis, six spherical citrate

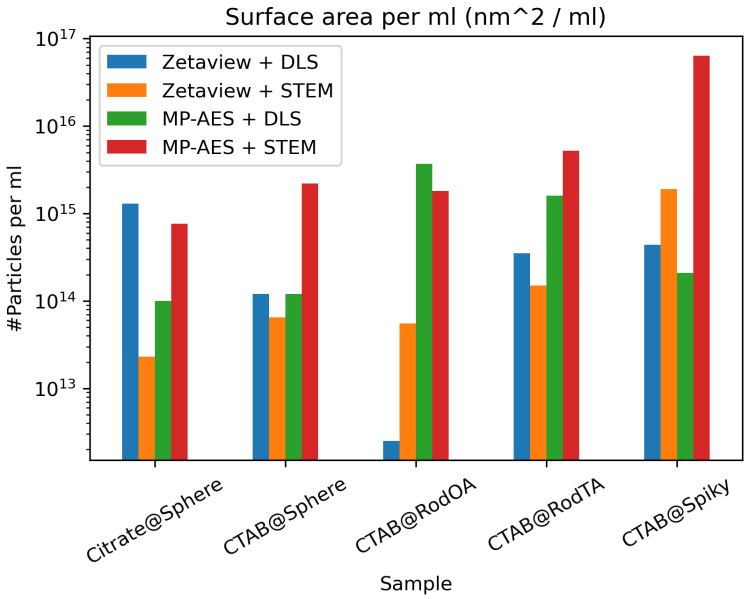

Figure 4.2.3: Surface area concentration found through four different methods.

coated Au NPs with stepwise increasing sizes made in previous work[20], and three CTAB coated Au NRs from seed-mediated growth with TA from Tina Bruns Master Thesis[68] were used. All NPs were digested according to the protocol in Section 3.5.5, and digested UV-vis were therefore measured in 40 dilution factor.

The boldest claim presented in the summary table is from Scarabelli et al.[27]. The paper states that; "*The reduction yield can be precisely estimated from the absorbance at 400 nm (Abs_{400}), regardless of the shape and size of the nanoparticles.*". Figure 4.2.4 shows the Abs_{400} for all NPs of our experimental set plotted versus MP-AES concentration. The scatter plot clearly shows disorder, without any linear trends. Scarabelli et al.s absorbance of 1.2 corresponding to Au = 0.5 mM is also in contradiction to these findings. The linear regression line presented here gives an absorbance of 0.2 for Au = 0.5 mM.

Looking at the actual experimental data presented in the paper, Figure 2C, Scarabelli et al. have studied a very limited set of only five Au NRs. The Abs_{400} for these five Au NRs is plotted against the Au concentration determined by ICP-MS measurement in the figure. Scarabelli et. al. then suggests that Abs_{400} can be used to determine Au concentration independent of form and size using the linear trend shown in this

Figure. Figure 4.2.5 demostrates that our experimental dataset likewise reveals more linear pattern when only the Au NRs are plotted versus Au concentration obtained from MP-AES analysis. In other words, the linear relationship is disrupted when Au NPs with various shapes and surface chemistries are introduced.

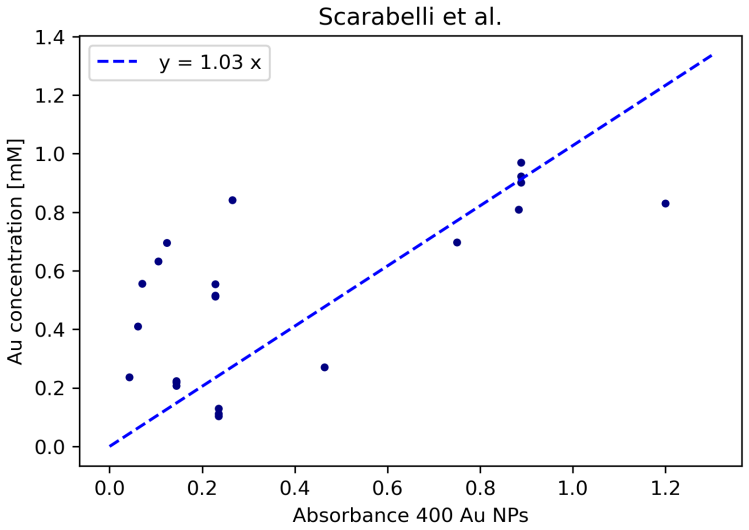

Figure 4.2.4: Scarabelli et al.[27] concludes that absrobance at 400 is propotional to concentration. Here Abs_{400} of all Au NPs are plotted against MP-AES concentration. No clear trends can be observed. $R^2 = 0.36$

Hendel et al[26], represents a modification of Scarabelli et al.s conclusions. The publication concludes that Au concentration could be extracted reliably from $Abs400$ for NPs with similar sizes and surface chemistries. This is extremely similar, as discussed in the previous paragraph, to what Scarabellis dataset actally contained; a comparison of five Au NRs, perhaps with similar surface chemistry and sizes as well. The experimental dataset of this thesis was time-limited and did not include any sets where both size and surface chemistry were the same. However, three subsets of the experimental data were investigated.

The citrate-coated spherical Au NPs of stepwise increasing sizes should have very similar surface chemistry. Figure 4.2.6a has Abs_{400} plotted against MP-AES concentration for this subset of Au NPs. The Au NPs have sizes 17, 27, 29, 37, 47, and 55 nm. In Figure 4.2.6b the data obtained from the largest particles is removed, and a more linear trend is found. Ultimately this supports the conclusions of Hendel et al., as sizes

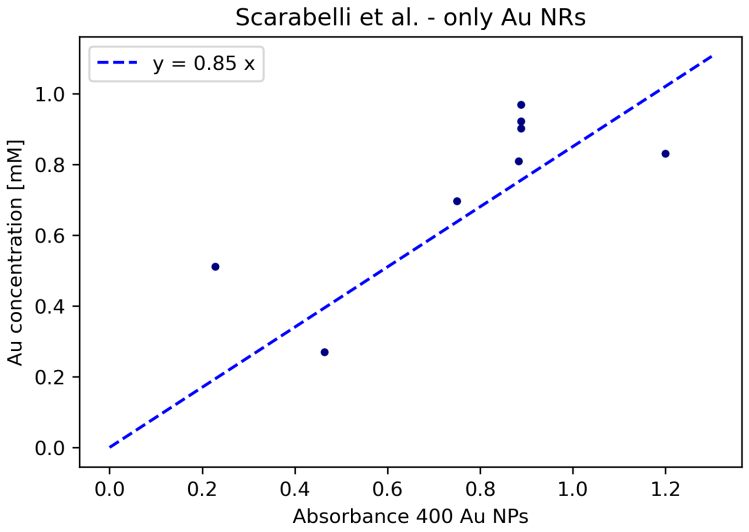

Figure 4.2.5: Absorbance at 400 nm of different Au NRs plotted against Au obtained from MP-AES. $R^2 = 0.96$

are more similar, Au concentration can be extracted more reliably from $Abs400$.

Similar surface chemistries are also produced by seed-mediated growth synthesis. However, the different shapes are obtained based on altering the growth solution with various co-surfactants, pH, and reducing agents. In comparison to the citrate-coated Au NPs, more differences in surface chemistry are thus anticipated between the CTAB-coated Au NPs. Sizes between the CTAB-coated NPs are also of greater variation. Figure 4.2.7 shows the resulting scatterplot when Abs_{400} for all the CTAB coated Au NPs are plotted against MP-AES concentration. Previous Figure 4.2.5 showed a smaller subset of this, with CTAB coated Au NRs plotted against MP-AES concentration. To be brief, these experimental results are in line with Hendel et al. s publication. As the sizes and surface chemistries are more similar, more linear trends between Abs_{400} and Au concentrations are be found.

Roach et al. [29], measures the absorbance of digested Au NPs, to overcome the shape dependency in UV-vis spectra as found by [28]. In Figure 4.2.8, Abs_{400} of digested Au NPs are plotted against the measured MP-AES Au concentration. Trends in this method are found much more linear, in termes of R^2 than Figure 4.2.4 of Scarabellies method. However, R^2 from the linear regression line are more significant than reported by Roach et al., Figure S2.

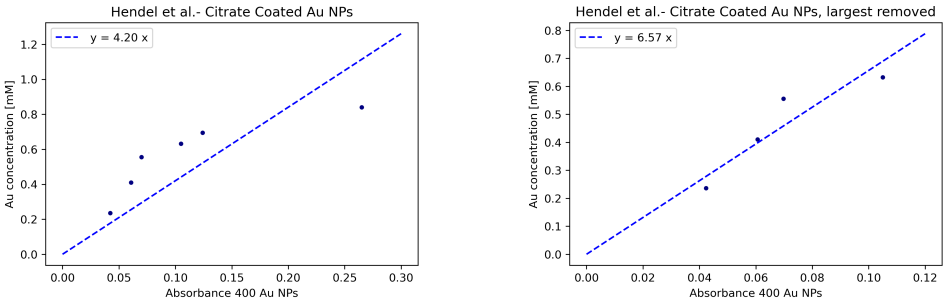

(a) **(b)**

Figure 4.2.6: The citrate coated Au NPs of stepvise increasing sizes have similar surface chemistries. Here their absorebance at 400 nm is plotted against Au concentration obtained from MP-AES. A) Includes all sizes, and have $R^2 = 0.89$. In subfigure B) the two largest sizes are reomved yielding a $R^2 = 0.98$.

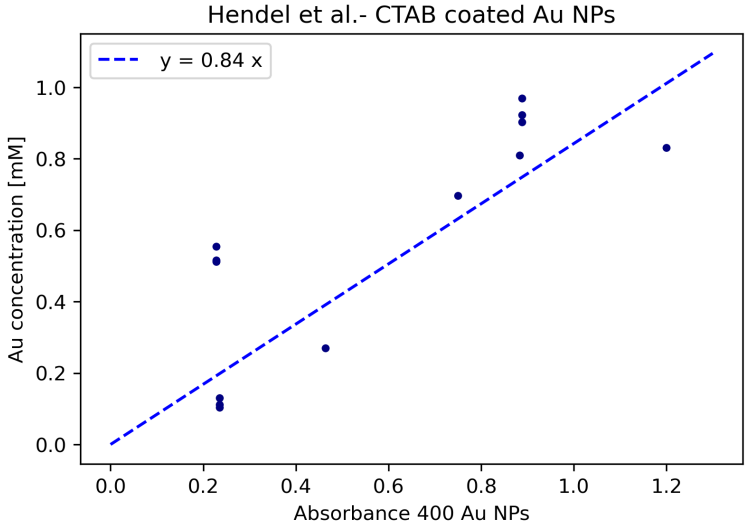

Figure 4.2.7: The CTAB coated Au NPs also have similar surface chemistries. Here their absorebance at 400 nm is plotted against Au concentration obtained from MP-AES. $R^2 = 0.45$

Looking closer at their dataset, it only contains Au NRs made with seed-mediated growth synthesis and slight variations in growth solutions, meaning that the sizes, shapes, and surface chemistry of the NPs are similar. Splitting our data into two subgroups of similar surface chemistries, Figure 4.2.9 plots the abs_{400} of digested citrate-coated Au NPs, and Figure 4.2.10 for CTAB coated Au NPs. The linearity improves in

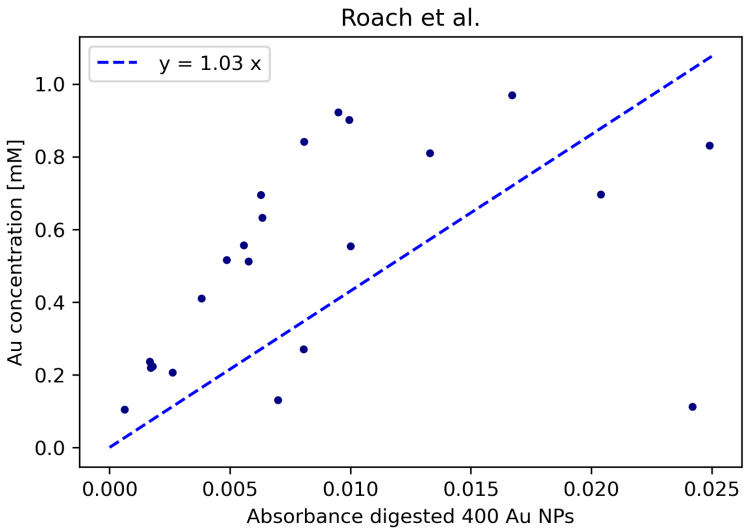

Figure 4.2.8: Roach et al.[29] measure absorbance of the digested NPs to overcome any shape and size dependency. Here absorbance of all NPs are plotted against Au concentration obtained from MP-AES. $R^2 = 0.81$

both subsets. This could ofcurse just be because of less datapoints. However, the citrate-coated NPs show considerably less deviations from the linear regression line. A deeper look at their dataset reveals that it only includes Au NRs produced by seed-mediated growth synthesis and minor differences in growth conditions. As a result, the NPs of Roach et al. s dataset have similar sizes, morphologies, and surface chemistry. Dividing the dataset of this study into subgroups with similar surface chemistries, improves linear dependency in both cases. Figure 4.2.9 plots the abs_{400} of digested citrate-coated Au NPs, and Figure 4.2.10 for CTAB coated Au NPs. Of course, there may be fewer data points to blame for this. However, slopes are significantly different between the two subsets, and especially the citrate-coated NPs show considerably less deviations from the linear regression line with a R^2 value of 0.97. This subset has more similar sizes and shapes than the CTAB subset. Roach et al. also publish the equation of their regression line, but since the dilution factor is not published, the absorbance values don't compare.

Ultimately this study indicates that NP size, shape, and surface chemistry influence the UV-vis absorbance and that there is no reliable universal method for obtaining concentration directly from UV-vis. The outcomes for Hendel et al. and Roach et al. methods are both encouraging. Deviations of fewer than 5% can be accomplished by

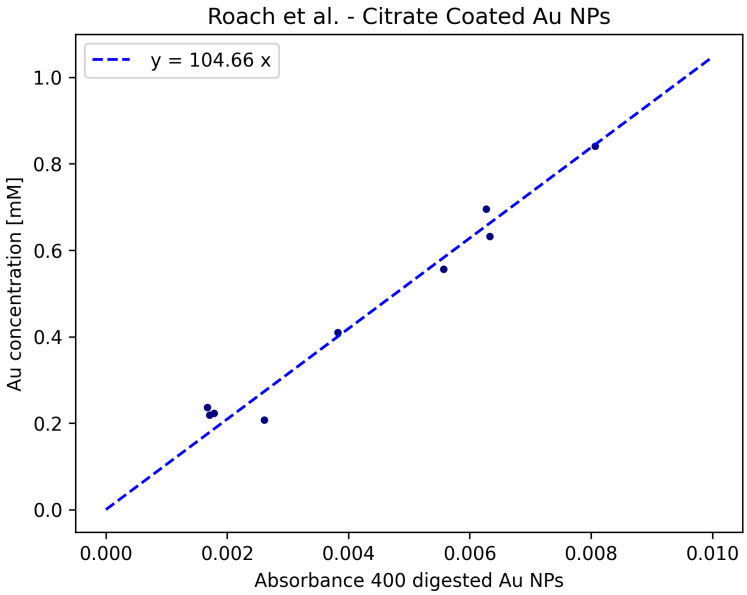

Figure 4.2.9: Absorbance at 400 of digested Citrate coated Au NPs plotted against Au concentration obtained from MP-AES. $R^2 = 0.97$

limiting to one shape and one surface functionalization. The methods are useful because they don't require high-end equipment. The method of Hendel et al. is particularly appealing because it involves measuring bare Au NPs without any sample preparation. However, in order to employ these techniques without the assistance of, for instance, an MP-AES a larger systematic study complete with calibration curves and sample preparation protocols would be required.

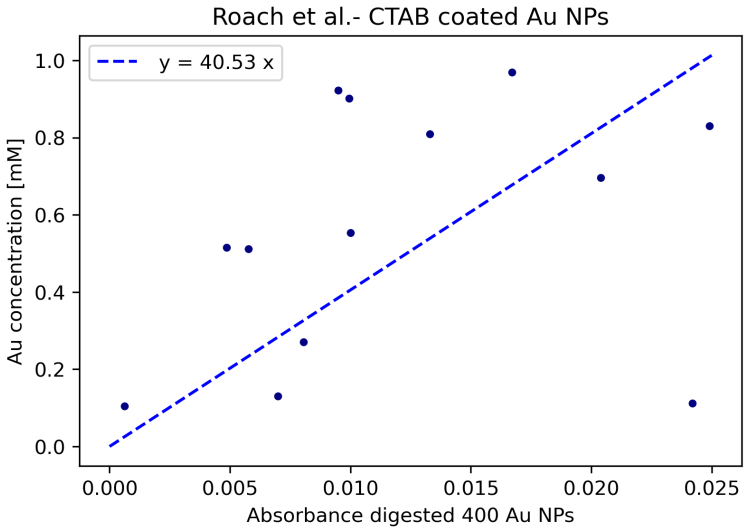

Figure 4.2.10: Absorbance at 400 of digested CTAB coated Au NPs plotted against Au concentration obtained from MP-AES. $R^2 = 0.97$

4.3 Hydrodynamic diameter of Anisotropic Nanostructures

Hydrodynamic diameter is a convenient and powerful tool for monitoring surface chemistry changes, and it is often reported in literature about functionalizing NPs. However, DLS is based on assuming the shape of a perfect sphere, and our research group lacked an optimized protocol for evaluating Au NRs. The CTAB@Au NR OA and CTAB@Au NR TA, as presented in section 4.1, were measured with DLS at different dilutions and detection angles to find a good protocol for characterization. The section also tries to answer questions about measurement reproducibility, the effect of dilutions, the effect of detection angles, and the effect of the weighting method on size distribution.

4.3.1 Within Measurement Reproducibility

Two identical measurments of the same sample were done in the start and end of each measurment to check the within-measurment reproducibility. This is equivalent to measuring the same sample with approxomatly 5 minutes time difference. Our DLS set up allows for detecton angles at back scattering (175 °), Forward scattering (15°) and Side scattering (90 °). However, Zetacells, allowing for combined DLS and ELS measurments, saving time, dont allow for side angle measurements. Backscatter angle were therefore chosen for comparison, and the resulting Hydrodynamic diameters at different dilutions are presented in Figure 4.3.1.

The Au concentration measured by MP-AES of CTAB@Au NRs OA and CTAB@Au NRs TA were 0.16 mg/ml and 0.18 mg/ml respectively. Figure 4.3.1A show that CTAB Au NR OA have high within measurement reproducibility at all dilutions, with the largest deviation of 1.16 nm found at dilution factor 8. In contrast, Figure 4.3.1B shows that as the dilution factor increases, the within measurement reproducibility for CTAB Au NR TA worsens. The difference is 8 nm at dilution factor 8, 107 nm at dilution factor 16, and 58 nm at dilution factor 40.

The difference in zeta potential between the two structures can be a probable explanation for this. The stabilizing CTAB layers are shown in numerous experiments to become unstable at decreasing particle concentrations, leading to particle aggregation[7, 73]. In addition, Tantra et al. [74] studied DLS and ELS of commercially available and stable Au NPs at various concentrations. This study concludes that there is a dilution limit, dependent on the nature of the NPs, where results are consistent. At dilution factors higher than this, sizes increased. Furthermore, Tantra et al. investigated the

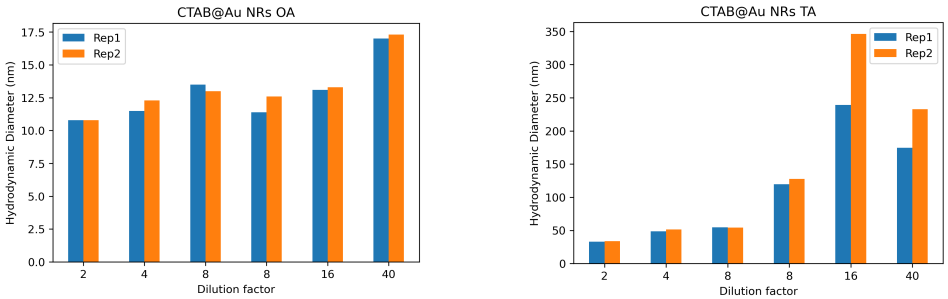

(a) **(b)**

Figure 4.3.1: Within measurement, reproducibility was checked by measuring hydrodynamic diameter at the backscattering angle at each measurement's start and end. Subfigure A shows the resulting measurements for CTRAB@Au NRs OA and Subfigure B CTRAB@Au NRs TA.

DLS and ELS measurements of stable, commercially available Au NPs at varied dilution factors. According to the findings of this study, there is a dilution limit below which results are reliable. The dilution factor of the limit depends on the characteristics of the NPs. None of the NPs of the study were comparable to the NPs of this study. But, ultimately, the results of this study can indicate the importance of getting to know samples of surfactant stabilized Au NPs and avoiding using high dilution factors if colloidal stability is a challenge.

4.3.2 Between Measurement Reproducibility

The functionalization protocol that will be studied in this thesis produces 0.5 ml of Au NPs. The lowest possible dilution factor is therefore 8. Two samples of both rods, on different days, were therefore prepared with dilution factor 8 and measured with the same settings. Figure 4.3.2 shows the resulting hydrodynamic diameters at different angles.

The trends of this section are similar to the previous section and Figure 4.3.1. CTAB@Au NR OA shows good reproducibility, while CTAB@Au NR TA is worse. Also, here it looks like the stability of the sample is crucial for meaningful DLS characterization. If the ZP of surfactant stabilized NPs are low, the sample should be measured at a lower dilution factor.

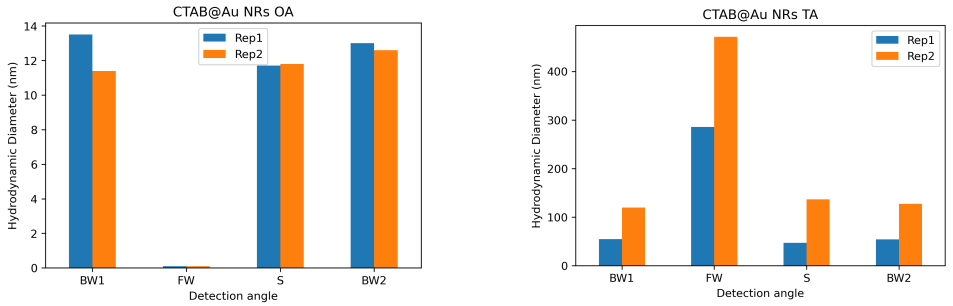

(a) **(b)**

Figure 4.3.2: Two NP samples at dilution factor 8 was measured to check between measurement reproducibility. The resulting measurements at different detection angles are shown in this figure. BW is backward angle, FW is forward angle and S is side angle. Subfigure A is CTAB@Au NRs OA, and subfigure B is CTAB@Au NRs TA.

4.3.3 Effect of Dilution and Angle

The previous two subsections showed that CTAB@Au NR OA had good reproducibility, both between measurements and within. Therefore, to study the dilution factor and angle, these Au NRs were chosen. Figure 4.3.3 presents the acquired correlation functions for each measurement angle and dilution factor. The corresponding hydrodynamic sizes at each angle and dilution are presented in Figure 4.3.4.

The forward angle stands out from the other two angles by showing larger differences between dilution factors. Table 2.2 summarized the pros and cons of the different detection angles. For Au NRs, the forward angle had the advantage of hardly any impact of Brownian motion. The good fit between the calculated correlation functions and the measured values is probably a result of this. However, there are significant differences in measured hydrodynamic sizes between the dilution factors, Figure REF, probably coming from the disadvantages of high sensitivity to any noise and the large impact of multiple scattering.

The backward and side angles show less dependence on the dilution factor, with similar sizes for all dilution factors tested. Figure 4.3.3 shows that the fit between the calculated and measured correlation functions is more deviating than the forward angle. Both these angles show high dependence on the Brownian Rotation found in anisotropic Au NPs, table 2.2.

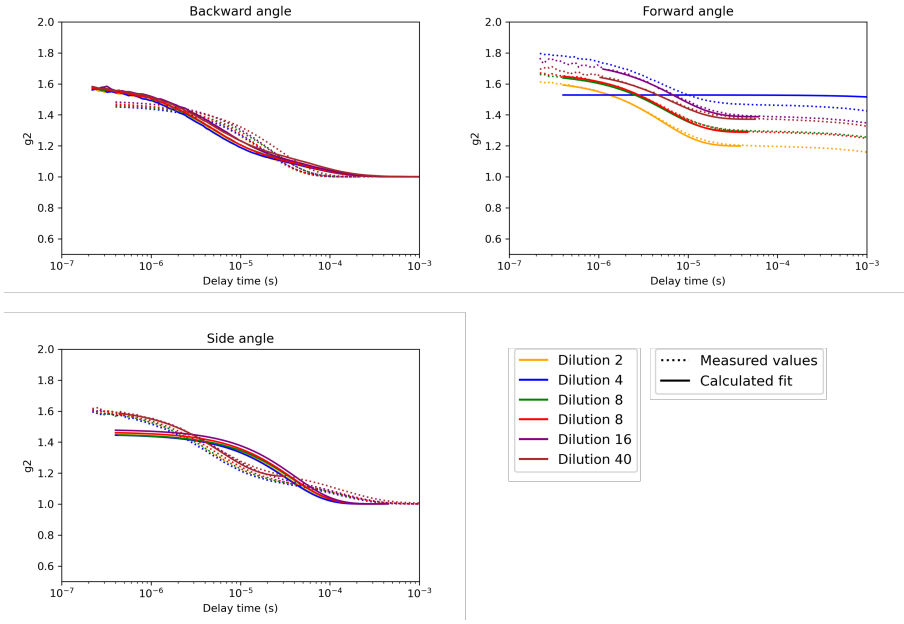

Figure 4.3.3: Correlation functions of CTAB@Au NR OA measured at different dilutions and detector angles.

4.3.4 Effect of Size Distribution Weighting

The DLS software allows for size distribution based on intensity, volume, and number weighting. Figure 4.3.5 presents the resulting size distributions of these modes at all three detection angles for CTAB@Au NRs OA at dilution factor 8.

Theoretically, the largest difference between these different methods for size distribution weighting is that larger-sized particles are more weighted in intensity and volume-weighted distributions. This matches the Size Distribution in figure 4.3.5. When intensity weighting is used, the resulting mean sizes are consistently the largest and the smallest.

Another characteristic that stands out in Figure 4.3.5 is the double peak distribution for intensity weighted size distributions at the backward and side detection angles. At the forward detection angle, there is only one peak to be found. Additionally, the forward angle also shows significantly larger sizes. The theoretical framework included a discussion of how large NPs scatter more light in the forward direction than small NPs. This implies that measurements of the forward angle already include a weighting

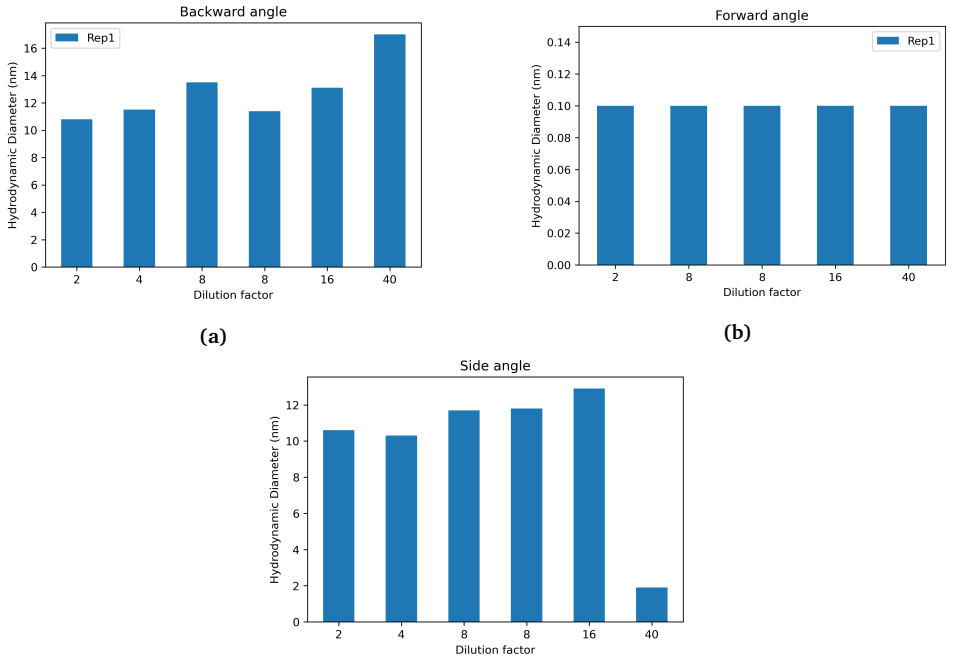

Figure 4.3.4: Hydrodynamic diameter of CTAB@Au NR OA measured at different dilutions and detector angles.

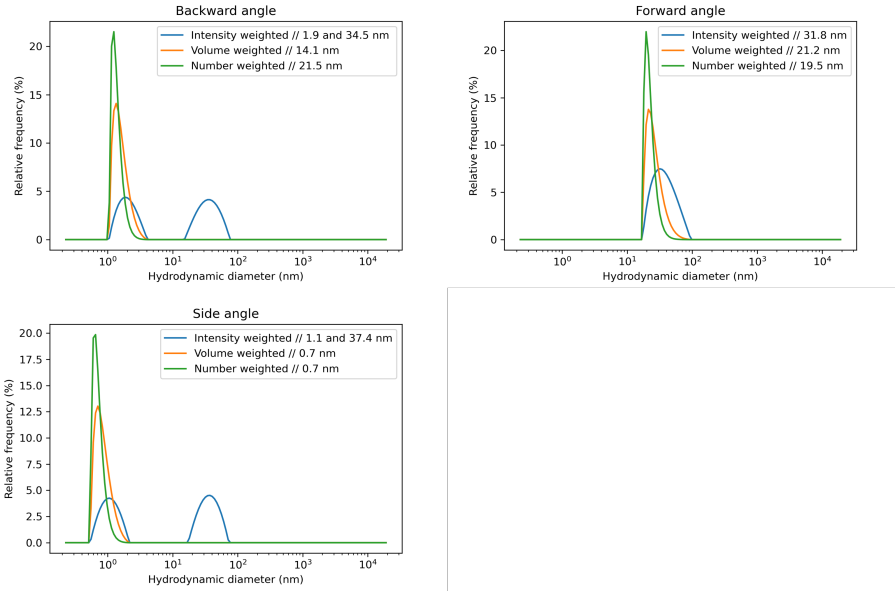

Figure 4.3.5: Size distributions weighted by intensity, volume and number for the three different angles measured for CTAB@Au NR OA at dilution 8.

where large NPs are "biased." However, as discussed in Table 2.2, less of the Brownian rotation is detected at a forward detection angle, which is advantageous for measuring anisotropic Au NPs.

It isn't possible to arrive at any conclusions for optimal universal measurement conditions for any anisotropic Au NPs. This section has shown that it is crucial to get to know the sample of interest and that sample stability is key to having high reproducibility in measurement. Both side and backward angles are great choices of angle, and the results generally indicate that the dilution factor should be as small as possible. The section also showed that multiple measurements should be conducted as quality control. Differences within a measurement will indicate a higher uncertainty and repeatability in hydrodynamic diameter.

4.4 Surface functionalization of Au NPs

The Au NPs presented in the section 4.1 were functionalized with PEG-SH and MUA-SH through a two-step method as described in Section 3.3. This section goes through each step's optimization and reproducibility, followed by a discussion on the shape dependency of functionalization.

4.4.1 Optimalization of PEG Functionalization Step

With an aim to optimize the first step of the PEG and MUA functionalization protocol, different concentrations of PEG solution were added to 0.5 ml of CTAB@Au NRs OA and stirred for 2 hours. Figure 4.4.1 shows the PEG amounts tried and the resulting Uv-vis spectra before and after the functionalization. Figure 4.4.2 presents the corresponding zeta potentials.

The Uv-vis spectra, Figure 4.4.1 show systematic trends depending on PEG amount added. The low amounts of PEG show no clear peak with significant broadening, clearly indicating aggregation in the Au NPs. As more PEG is added, 0.012mg, 0.030 mg, and 0.060 mg, the original shape of the LSPR spectra is back. However, as indicated by the low absorbance, the yield seems low. When 1.28 mg was added, absorbance increased dramatically, and the peak narrowed.

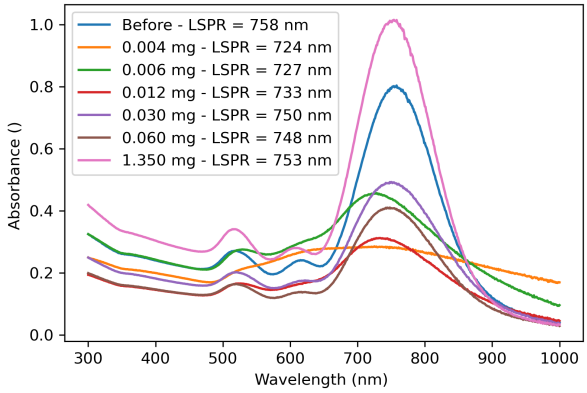

Figure 4.4.1: Uv-vis absorbance spectra of PEG functionalized CTAB@Au NRs OA. The samples were functionalized using an increasing concentration of PEG solution. The unfunctionalized Au NRs is measured in a more diluted solution.

The zeta potential in Figure 4.4.2 does not exhibit the same consistent pattern. Already at 0.006 mg PEG, the zeta potential has changed to -6.9 mV, and higher amounts of PEG show zeta potential in the same order of magnitude, without any clear trends. Methoxy polyethylene glycol (mPEG, MW = 5000, Sigma-Aldrich, USA) was used for this functionalization protocol. The PEG molecule is not a charged molecule, but the methyl group interaction with water gives the PEGylated NPs a slight negative charge. Before functionalization, the Au NPs have a positive charge from CTAB. The inconsistent patterns in zeta potential might indicate that the initial ligand exchange causes the majority of the zeta potential change. However, it is clear from the absorbance spectra that additional ligand exchange is necessary for colloidal stability in order to avoid aggregation.

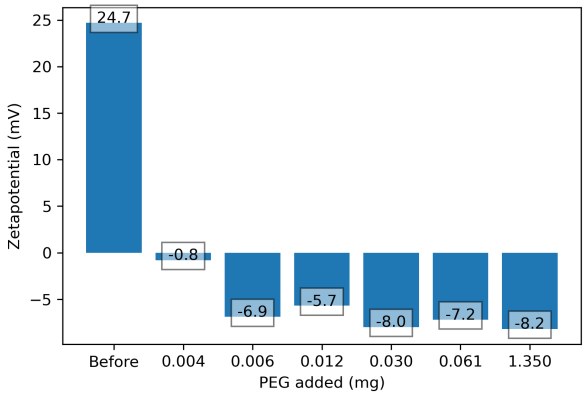

Figure 4.4.2: Zetapotentials of PEG functionalized CTAB@Au NRs OA. The samples were functionalized using an increasing concentration of PEG solution.

Bandyopadhyay et. al.[18] functionalized a similar Au NRs with 1 mg PEG and the same protocol stirring for 2 hours. Similar to our findings, the publication reports only slight shifts in absorbance spectra upon PEGylation. In contrast, zeta potential changes are different. Bandyopadhyay et al. find a zeta potential change from 45 mV to ca 20 mV, considerably different from our findings. Jia et al. [75], a newer publication, also functionalizes Au NRs with the same type of PEG. The aspect ratio of these Au NRs are 4, and their protocol stirs 19 ml 1 mg/ml PEG and 1 ml Au NRs overnight. The resulting zeta potentials here are more similar, reporting a change from ca 20 mV to ca - 5 mV for CTAB coated Au NRs. The protcol use significantly more PEG and longer incubation times than Bandyopadhyay et. al. and our protocol. This could indicate that

more PEG is bound to the NPs in our study and Jie et al.s study. Initial zeta potential or PEG formulation can be other probable reasons explaining the differences.

More concentrations between 0.06 mg and 1.28 mg should be tested in future work. Furthermore, it was planned to use FT-IR data, but downtime on the apparatus made this impossible. FT-IR data would have given valuable input into the chemical composition on the surface, telling us, for example, how much CTAB is left. However, with a clear indication of high yield from UV-vis spectra and stability from ZP measurements, the goals of this engineering approach were met, and it was decided to carry on to the next step in the project. Another takeout is that lower amounts of PEG are insufficient.

4.4.2 Reproducibility of PEG Functionalization

Reproducibility was checked by comparing the functionalized sample from optimization experiments, 1.28 mg/ml PEG with 0.5ml NPs, with three experiments made using 1 ml of NPs and 1 ml of 2.56 mg/ml PEG solution. These samples will be referred to as sample 1, 2, 3, and 4, respectively. Resulting UV-vis spectra and zeta potential are shown in Figures 4.4.3 and 4.4.4.

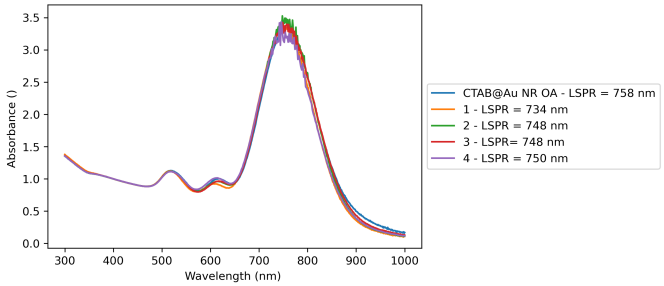

Figure 4.4.3: Reproducibility in PEG functionalization of CTAB@Au NRs OA was tested. Spectras are normalized to Abs_{400}.

The absorbance spectra show good correlations between the experiments. A slight shift in LSPR position is observed between sample 1 and the other three. Yield could not be compared in UV-vis since the samples were measured under different dilutions.

Sample 4 differs significantly from the other experiments in zeta potential, Figure 4.4.4. The four other samples were made using the same stock solution, while the fourth parallel was made using a new one. The larger change in zeta potential indicates more change in surface chemistry, indicating that more PEG had been bound. The new stock solution could ultimately be more concentrated or have less degraded thiols.

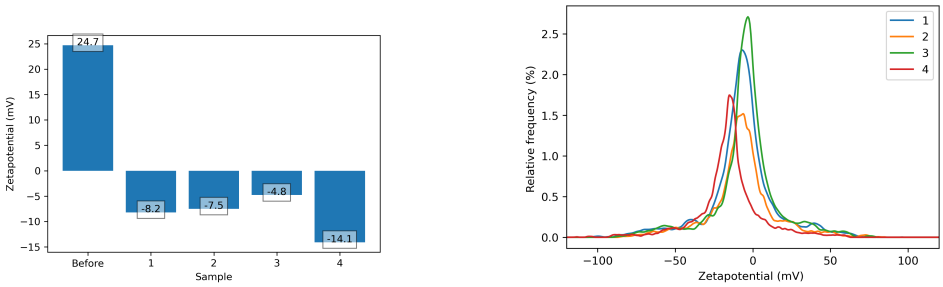

(a) **(b)**

Figure 4.4.4: Zetapotentials (a) and zetapotential distributions(b) of the three experiments with PEG functionalization of CTAB@Au NRs OA.

To fully document the reproducibility of this method, more experiments should have been run. More characterization techniques, such as hydrodynamic diameter, FT-IR, and concentration measurements with Zetaview would also have improved the study. Furthermore, it would have been interesting to further study how and if this process can be scaled up in volume without changing sample properties.

4.4.3 Optimalization of MUA functionalization step

To optimize the MUA functionalization step, PEG-coated CTAB@Au NR OA samples were functionalized after protocol in section 3.3, varying the concentration of MUA with 5, 10, and 20 mM, both at room temperature and 55 $^{\circ}C$. The resulting Uv-vis spectra are presented in Figure 4.4.5. Zeta potential and hydrodynamic diameter is shown in Figure 4.4.6.

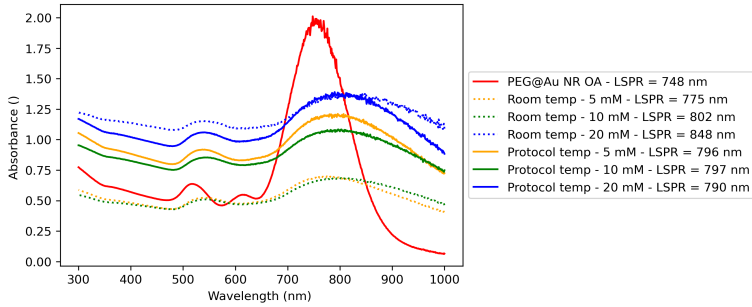

Figure 4.4.5: Absorbance spectra of Au NR OA functionalized with MUA. Three different MUA concentrations, with room temperature, and 55 $^{\circ}C$ were tried for optimalization.

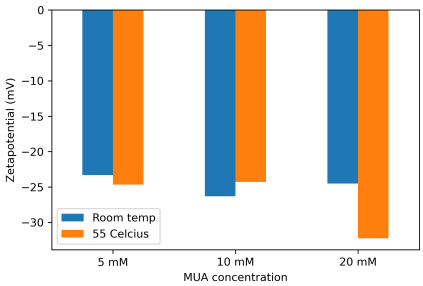

(a) Zetapotentials

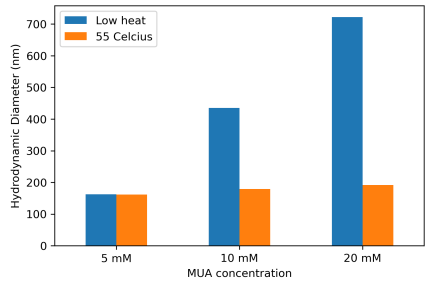

(b) Hydrodynamic diameter

Figure 4.4.6: Zetapotentials (a) and hydrodynamic diameter(b) of the six experiments with optimalization for MUA functionalization of CTAB@Au NRs OA.

The coating with MUA resulted in a broadening of both longitudinal and transverse peaks in the UV-vis spectra for all experiments, Figure 4.4.5. This is in line with the findings of Bandyopadhyay et al.[18]. The optical properties of Au NPs depend on the shape, size, aggregation state, and chemical environment, and there could be multiple reasons for this broadening. The article points to different axes of rotations of the Au NRs due to anisotropy, non-uniform coating, size enlargement, and the polydispersity of the samples.

Carboxy groups are negatively charged in an aqueous solution. The introduction of carboxy groups to Au NPs was therefore expected to decrease the zeta potential of the Au NPs. A zeta potential change greater than or equal to $-10mV$ was found for all the samples, indicating that all samples have been coated with carboxy groups. Looking at the UV-vis spectra, zeta potential, and hydrodynamic diameters, the parallel with 55 $^{\circ}C$ and concentration 20 mM MUA differs from the rest. This sample shows a lower zeta potential, possibly indicating more carboxyl groups bound to the surface, lower hydrodynamic diameter indicating less aggregation, and higher absorbance values indicating higher NP yield. These synthesis conditions will therefore be used moving on further.

4.4.4 Reproducibility in MUA functionalization

To save chemicals, only two experiments were done testing reproducibility in MUA functionalization. The samples were characterized with UV-vis, Figure 4.4.7, and Zeta potential and Hydrodynamic Diameter Figure 4.4.8.

Differences between the experiments are significant in all three characterization

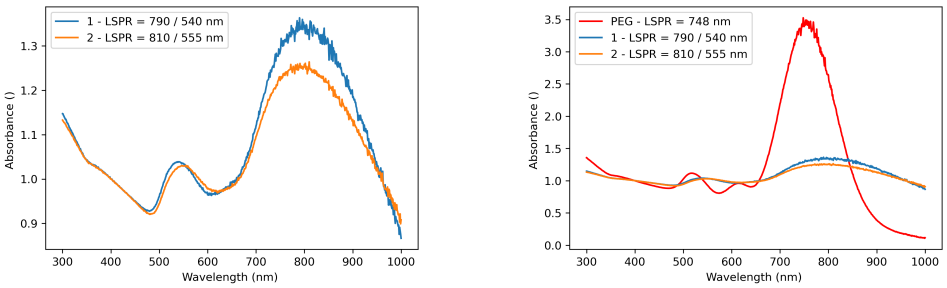

(a) **(b)**

Figure 4.4.7: Reproducibility in MUA functionalization of CTAB@Au NRs OA was tested. Spectras are normalized to Abs_{400}. Subfigure B) also include the PEG functionalized Au NRs OA for comparison.

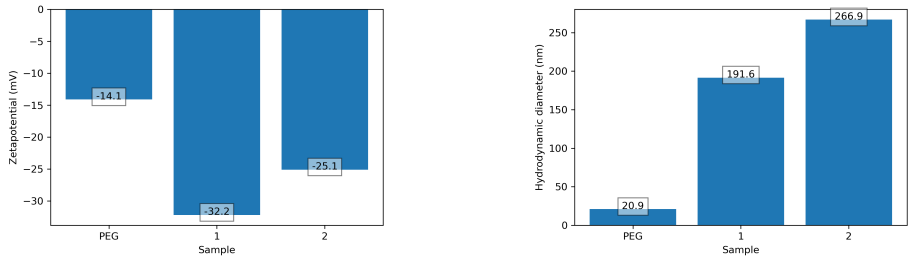

(a) **(b)**

Figure 4.4.8: Zetapotentials (a) and Hydrodynamic diameter(b) of the two experiments testing reproducibility of MUA functionalization.

techniques. Figure 4.4.7 show that Sample 1 has a less red-shifted LSPR-peaks, and a lower hydrodynamic diameter, both indicating less aggregation in the NPs. Furthermore, the more negative zeta potential indicates that more MUA is bound to the NPs.

MUA is an oxygen-sensitive chemical. The MUA stock solution was prepared in the morning. Sample 1 was functionalized directly after the preparation, and sample two followed some hours later. These results could indicate that severe degradation already started occurring in the first hours of MUA in stock solution. The consequences of these differences should have been tested. This could be accomplished, for instance, by comparing the reactivity of the carboxyl groups of the samples. Retout et al.[76] present a method where the carboxyl groups' reactivity is evaluated through conjugation of an organic dye and measurement with UV-vis. Differences in FT-IR spectra could also have given valuable information. However, the results found in this section highlight the importance of preparing MUA fresh before use and the need for adequate storage and handling protocols.

4.4.5 Adjusting PEG-amount to Surface Area Concentration

The available surface area plays a critical role for the application of Au NPs. It is not very common to use surface area concentration to adjust surface functionalization protocols for Au NPs. As discussed in section 4.2.2, the different methods of obtaining this metric gave results varying by multiple orders of magnitude. The motivation of this study was to check if surface area concentration could be an effective metric to adjust the PEG amount for different Au NP samples. The plan was to compare using a fixed amount of PEG in mg, to a fixed amount of PEG chains per surface area. However, later in the process, a calculation mistake was found, and the number of chains per nm^2 is, as a result, not kept fixed. Despite this, these experiments taught us more about the nature of the functionalization protocol.

Figure 4.4.9 show the added PEG chains per surface area in unadjusted experiments and adjusted experiments. The calculations used to find PEG chains per surfacearea is presented in Appendix C. Unadjusted experiments added 2.56 mg PEG to all samples. Figure 4.4.10, and Figure 4.4.11 show the resulting UV-Vis spectra and zeta potentials obtained, respectively.

The UV-vis spectra, Figure 4.4.10, show only slight differences between adjusted and unadjusted amounts for all samples. The largest difference can be found in the CTAB@Au NPs spiky sample, which is the sample where the lowest amount of PEG was added in the adjusted experiments. Zeta potential in Figure 4.4.11 shows considerable

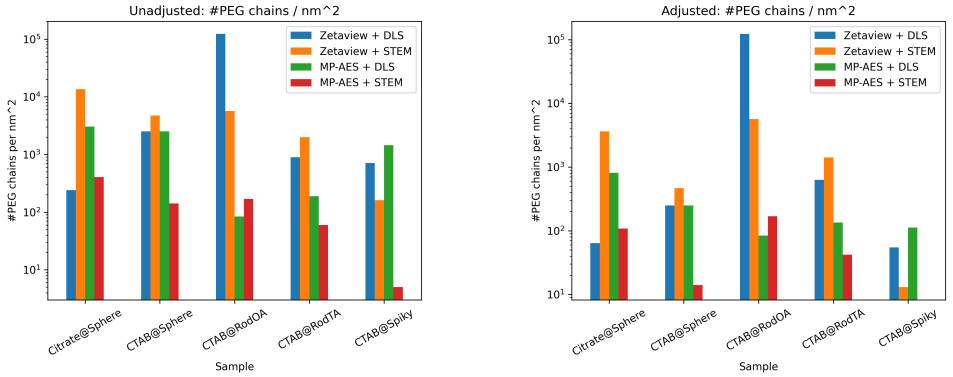

(a) **(b)**

Figure 4.4.9: Added PEG chains per surface area, as calculated with four different methods. Subfigure A) show experiements were 2.56 mg PEG is added. Subfigure B) show adjusted experiments. These should have been adjusted to the number of chains for CTAB@Au NRs OA measured with MP-AES and STEM. However, calculation mistakes were found. The added amount in mg for adjusted experiments are 0.68 mg for Citrate@Au NSs, 0.25 mg for CTAB@Au NSs, 2.56 mg for CTAB@Au NRs OA, 1.80 mg for CTAB@Au NRs TA, and 0.20 mg for CTAB@Au NPs spiky. Numbers of these plots are shown in table 4.3.

Table 4.3: Calculated number of added PEG chains per surface area for the two experiments. A bar plot of this data is shown in Figure 4.4.9. Calculations are explained in Appendix C

Parallel	**Sample**	**Zetaview + DLS**	**Zetaview + STEM**	**MP-AES + DLS**	**MP-AES + STEM**
Adjusted	Citrate@Au NSs	64	3 625	813	108
	CTAB@Au NSs	250	467	249	14
	CTAB@Au NRs OA	122 471	5 643	84	169
	CTAB@Au NRs TA	627	1 407	134	42
	CTAB@Au NPs spiky	55	13	112	0
Unadjusted	Citrate@Au NSs	241	13 575	3 045	406
	CTAB@Au NSs	2 524	4 726	2 520	141
	CTAB@Au NRs OA	122 471	5 643	84	169
	CTAB@Au NRs TA	892	2 001	190	60
	CTAB@Au NPs spiky	708	161	1 442	5

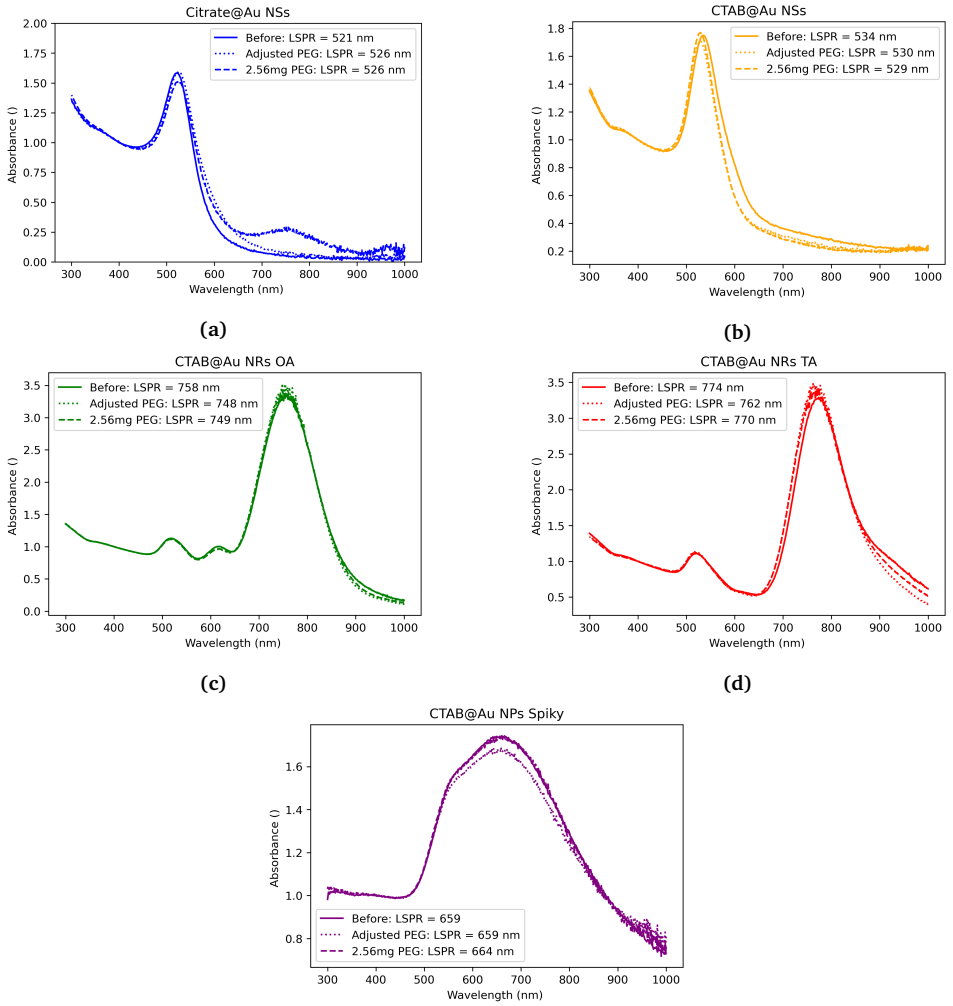

Figure 4.4.10: Normalized Uv-vis absorption spectra of all shapes functionalized with adjusted or unadjusted amounts of PEG.

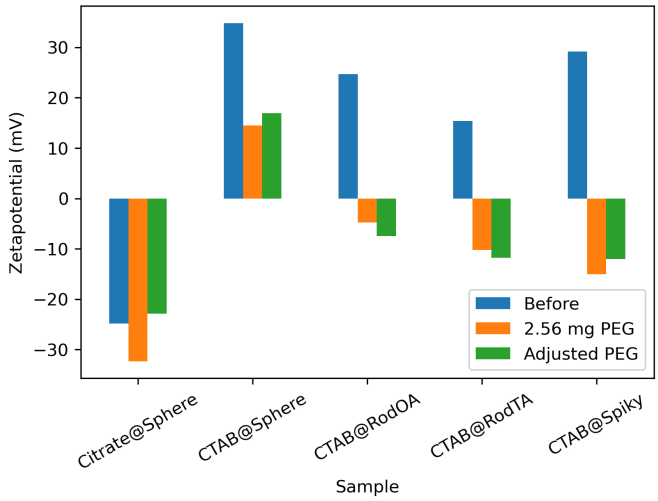

Figure 4.4.11: Resulting zetapotentials for PEG functionalization with and witouth adjusting PEG amounts.

changes in zeta potential for all samples, indicating successful surface functionalization. Citrate@Au NSs, CTAB@Au NSs, and CTAB@Au NPs spiky all show the largest change when adding 2.56 mg PEG, the parallel adding the highest amount. A slightly lower change in zeta potential is measured for the adjusted parallel in the Au NRs. However, two experiments of CTAB@Au NRs OA add the same amount, indicating that this difference is within the variances of reproducibility.

Figure 4.4.9 shows the number of chains added per nm^2 in each parallel using the four different as discussed in section 4.2.2. An excess of PEG chains is needed for the surface functionalization of PEG. For reference, only found a few publications using the metric of PEG chains per nm^2 were found. Kinnear et al. state that a traditional one-step method to functionalize Au NPs with excess PEG uses 100 PEG per nm^2[77]. The article compares the traditional method with a two-step method using only 10 PEG chains per nm^2. Xia et al. study the coverage density of PEG on Au NPs and concluded that it is dependent on the initial capping ligand and NP shape[58]. The resulting chains per nm^2 were found to be 1.63 for citrate-capped AuNPs and 0.052 for CTAB-capped AuNRs. Xia et al. use STEM and ICP-MS to find surface area concentration.

Since none of the samples or methods have a constant or even comparable amount of chains added per nm^2, it is hard to pinpoint any specific trends. However, the number of added chains based on MP-AES and STEM methods stands out from the

rest, being significantly lower. In the adjusted experiments, 14 $chains/nm^2$ is added for citrate@Au NSs, 42 for CTAB@Au NRs TA, and less than 1 for CTAB@Au NPs spiky. Compared to the literature outlined in the paragraph above, this is low. All the samples also showed good conservation of LSPR properties and considerable zeta potential changes. It is, therefore, likely that this STEM+MP-AES method positively overestimates surface area per nm^2.

Even though a study with some unsystematic characteristics, it can be used to indicate that finding and using a threshold fixed PEG amount is efficient. The NPs in this study had concentrations in the same order of magnitude, between 0.6 mg/ml to 4.7 mg/ml measured with MP-AES, and $e9$ to $e10$ number of particles per ml measured with Zetaview. The amount of chemicals saved if adjusted to surface area is minimal, and using fixed amounts is more time-efficient.

4.4.6 Shape dependency in PEG/MUA functionalization

The synthesis procedures, as found in Section 4.4.1 and Section 4.4.3, were applied to the rest of the Au NPs presented in Section 4.1. Figure 4.4.12 presents UV-vis absorbance spectra at each step in the functionalization. Figure 4.4.13 and 4.4.14 present the resulting zeta potentials and hydrodynamic diameters, respectively.

Upon step 1, surface functionalization with PEG, Figure 4.4.12 shows that all shapes keep the same characteristic UV-vis absorbance spectra. These findings are in line with previous work on this method. Thierry et al.[57] functionalize CTAB coated Au NRs, and report no change in the transverse and longitudinal plasmon band shapes and positions, arguing that this indicates an absence of aggregation. Bandyopadhyay et al.s[18] work include surface functionalization of five different shaped Au NPs, shows that UV-vis shapes and peak positions remain for all shapes.

Hydrodynamic diameters in Bandyopadhyay et al. slightly increase for all shapes but the bypyramids. Figure 4.4.14 showed the same incremental changes in hydrodynamic diameter for the Au NRs and the spiky structures. However, both spherical structures showed a large increase in size. Since the LSPR-peaks are narrow and at the same position, aggregation is unlikely. The large measurement of size could be because of contaminations such as free PEG in the solution. Only one round of centrifugation were conducted. Extra cleaning by centrifugation and repeat measurements would have made it possible to check if contaminations was the reason for the large size. In further studies, it is of strong recommendation to do so if such big sizes are observed. The fact that zeta potential and hydrodynamic diameter are based on measuring a perfect sphere

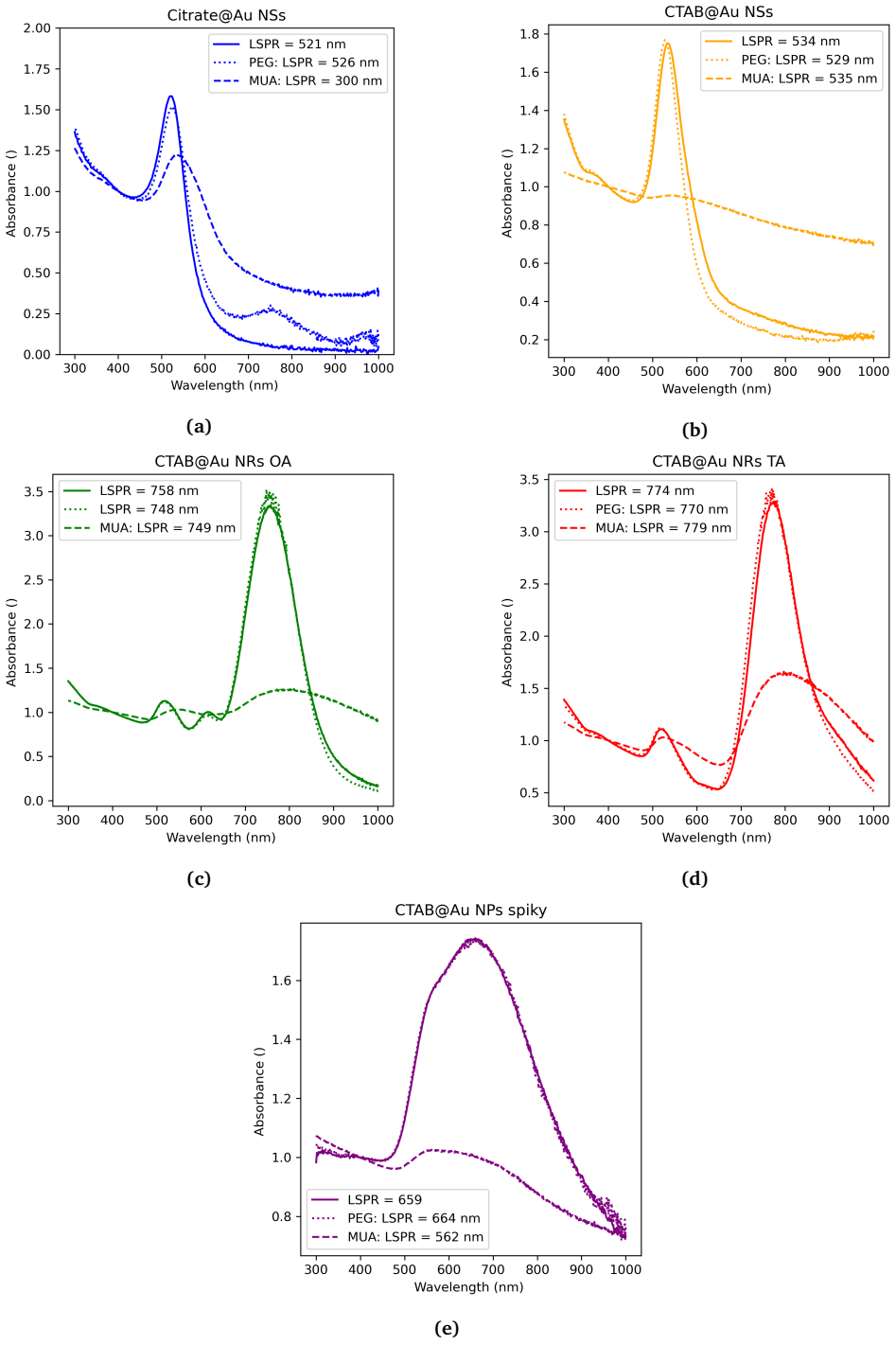

Figure 4.4.12: Normalized Uv-vis absorption spectra of all shapes functionalized stepvise with PEG and MUA.

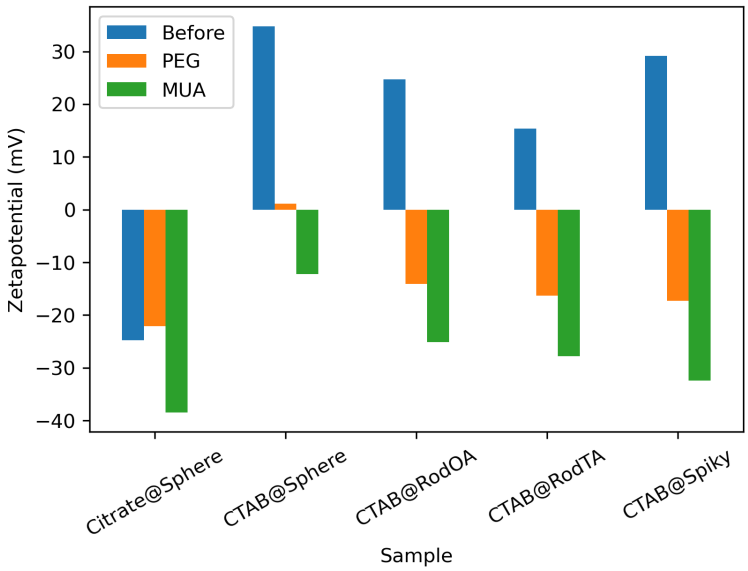

Figure 4.4.13: Zeta potentials of all shapes functionalized stepvise with PEG and MUA.

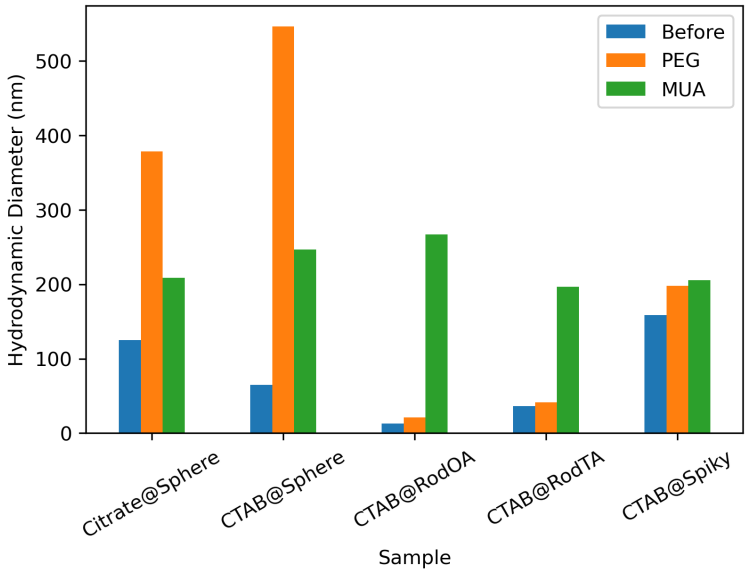

Figure 4.4.14: Hydrodynamic diameter of all shapes functionalized stepvise with PEG and MUA.

should also be borne in mind. The anisotropic samples are therefore not necessarily comparable to the isotropic ones.

Figure 4.4.13 shows how Citrate@Au NPs following PEG functionalization stand out from the other NPs in terms of zeta potential. The CTAB coated structures have changes in zeta potential of -34 mV for CTAB@Au NSs, -39 mV for CTAB@Au NRs OA, -32 mV for CTAB@Au NRs TA, and -48 mV for CTAB@Au NPs spiky. In contrast, Citrate@Au NSs show a slight increase, + 2 mV, upon ligand exchange with PEG. Bandyopadhyay et al.s work also report the same positive increase in zeta potential for Citrate coated Au NPs. However, as pointed out in the section about optimization of PEG functionalization, larger zeta potential changes are found for the CTAB coated structures of this work, compared to Bandyopadhyay et al. Ultimately, these results could indicate that initial surface charge is the most important factor, rather than Au NP shape or concentration when functionalizing with PEG.

As the shapes are functionalized with MUA, Figure 4.4.12 shows that all shapes have a significant broadening of the peaks in the absorbance spectra. Looking at Figure 4.5.5, plotting the MUA functionalized Au NPs with a more detailed y-axis, Citrate@Au NPs, and the two Au NRs still show distinct peaks with the same characteristic shape. CTAB@Au NSs and CTAB@Au NPs spiky are the most polydisperse samples, and both show distinct changes in absorbance spectra geometry and peak position. Zeta potential change, Figure 4.4.13, is similar for all shapes. Hydrodynamic diameter, Figure 4.4.14, significantly decreases for the spherical NPs, significantly increases for rod NPs, and stays the same for the spiky structure.

In the theoretical framework, it was discussed how previous works have found that the large size of PEG makes it difficult to penetrate the dense packing of CTAB on 111 facet on anisotropic Au NRs, resulting in incomplete removal of CTAB[7]. Therefore, it was predicted that the anisotropic Au NPs would have more considerable changes in physicochemical properties, than the isotropic NPs, upon functionalization with MUA. The findings of this study do not follow this pattern. Uv-vis spectra, the Au NRs, as well as the citrate@Au NSs, show better conservation of LSPR-peaks. Au NRs also show the lowest change in zeta potential. Conclusions about changes in hydrodynamic diameter are difficult to reach. As previously mentioned, any contamination can significantly increase the observed hydrodynamic diameter. Ethanol, used to dissolve MUA, is a large molecule, and even the most minor amounts could affect the DLS measurement. Extra cleaning steps and repeat measurements should therefore have been included in this study. Furthermore, the same argument of zeta potential and hydrodynamic diameter being based on measuring a perfect sphere also apply here. The anisotropic samples are

therefore not necessarily comparable to the isotropic ones. In other words, this study can neither support nor contradict previous work's findings.

The key concept of this two-step procedure was that the first step of ligand exchange with PEG should introduce steric repulsion and colloidal stability upon functionalization with MUA. Bandyopadhyay et al. Figure S2 shows a similar broadening as observed in this study. The publication, as discussed previously, section 4.4.3, point to different axes of rotations of the Au NRs due to anisotropy, non-uniform coating, size enlargement (DLS data), and the polydispersity of the samples, to explain the broadening of the UV-vis spectra. In contrast, the results of Thierry et al. show much better conservation of LSPR -properties for a CTAB coated Au NRs, definitely qualifying as an anisotropic shape. Thierry et al. s work could, in other words, indicate that better preservation of UV-vis spectra is possible and that NP aggregation also could be a possible explanation for the broadening in LSPR-peaks. Both Thierry et al. and Bandyopadhyay et al.s explanations are probable. In future studies, it would therefore be interesting to look closer at the colloidal stability of the PEG-coated Au NPs. Has the ligand exchange introduced enough steric repulsion to prevent aggregation upon functionalizing with MUA? In addition, more methods for sonication could be interesting to study. In Thierry et al.s work, the PEGylated Au NRs were first mixed with the MUA solution, then sonicated for 30 minutes at 25 $^{\circ}C$, before the temperature was increased to 55 $^{\circ}C$ and sonicated for 60 minutes to enhance the ligand exchange process. The solution was kept at room temperature overnight, after which sedimentation of the rods could be observed. In the work of this thesis, and Bandyopadhyay et al.s work, the PEGylated Au NPs are sonicated for 2 hours at 55 $^{\circ}C$. Investigating more MUA amounts and if there is some shape dependency in MUA amount could also be of interest.

Both Thierry et al.s and Bandyopadhyay et al.s publications include X-ray photoelectron spectroscopy (XPS) analysis. Bromide (Br) signal is utilized to detect the presence of CTAB. Both publications demonstrate that the Br signal is reduced after PEG functionalization and completely removed upon MUA functionalization. Further studies would be strengthened by including characterization of the surface chemistry.

In conclusion, five Au NPs of different shapes and initial surface chemistry have successfully been surface-functionalized through a two-step ligand exchange with PEG and MUA. No clear trends depending on the NP shape were found in the study. In the PEG functionalization step, all shapes keep their LSPR properties, and indications of dependence on the initial surface charge were found. A large decrease in zeta potential, indicating successful grafting of MUA with carboxyl groups, was found for all shapes in step 2. In this step, a significant broadening of absorbance spectra appeared, and it was

discussed that further studies would be needed to identify the reason for this. Results by Thierry et al. indicated that better LSPR properties are possible. At the same time, Bandyopadhyay et al.s work argue that the broadening of the UV-vis spectra comes from different axes of rotations due to anisotropy, non-uniform coating, size enlargement, and the polydispersity of the samples.

4.5 Biosensing Application with Biotin and Streptavidin

In order to test the Au NPs in a model biosensing system with Biotin and Streptavidin, a method, as published by Aslan et al.[65], and modified by Hinman et al.[67], was applied.

4.5.1 Optimalization of Biotynelation Protocol

The method was made for Turkevich Au NPs functionalized with long-chain carboxyl-terminated alkane thiol MHDA and Tween 20. Therefore, the PEG/MUA functionalized Citarate@Au NP samples were chosen for optimization experiments. Three incubation times, as presented in Table 4.4 were tried. The short incubation times are from Aslan et al.[65], and long incubation times are from Hinman et al.[67]. A mid point was also tested. Figure 4.5.1 presents the resulting UV-vis spectra before and after the Biotynelation. Figure 4.5.2 shows the resulting zeta potential and hydrodynamic diameters.

Table 4.4: The incubation times were varied to optimize protocol for Biotynelation. All times are in minutes. Short incubation times are from Aslan et al.[65], and long incubation times are from Hinman et al.[67].

Incubation time	**Sample 1** -Short	**Sample 2** -Mid	**Sample 3** -Long
with NHS/EDC	5	10	15
with AEE/BA	10	60	120

A schematic of the protocol was shown in Figure 3.4.1. The first step consists of cleaning the Au NPs three times in PBT with centrifugation. Figure 4.5.1 shows that a large drop in absorbance and redshift in LSPR peak position occur already after this step. The buffer includes large amounts of salts, suppressing the electric double layer of the NP, and, therfore challenging the colloidal stability of the Au NPs. The loss in stability could induce aggregation shown as a redshift and broadening of the LSPR-peak. In addition, the centrifugation relies on spinning the NPs down to a pellet and removing the supernatant by pipetting; losing NPs is therefore expected and explains a lowering in absorbance values.

For the biotinylation protocol, the longer the incubation time used, the less redshift

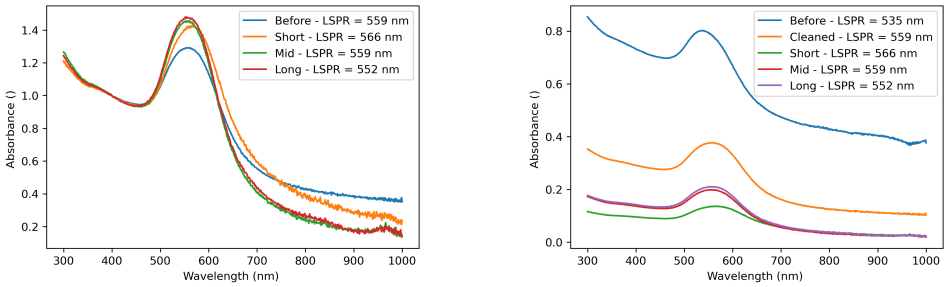

(a) **(b)**

Figure 4.5.1: Uv-vis absorbance spectra of the three experiments for optimalization of biotynelation of Au NPs. Short, Mid and Long is different incubation times as described in Table 4.4. Subfigura A) is normalized to absorbance at 400nm. Subfigure B) is the raw data.

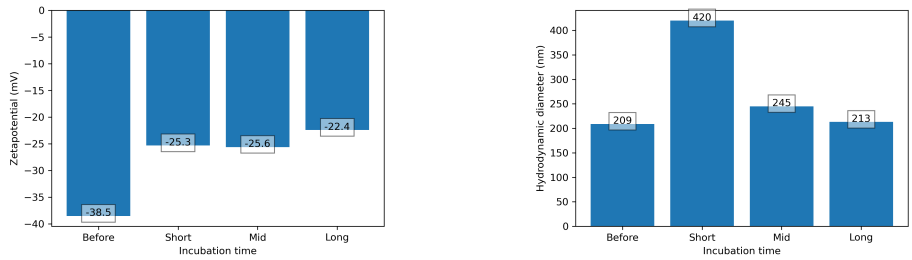

(a) **(b)**

Figure 4.5.2: Zetapotentials (a) and hydrodynamic diameter(b) of the three experiments for optimalization of biotynelation of Au NPs. The experiments have different incubation times as described in Table 4.4.

and broadening of the LSPR-peak is observed. The Uv-vis spectra, Figure 4.5.1, show that Mid and Long incubation times give a blue shift in LSPR-peak position compared to the cleaned NPs before biotinylation. The short incubation time gives a further redshift, indicating even more aggregation in the Au NPs. Aslan et al. shows that the activation of carboxy groups in the NHS/EDC step in the protocol induces aggregation. The article argues that this is because of the reduction in surface charge. In the biotinylation step surface charge is increased, allowing for redispersion of the NPs. The differences in LSPR-peak could therefore indicate that more biotin is bound for longer incubation times. This same trend is found for hydrodynamic diameter; short incubation time shows ca twice as high size, indicating significant aggregation. Differences between Mid and Long incubation times are minor. The zeta potentials don't show significant differences between samples.

In terms of colloidal stability, the results published by Aslan et al.[65] and Hinman et al.[67] show less of a redshift after the Biotynelation protocol. Both report LSPR-position at ca 525 nm for the MHDA-Au NPs before biotinylation and ca 530 nm after the biotinylation. Aslan et al. argue that the difference in LSPR-position between unmodified gold nanoparticles and biotinylated gold nanoparticles is due to the local increase in the refractive index caused by the addition of ligand layers to the surface of gold nanoparticles. In contrast, the results of this thesis show a redshift to LSPR-position of 555 nm upon cleaning with PBT buffer, and a redshift to 552 nm after Biotynelation. This could be because the PEG/MUA functionalized Citrate@Au NPs have lower stability in the buffer than the NPs used in previous work. Another work by Aslan et al.[78] backs up this argument, testing the stability of bare Au NPs and Au NPs with a physisorbed layer of Tween 20 on the surface. Their work finds that having both Tween 20 on the surface and in the buffer solutions preserves the stability of the Au NPs. When Tween 20 was not present in buffer solutions, gold nanoparticles aggregated irreversibly.

A stability assay test, as done in Hinman et al.[67](Figure S2) would have given valuable information on the colloidal stability of the Au NPs of this thesis. The stability before and after the biotinylation could also be compared if these tests were done. However, because of the limited time aspect of a master thesis, and since the LSPR-peak still was distinct and visible, it was decided to carry on with the synthesis conditions of the long incubation time.

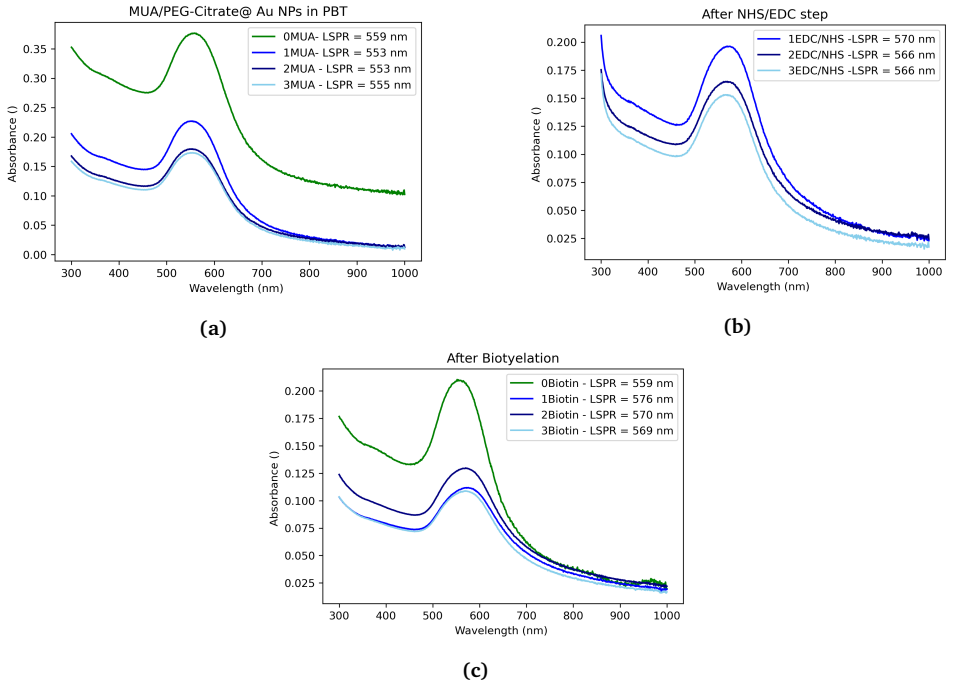

Figure 4.5.3: Uv-vis spectra at each step in Biotin functionalization protocol. Sample 0 is from optimalization experiements. Samples 1-3 were done in parallel.

4.5.2 Reproducibility

Three experiments of PEG/MUA functionalized Citrate@Au NP samples were biotinylated and compared to the optimization experiments to check reproducibility. Figure 4.5.3 shows the resulting UV-vis spectra at each step in the protocol; after cleaning with PBT, after incubation with NHS/EDC(optimization experiment data is missing), and after the biotinylation. Figure 4.5.4 presents zeta potential and hydrodynamic diameter.

There are some important differences between the experiments. First, the LSPR position is already different after the cleaning step with PBT. This supports the findings from the optimization experiment that colloidal stability is challenging. In further studies, colloidal stability should be studied, and different buffers or chemisorption with tween 20 prior to cleaning can be tried to improve the stability.

Next, Figure 4.5.3 show differences in absorbance values. The optimization experiment has a much higher absorbance value than the new experiments. The absorbance can indicate the yield and, therfore, the loss of Au NPs. The difference is seen already

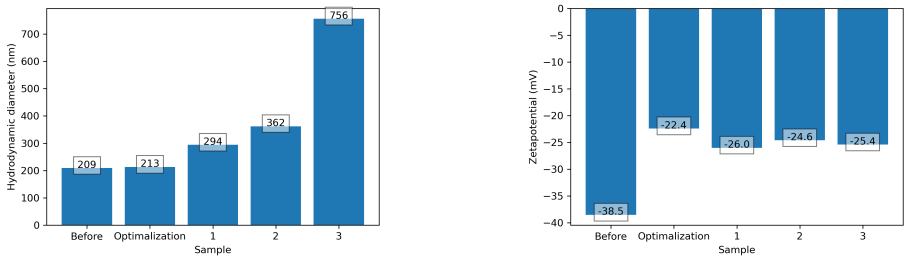

(a) **(b)**

Figure 4.5.4: Zetapotentials (a) and hydrodynamic diameter(b) of four experiments of biotynelated PEG/MUA coated Citrate@Au NPs. Sample 0 is from optimalization experiements. Samples 1-3 were done in parallel.

after cleaning. Adjusting the NP amount after cleaning could be a measure to have more reproducible results. In addition, the protocol contains many rounds of manual pipetting, making it impossible to avoid some loss of NPs throughout the procedure.

Figure 4.5.4a shows that zeta potentials are very similar. Hydrodynamic diameters, on the other hand, show larger sizes in the new experiments and an especially large size for experiment 3, indicating aggregation.

To conclude, the biotinylation protocol needs more optimization and further studies to improve reproducibility. Especially the colloidal stability shows concern. Moving on, in this thesis, the method will be applied without further improvement. Quality control must therefore be thoroughly discussed, both in the biotinylation procedure and later in the model biosensing system with streptavidin.

4.5.3 Biotynelation of all shapes

Synthesis conditions of Hinman et al.[67], as found in the previous section, was used to Biotynelate the Au NPs of various shapes. The resulting UV-vis spectra at each point in functionalization are presented in Figure 4.5.5. Zeta potential and Hydrodynamic diameters are presented in Figure 4.5.6 and 4.5.7.

The UV-vis spectra generally show the same trend in all shapes; A redshift in LSPR position accompanied by broadening upon washing with PBT and incubation with EDC/NHS. After incubation with biotin and AEE, the peak shifts back closer to the original position. As discussed in previous sections, the shift upon washing in the buffer is not seen in Aslan et al., and Hinman et al. Future work should study and improve the colloidal stability to optimize this protocol step. For the following steps, the same

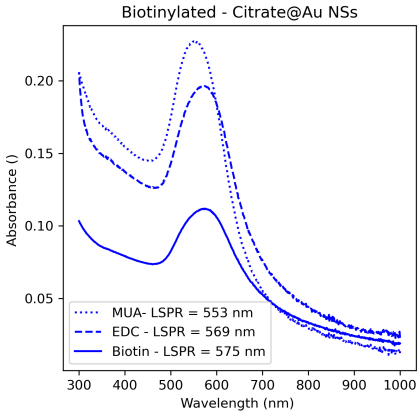

(a)

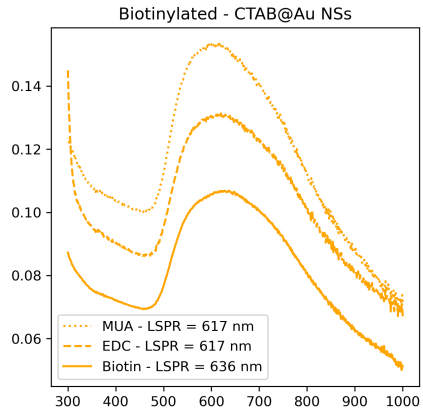

(b)

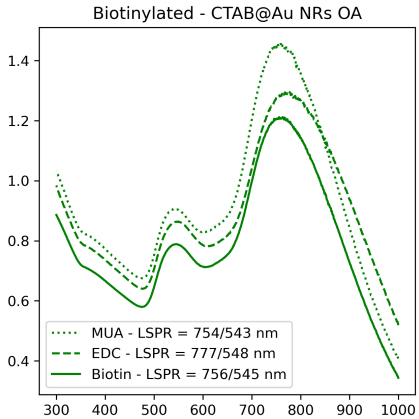

(c)

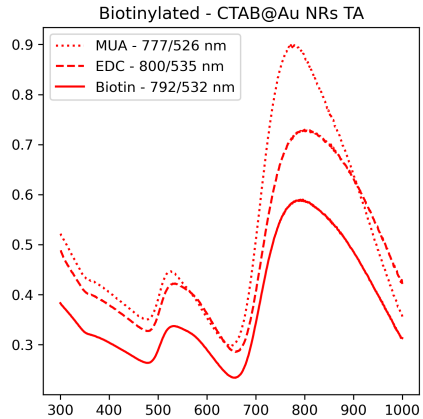

(d)

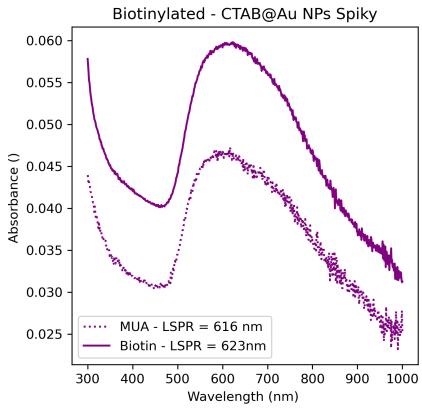

(e)

Figure 4.5.5: Uv-vis stepvise after biotynalation of MUA functionalized Au NPs. UV-vis at NHS/EDC step is missing for sample CTAB@Au NPs spiky.

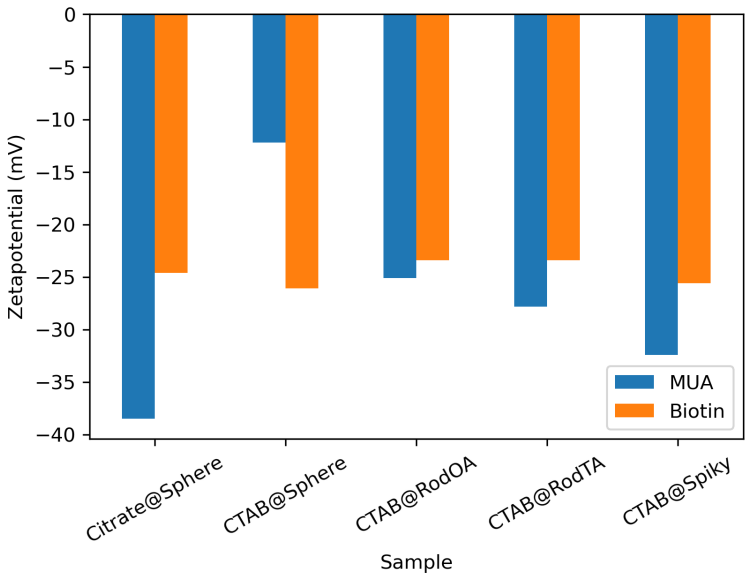

Figure 4.5.6: Resulting zetapotential after biotynalation of MUA functionalized Au NPs.

trend is found both in Aslan et al. and Hinman et al.s publications. Aslan et al. argue that the active esters formed when Au NPs with carboxy groups react with NHS and EDC will reduce the surface charge and thereby induce aggregation. In the next step, biotin is attached to the carboxy groups, followed by a shift back to the original LSPR position. This indicates successful redispersion of the NPs.

Aslan et al. and Hinman et al. have not published zeta potential and hydrodynamic diameter upon functionalization. Figure 4.5.6 shows that all shapes have a change in zeta potential. However, no clear trends can be observed. The Au NRs and Au spiky structure show slight increases in zeta potential of +3 mV, + 4mV, and +6mV, respectively. The spherical structures show more considerable changes, -14 mV for CTAB@sphere and +12 for citrate@sphere. Figure 4.5.7 shows the measured hydrodynamic diameters upon biotinylation, also without clear trends. Both Au NRs, and the CTAB coated NSs, decrease in size. Citrate@Au NSs show a considerable increase in size, while the spiky structure increases slightly.

It is hard to pinpoint any clear reasons and trends governing biotinylation. In theory, the number of carboxyl groups could decide how much biotin can be bound to the Au NPs. Different amounts of biotin could be tested to check this. Testing carboxy groups' reactivity, for example, with Retout et al.s method[76] as discussed in Section 4.4.4,

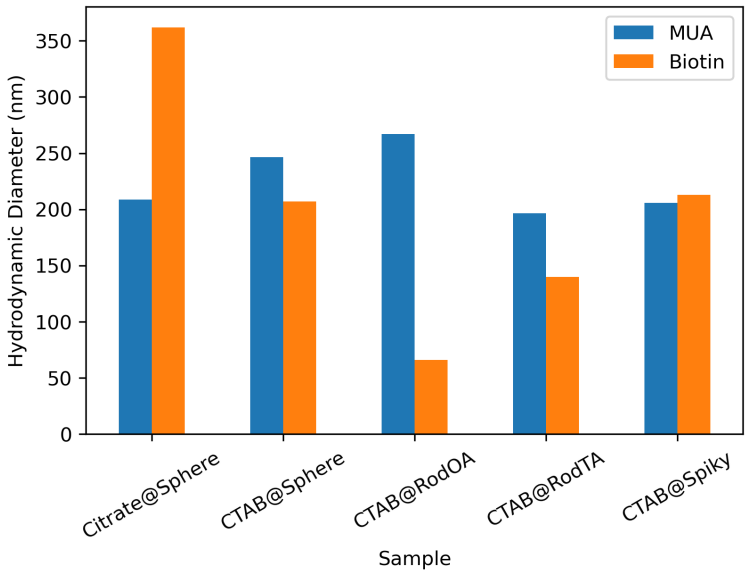

Figure 4.5.7: Resulting hydrodynmaic diameter after biotynalation of MUA functionalized Au NPs.

would also give valuable information. Furthermore, some samples could have free NPs without carboxyl groups. This would contribute to weight down the changes upon biotinylation. As pointed to in the previous section, characterization of surface chemicals would also here be an excellent complement to the study. However, optimization of the model protein system was not the aim of this master thesis. The following section will show aggregation with Streptavidin.

4.5.4 Aggregation with Streptavidin

Biotynelated Citrate@Au NSs and CTAB@Au NRs OA were chosen for comparison in the model biosensing system with streptavidin. Figures 4.5.8 and 4.5.9 show the resulting UV-vis spectra, normalized and unnormalized, for the Au NSs. As the figure indicates, no noticeable aggregation can be observed. A different result is obtained by employing the Au NRs. Figure 4.5.10 and 4.5.11 show the normalized and unnormalized Uv-vis spectra, respectively. Already in the second amount with streptavidin, detectable changes have occurred. The largest induced shift at 13 nm in longitudinal peak is found at 75 nM Streptavidin concentration, see Figure 4.5.12. When more streptavidin

is added, the LSPR peaks shift back, explained by the different modes of interaction discussed in the theoretical framework, Figure 2.4.4.

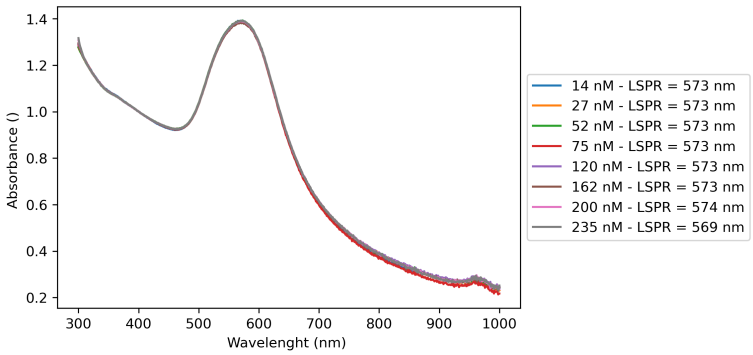

Figure 4.5.8: Normalized absorbance spectra of Biotynelated Citrate@Au NSs with increasing amounts of Streptavidin.

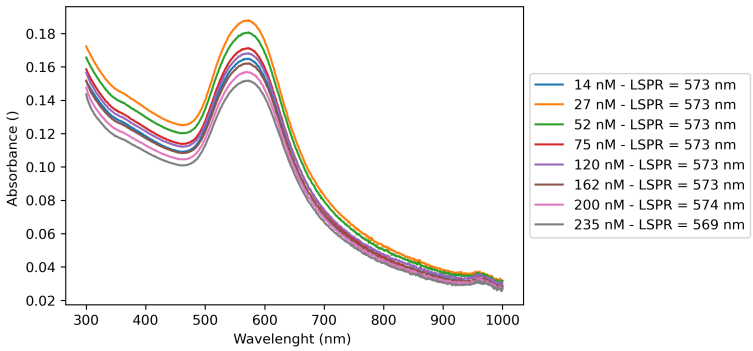

Figure 4.5.9: Unnormalized absorbance spectra of Biotynelated Citrate@Au NSs with increasing amounts of Streptavidin.

Aslan et al.[65] does multiple experiments with this model biosensing system, concluding that aggregation is dependent on the concentrations of streptavidin, biotinylated gold nanoparticles, and the surface mole fraction of biotin groups on the nanoparticles. Comparable experiments are done by adding increasing amounts of streptavidin, 4–200 nM, to 0.80 nM biotinylated Au NSs. Their work finds a shift from 531 nm to 538 nm upon the addition of 8.0 nM streptavidin. The largest shift was found with the addition of 24 nM, from 530 nm to 560 nm.

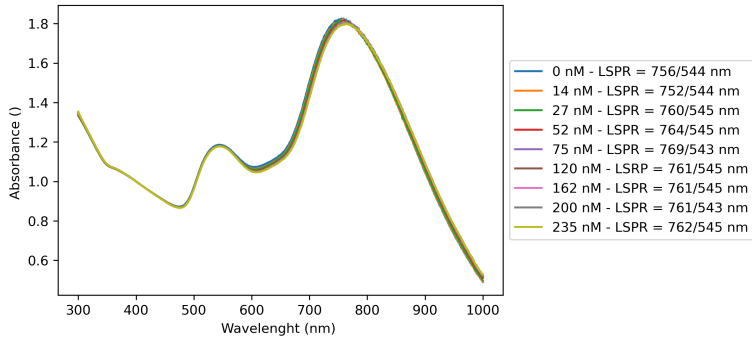

Figure 4.5.10: Normalized absorbance spectra of BiotynelatedAu NRs with increasing amounts of Streptavidin.

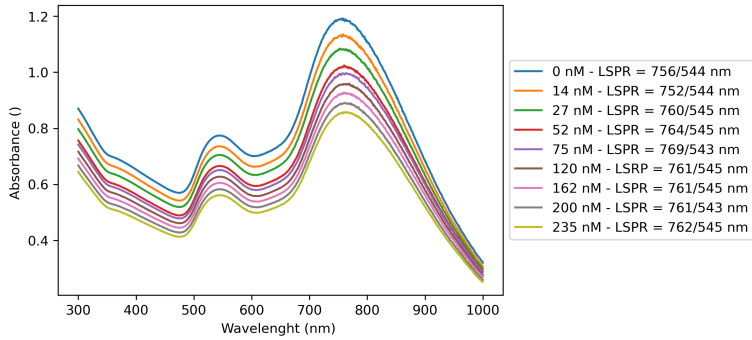

Figure 4.5.11: Unnormalized absorbance spectra of BiotynelatedAu NRs with increasing amounts of Streptavidin.

Aslan's results show significantly larger shifts, and at lower Streptavdin concentration. Especially the difference between no noticeable aggregation in the NSs of our results, Figure 4.5.8, and Aslan's 30 nm shift is striking. There can be many reasons for these differences. First, the biotinylated Au NSs in our study already have a starting LSPR peak position at 560 nm. The broadening and redshift in LSPR-peak upon aggregation come from the electronic coupling of two or more individual NPs. After the coupling, the electric field oscillations of the LSPR-phenomenon will shift frequency where it occurs. The lack in sensitivity for the Au NSs could, therefore, either come from already existing aggregation in the sample, polydispersity in the sample, or less sensitive peak positions. Less available biotin groups on the surface are also a probable reason.

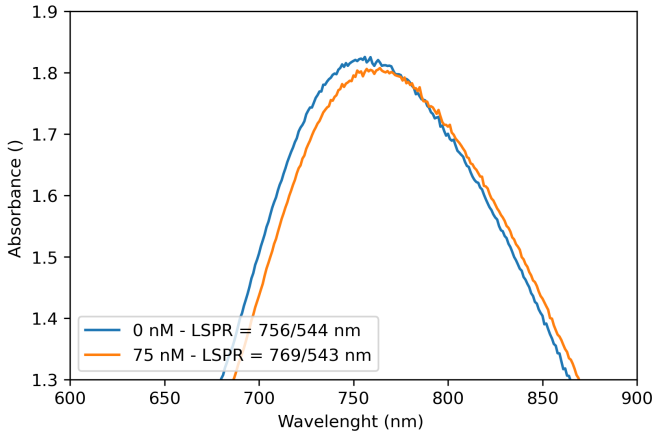

Figure 4.5.12: The largest LSPR shift is found when 75 nM Streptavidin was added to Biotynelated Au NRs.

The Au NRs show a noticeable shift in the absorbance spectra. However, also this induced shift in LSPR position is significantly lower than what was found in Aslan et al.s study. As discussed in the theoretical framework, the sensitivity of the refractive index increase as the Au NPs elongate, and especially the longitudinal peaks of Au NRs show sensitive properties. This can be a probable explanation both why the large difference is found between the two peaks for the Au NRs, but also why aggregation was visible for Au NRs, but not for Au NSs.

Ultimately this study shows that there is remaining work to be done to optimize the model biosensing system for PEG/MUA functionalized Au NPs. However, the visible aggregation in the Au NRs indicates that the system can be a valuable tool for testing the refractive index sensitivity of Au NPs with carboxyl groups on the surface.

5 Conclusions

The overall aim of this thesis was to learn more about shape dependency in the surface functionalization of Au NPs. This was done through an experimental approach.

First, five different shaped of Au NPs were synthesized and characterized through the well-known methods of seed-mediated growth and Turkevich synthesis routes. The NPs showed distinct LSPR-peaks, and zeta potentials indicated good colloidal stability.

Characterization of Au Concentration was then studied. Reproducibility and resolution in MP-AES measurements had been of concern. When three parallels were conducted for four samples of various shapes and polydispersity, the obtained Au concentrations showed a maximum standard deviation of 0.01 mg/ml.

Next, different published methods to determine Au Concentration via UV-vis were tested through an experimental approach. The study indicated that no universal method exists. However, NPs with similar sizes and surface chemistry have concentrations close to proportional to absorbance at 400nm. The lowest uncertainty was found when absorbance at 400 nm of digested citrate-coated Au NPs was measured.

To learn about the hydrodynamic diameter of anisotropic Au NPs, two Au NRs were measured at various dilutions and detection angles. The short study came to the conclusion that it is crucial to get to know the sample of interest and that sample stability is key to having high reproducibility in measurement.

PEG and MUA functionalization protocols were optimized and checked for reproducibility using Au NRs. Different amounts of the chemicals were tested, and the highest stability and yield were found using 2.56 mg/ml PEG and 20 mM MUA. These conditions were applied to the five Au NPs, and no clear shape dependencies were found. All the Au NPs kept their optical properties upon functionalizing with PEG in the first step. The second step, functionalizing with MUA, resulted in a broadening of the absorbance spectra for all samples. The question is whether it is possible to better preserve absorbance spectra or if the different axes of rotations due to anisotropy,

non-uniform coating, size enlargement, and the polydispersity of the samples make it impossible, was discussed. Further studies of colloidal stability, the reactivity of carboxy groups, and sonication methods were suggested.

Lastly, the Au NPs were biotinylated, and biotinylated Au NSs and Au NRs were applied in a model biosensing with streptavidin. Best results for biotinylation were found using long incubation times after Hinman et al.[67]. Compared to the literature, a significant redshift upon cleaning with buffer was noticed, and the importance of improving colloidal stability in this protocol step was pointed out. The biotinylated Au NSs showed no signs of aggregation with increasing amounts of streptavidin. In contrast, the Biotynelated Au NRs showed a maximum shift of 13 nm in longitudinal peak position when 75 nM Streptavidin was added. The study showed a lower performance compared to Aslan et al.[65], and it was discussed that already existing aggregation, polydispersity, or less available biotin groups on the surface could be reasons for this. However, it was concluded that the visible aggregation in the Au NRs indicates that the system can be a valuable tool for testing the refractive index sensitivity of any Au NPs with carboxyl groups on the surface if further optimized.

Bibliography

[1] WHO Coronavirus (COVID-19) Dashboard | WHO Coronavirus (COVID-19) Dashboard With Vaccination Data.

[2] Anthony Terriau, Julien Albertini, Emmanuel Montassier, Arthur Poirier, and Quentin Le Bastard. Estimating the impact of virus testing strategies on the COVID-19 case fatality rate using fixed-effects models. *Scientific Reports*, 11(1), 11 2021.

[3] Borja Sepúlveda, Paula C. Angelomé, Laura M. Lechuga, and Luis M. Liz-Marzán. LSPR-based nanobiosensors. *Nano Today*, 4(3):244–251, 6 2009.

[4] Nikhil Bhalla, Pawan Jolly, Nello Formisano, and Pedro Estrela. Introduction to biosensors. *Essays in Biochemistry*, 60(1), 6 2016.

[5] Sulalit Bandyopadhyay. *Fabrication and Application of Nanomaterials*. McGraw-Hill Education, New York, 1st ed. edition, 5 2019.

[6] Siyao Liu and Michael Lämmerhofer. Functionalized gold nanoparticles for sample preparation: A review, 9 2019.

[7] Jie Cao, Tong Sun, and Kenneth T.V. Grattan. Gold nanorod-based localized surface plasmon resonance biosensors: A review. *Sensors and Actuators, B: Chemical*, 195:332–351, 2014.

[8] Samuel E. Lohse, Nathan D. Burrows, Leonardo Scarabelli, Luis M. Liz-Marzán, and Catherine J. Murphy. Anisotropic Noble Metal Nanocrystal Growth: The Role of Halides. *Chemistry of Materials*, 26(1):34–43, 1 2013.

[9] Sulalit Bandyopadhyay, Gurvinder Singh, and Wilhelm Robert Glomm. Shape tunable synthesis of anisotropic gold nanostructures through binary surfactant mixtures. *Materials Today Chemistry*, 3:1–9, 3 2017.

[10] Sandeep Ghosh and Liberato Manna. The Many "Facets" of Halide Ions in the Chemistry of Colloidal Inorganic Nanocrystals. *Chemical Reviews*, 118(16):7804–7864, 8 2018.

[11] Catherine J. Murphy, Anand M. Gole, Simona E. Hunyadi, John W. Stone, Patrick N. Sisco, Alaaldin Alkilany, Brian E. Kinard, and Patrick Hankins. Chemical sensing and imaging with metallic nanorods. *Chemical Communications*, 8(5):544–557, 1 2008.

[12] Nguyen T.K. Thanh, N. Maclean, and S. Mahiddine. Mechanisms of nucleation and growth of nanoparticles in solution. *Chemical Reviews*, 114(15):7610–7630, 2014.

[13] Joel Harper-Harris, Krishna Kant, and Gurvinder Singh. Oleic Acid-Assisted Synthesis of Tunable High-Aspect-Ratio Multiply-Twinned Gold Nanorods for Bioimaging. *ACS Applied Nano Materials*, 4(4):3325–3330, 4 2021.

[14] Linfeng Gou and Catherine J. Murphy. Fine-tuning the shape of gold nanorods. *Chemistry of Materials*, 17(14):3668–3672, 7 2005.

[15] Leonid Vigderman and Eugene R. Zubarev. High-yield synthesis of gold nanorods with longitudinal SPR peak greater than 1200 nm using hydroquinone as a reducing agent. *Chemistry of Materials*, 2013.

[16] Leonardo Scarabelli, Marc Coronado-Puchau, Juan J Giner-Casares, Judith Langer, and Luis M Liz-Marzán. Monodisperse Gold Nanotriangles: Size Control, Large-Scale Self-Assembly, and Performance in Surface-Enhanced Raman Scattering. *ACS Nano*, 8(6):5833–5842, 6 2014.

[17] Gurvinder Singh, Antonius T J van Helvoort, Sulalit Bandyopadhyay, Sondre Volden, Jens-Petter Andreassen, and Wilhelm R Glomm. Synthesis of Au nanowires with controlled morphological and structural characteristics. *Applied Surface Science*, 311:780–788, 2014.

[18] Sulalit Bandyopadhyay, Birgitte H. McDonagh, Gurvinder Singh, Karthik Raghunathan, Axel Sandvig, Ioanna Sandvig, Jens Petter Andreassen, and Wilhelm R. Glomm. Growing gold nanostructures for shape-selective cellular uptake. *Nanoscale Research Letters*, 13, 2018.

[19] Muniyandi Jeyaraj, Sangiliyandi Gurunathan, Muhammad Qasim, Min-Hee Kang, and Jin-Hoi Kim. A Comprehensive Review on the Synthesis, Characterization,

and Biomedical Application of Platinum Nanoparticles. *Nanomaterials*, 9(12), 2019.

[20] Astrid Prestegård. Growing Anisotropic Plasmonic Nanoiparticles for Biosensing Applications. Technical report, NTNU, Trondheim, 2021.

[21] Werner Mäntele and Erhan Deniz. UV–VIS absorption spectroscopy: Lambert-Beer reloaded. *Spectrochimica Acta Part A: Molecular and Biomolecular Spectroscopy*, 173:965–968, 2 2017.

[22] Alexander G. Shard, Louise Wright, and Caterina Minelli. Robust and accurate measurements of gold nanoparticle concentrations using UV-visible spectrophotometry. *Biointerphases*, 13(6):061002, 11 2018.

[23] Caterina Minelli, Magdalena Wywijas, Dorota Bartczak, Susana Cuello-Nuñez, Heidi Goenaga Infante, Jerome Deumer, Christian Gollwitzer, Michael Krumrey, Karen E Murphy, Monique E Johnson, Antonio R Montoro Bustos, Ingo H Strenge, Bertrand Faure, Peter Høghøj, Vivian Tong, Loïc Burr, Karin Norling, Fredrik Höök, Matthias Roesslein, Jovana Kocic, Lyndsey Hendriks, Vikram Kestens, Yannic Ramaye, Maria C Contreras Lopez, Guy Auclair, Dora Mehn, Douglas Gilliland, Annegret Potthoff, Kathrin Oelschlägel, Jutta Tentschert, Harald Jungnickel, Benjamin C Krause, Yves U Hachenberger, Philipp Reichardt, Andreas Luch, Thomas E Whittaker, Molly M Stevens, Shalini Gupta, Akash Singh, Fang-hsin Lin, Yi-Hung Liu, Anna Luisa Costa, Carlo Baldisserri, Rid Jawad, Samir E L Andaloussi, Margaret N Holme, Tae Geol Lee, Minjeong Kwak, Jaeseok Kim, Johanna Ziebel, Cedric Guignard, Sebastien Cambier, Servane Contal, Arno C Gutleb, Jan "Kuba" Tatarkiewicz, Bartłomiej J Jankiewicz, Bartosz Bartosewicz, Xiaochun Wu, Jeffrey A Fagan, Elisabeth Elje, Elise Rundén-Pran, Maria Dusinska, Inder Preet Kaur, David Price, Ian Nesbitt, Sarah O' Reilly, Ruud J B Peters, Guillaume Bucher, Dennis Coleman, Angela J Harrison, Antoine Ghanem, Anne Gering, Eileen McCarron, Niamh Fitzgerald, Geert Cornelis, Jani Tuoriniemi, Midori Sakai, Hidehisa Tsuchida, Ciarán Maguire, Adriele Prina-Mello, Alan J Lawlor, Jessica Adams, Carolin L Schultz, Doru Constantin, Nguyen Thi Kim Thanh, Le Duc Tung, Luca Panariello, Spyridon Damilos, Asterios Gavriilidis, Iseult Lynch, Benjamin Fryer, Ana Carrazco Quevedo, Emily Guggenheim, Sophie Briffa, Eugenia Valsami-Jones, Yuxiong Huang, Arturo A Keller, Virva-Tuuli Kinnunen, Siiri Perämäki, Zeljka Krpetic, Michael Greenwood, and Alexander G Shard. Versailles project on advanced materials and standards (VAMAS) interlaboratory study on measuring the number

concentration of colloidal gold nanoparticles. *Nanoscale*, 14(12):4690–4704, 2022.

[24] Wolfgang Haiss, Nguyen T K Thanh, Jenny Aveyard, and David G Fernig. Determination of Size and Concentration of Gold Nanoparticles from UV–Vis Spectra. *Analytical Chemistry*, 79(11):4215–4221, 6 2007.

[25] Nikolai G Khlebtsov. Determination of Size and Concentration of Gold Nanoparticles from Extinction Spectra. *Analytical Chemistry*, 80(17):6620–6625, 9 2008.

[26] Thomas Hendel, Maria Wuithschick, Frieder Kettemann, Alexander Birnbaum, Klaus Rademann, and Jörg Polte. In Situ Determination of Colloidal Gold Concentrations with UV–Vis Spectroscopy: Limitations and Perspectives. *Analytical Chemistry*, 86(22):11115–11124, 11 2014.

[27] Leonardo Scarabelli, Ana Sánchez-Iglesias, Jorge Pérez-Juste, and Luis M. Liz-Marzán. A "Tips and Tricks" Practical Guide to the Synthesis of Gold Nanorods. *Journal of Physical Chemistry Letters*, 6(21):4270–4279, 11 2015.

[28] Alexander G Shard, Louise Wright, and Caterina Minelli. Robust and accurate measurements of gold nanoparticle concentrations using UV-visible spectrophotometry. *Biointerphases*, 13(6):61002, 2018.

[29] Lucien Roach, P Louise Coletta, Kevin Critchley, and Stephen D Evans. Controlling the Optical Properties of Gold Nanorods in One-Pot Syntheses. *The Journal of Physical Chemistry C*, 126(6):3235–3243, 2 2022.

[30] Wolfram Hergert. Gustav Mie: From Electromagnetic Scattering to an Electromagnetic View of Matter. In Wolfram Hergert and Thomas Wriedt, editors, *The Mie Theory: Basics and Applications*, pages 1–51. Springer Berlin Heidelberg, Berlin, Heidelberg, 2012.

[31] Jan Mast, Eveline Verleysen, Vasile-Dan Hodoroaba, and Ralf Kaegi. Chapter 2.1.2 - Characterization of nanomaterials by transmission electron microscopy: Measurement procedures. In Vasile-Dan Hodoroaba, Wolfgang E S Unger, and Alexander G Shard, editors, *Characterization of Nanoparticles*, Micro and Nano Technologies, pages 29–48. Elsevier, 2020.

[32] E Buhr, N Senftleben, T Klein, D Bergmann, D Gnieser, C G Frase, and H Bosse. Characterization of nanoparticles by scanning electron microscopy in transmission mode. *Measurement Science and Technology*, 20(8):84025, 6 2009.

[33] Leonardo Scarabelli, Marek Grzelczak, and Luis M. Liz-Marzán. Tuning gold nanorod synthesis through prereduction with salicylic acid. *Chemistry of Materials*, 2013.

[34] Alexander Bootz, Vitali Vogel, Dieter Schubert, and Jörg Kreuter. Comparison of scanning electron microscopy, dynamic light scattering and analytical ultracentrifugation for the sizing of poly(butyl cyanoacrylate) nanoparticles. *European Journal of Pharmaceutics and Biopharmaceutics*, 57(2):369–375, 2004.

[35] Jake Austin and MalvernPanalytical. Dynamic-light-scattering-.

[36] Jake Austin, Caterina Minelli, Douglas Hamilton, Magdalena Wywijas, and Hanna Jankevics Jones. Nanoparticle number concentration measurements by multi-angle dynamic light scattering. *Journal of Nanoparticle Research*, 22(5):108, 2020.

[37] J Doak, R K Gupta, K Manivannan, K Ghosh, and P K Kahol. Effect of particle size distributions on absorbance spectra of gold nanoparticles. *Physica E: Low-dimensional Systems and Nanostructures*, 42(5):1605–1609, 2010.

[38] Frank Babick. Chapter 3.2.1 - Dynamic light scattering (DLS). In Vasile-Dan Hodoroaba, Wolfgang E S Unger, and Alexander G Shard, editors, *Characterization of Nanoparticles*, Micro and Nano Technologies, pages 137–172. Elsevier, 2020.

[39] Ming Xu, Mahmoud G Soliman, Xing Sun, Beatriz Pelaz, Neus Feliu, Wolfgang J Parak, and Sijin Liu. How Entanglement of Different Physicochemical Properties Complicates the Prediction of in Vitro and in Vivo Interactions of Gold Nanoparticles. *ACS Nano*, 12(10):10104–10113, 10 2018.

[40] Jeffrey Bodycomb. Interpreting and Understanding Dynamic Light Scattering Size Data.

[41] Andrei S Dukhin and Renliang Xu. Chapter 3.2.5 - Zeta-potential measurements. In Vasile-Dan Hodoroaba, Wolfgang E S Unger, and Alexander G Shard, editors, *Characterization of Nanoparticles*, Micro and Nano Technologies, pages 213–224. Elsevier, 2020.

[42] K Pate and P Safier. 12 - Chemical metrology methods for CMP quality. In Suryadevara Babu, editor, *Advances in Chemical Mechanical Planarization (CMP)*, pages 299–325. Woodhead Publishing, 2016.

[43] Fanny Varenne, Jérémie Botton, Claire Merlet, Jean Jacques Vachon, Sandrine Geiger, Ingrid C. Infante, Mohamed M. Chehimi, and Christine Vauthier. Standardization and validation of a protocol of zeta potential measurements by electrophoretic light scattering for nanomaterial characterization. *Colloids and Surfaces A: Physicochemical and Engineering Aspects*, 486:218–231, 12 2015.

[44] Bob Carr and Matthew Wright. Nanoparticle Tracking Analysis; A Review of Applications and Usage in the Analysis of Exosomes and Microvesicles Applications of NTA in Exosomes Research.

[45] Vasco Filipe, Andrea Hawe, and Wim Jiskoot. Critical Evaluation of Nanoparticle Tracking Analysis (NTA) by NanoSight for the Measurement of Nanoparticles and Protein Aggregates. *Pharmaceutical Research*, 27(5):796–810, 2010.

[46] Patrick Hole. Chapter 3.1.2 - Particle Tracking Analysis (PTA). In Vasile-Dan Hodoroaba, Wolfgang E S Unger, and Alexander G Shard, editors, *Characterization of Nanoparticles*, Micro and Nano Technologies, pages 79–96. Elsevier, 2020.

[47] V Balaram. Microwave plasma atomic emission spectrometry (MP-AES) and its applications – A critical review. *Microchemical Journal*, 159:105483, 2020.

[48] AGILENT TECHNOLOGIES. Microwave Plasma Atomic Emission Spectroscopy (MP-AES) - Application eHandbook, 2021.

[49] Wei Li, Patrick Simmons, Doug Shrader, Timothy J Herrman, and Susie Y Dai. Microwave plasma-atomic emission spectroscopy as a tool for the determination of copper, iron, manganese and zinc in animal feed and fertilizer. *Talanta*, 112:43–48, 2013.

[50] Stefan Karlsson, Viktor Sjöberg, and Anna Ogar. Comparison of MP AES and ICP-MS for analysis of principal and selected trace elements in nitric acid digests of sunflower (Helianthus annuus). *Talanta*, 135:124–132, 2015.

[51] Jiangjiang Zhang, Lei Mou, and Xingyu Jiang. Surface chemistry of gold nanoparticles for health-related applications. *Chemical Science*, 11(4):923–936, 1 2020.

[52] Jinfeng Liao, Taorang Tian, Sirong Shi, Xueping Xie, Shuanglin Peng, Ying Zhu, Jingang Xiao, and Yunfeng Lin. Broadening the biocompatibility of gold nanorods from rat to Macaca fascicularis: advancing clinical potential. *Journal of Nanobiotechnology*, 19(1):195, 2021.

[53] Xin Shi, Hannah L Perry, and James D E T Wilton-Ely. Strategies for the functionalisation of gold nanorods to reduce toxicity and aid clinical translation. *Nanotheranostics*, 5:155–165, 2021.

[54] Xiaohua Huang, Svetlana Neretina, and Mostafa A El-Sayed. Gold Nanorods: From Synthesis and Properties to Biological and Biomedical Applications. *Advanced Materials*, 21(48):4880–4910, 2009.

[55] Qiu Dai, Janelle Coutts, Jianhua Zou, and Qun Huo. Surface modification of gold nanorods through a place exchange reaction inside an ionic exchange resin. *Chem. Commun.*, (25):2858–2860, 2008.

[56] Jie Cao, Ewan K Galbraith, Tong Sun, and Kenneth T V Grattan. Effective surface modification of gold nanorods for localized surface plasmon resonance-based biosensors. *Sensors and Actuators B: Chemical*, 169:360–367, 2012.

[57] Benjamin Thierry, Jane Ng, Tina Krieg, and Hans J. Griesser. A robust procedure for the functionalization of gold nanorods and noble metal nanoparticles. *Chemical Communications*, (13):1724–1726, 3 2009.

[58] Xiaohu Xia, Miaoxin Yang, Yucai Wang, Yiqun Zheng, Qingge Li, Jingyi Chen, and Younan Xia. Quantifying the Coverage Density of Poly(ethylene glycol) Chains on the Surface of Gold Nanostructures. *ACS Nano*, 6(1):512–522, 1 2012.

[59] Elif Burcu Aydın, Muhammet Aydın, and Mustafa Kemal Sezgintürk. Biosensors and the evaluation of food contaminant biosensors in terms of their performance criteria. *International Journal of Environmental Analytical Chemistry*, 100(5):602–622, 2020.

[60] Rhishikesh Mandke, Buddhadev Layek, Gitanjali Sharma, and Jagdish Singh. Fabrication and Evaluation of Nanoparticle-Based Biosensors. In *Biosensor Nanomaterials*, chapter 4, pages 73–93. John Wiley & Sons, Ltd, 2011.

[61] Parikshit Moitra, Maha Alafeef, Ketan Dighe, Matthew B Frieman, and Dipanjan Pan. Selective Naked-Eye Detection of SARS-CoV-2 Mediated by N Gene Targeted Antisense Oligonucleotide Capped Plasmonic Nanoparticles. *ACS nano*, 14(6):7617–7627, 6 2020.

[62] Huanjun Chen, Xiaoshan Kou, Zhi Yang, Weihai Ni, and Jianfang Wang. Shape- and Size-Dependent Refractive Index Sensitivity of Gold Nanoparticles. *Langmuir*, 24(10):5233–5237, 5 2008.

[63] Hemant Ramakant Hegde, Santhosh Chidangil, and Rajeev K Sinha. Refractive index sensitivity of Au nanostructures in solution and on the substrate. *Journal of Materials Science: Materials in Electronics*, 33(7):4011–4024, 2022.

[64] Nidhi Nath and Ashutosh Chilkoti. A Colorimetric Gold Nanoparticle Sensor To Interrogate Biomolecular Interactions in Real Time on a Surface. *Analytical Chemistry*, 74(3):504–509, 2 2002.

[65] Kadir Aslan, Claudia C Luhrs, and Víctor H Pérez-Luna. Controlled and Reversible Aggregation of Biotinylated Gold Nanoparticles with Streptavidin. *The Journal of Physical Chemistry B*, 108(40):15631–15639, 10 2004.

[66] Maria Wuithschick, Alexander Birnbaum, Steffen Witte, Michael Sztucki, Ulla Vainio, Nicola Pinna, Klaus Rademann, Franziska Emmerling, Ralph Kraehnert, and Jörg Polte. Turkevich in New Robes: Key Questions Answered for the Most Common Gold Nanoparticle Synthesis. *ACS Nano*, 9(7):7052–7071, 7 2015.

[67] Samuel S Hinman, Kristy S McKeating, and Quan Cheng. DNA Linkers and Diluents for Ultrastable Gold Nanoparticle Bioconjugates in Multiplexed Assay Development. *Analytical Chemistry*, 89(7):4272–4279, 4 2017.

[68] Tina Maria Bruns. Quantifying Growth of Anisotropic Gold Nanoparticles and Understanding Growth Mechanisms, 2021.

[69] Li Shi, Eric Buhler, François Boué, and Florent Carn. How does the size of gold nanoparticles depend on citrate to gold ratio in Turkevich synthesis? Final answer to a debated question. *Journal of Colloid and Interface Science*, 492:191–198, 2017.

[70] Samuel E Lohse and Catherine J Murphy. The Quest for Shape Control: A History of Gold Nanorod Synthesis. *Chemistry of Materials*, 25:1250–1261, 2013.

[71] Astrid Prestegård. Growing Anisotropic Gold nanostructures, 2021.

[72] Furong Tian, Franck Bonnier, Alan Casey, Anne E Shanahan, and Hugh J Byrne. Surface enhanced Raman scattering with gold nanoparticles: effect of particle shape. *Anal. Methods*, 6(22):9116–9123, 2014.

[73] Richard Becker, Bo Liedberg, and Per-Olov Käll. CTAB promoted synthesis of Au nanorods – Temperature effects and stability considerations. *Journal of Colloid and Interface Science*, 343(1):25–30, 2010.

[74] Ratna Tantra, Philipp Schulze, and Paul Quincey. Effect of nanoparticle concentration on zeta-potential measurement results and reproducibility. *Particuology*, 8(3):279–285, 2010.

[75] Yan Peng Jia, Kun Shi, Jin Feng Liao, Jin Rong Peng, Ying Hao, Ying Qu, Li Juan Chen, Li Liu, Xia Yuan, Zhi Yong Qian, and Xia Wei Wei. Effects of Cetyltrimethylammonium Bromide on the Toxicity of Gold Nanorods Both In Vitro and In Vivo: Molecular Origin of Cytotoxicity and Inflammation. *Small Methods*, 4(3):1900799, 2020.

[76] Maurice Retout, Pascale Blond, Ivan Jabin, and Gilles Bruylants. Ultrastable PEGylated Calixarene-Coated Gold Nanoparticles with a Tunable Bioconjugation Density for Biosensing Applications. *Bioconjugate Chemistry*, 32(2):290–300, 2 2021.

[77] Calum Kinnear, Hervé Dietsch, Martin J D Clift, Carola Endes, Barbara Rothen-Rutishauser, and Alke Petri-Fink. Gold Nanorods: Controlling Their Surface Chemistry and Complete Detoxification by a Two-Step Place Exchange. *Angewandte Chemie International Edition*, 52(7):1934–1938, 2013.

[78] Kadir Aslan and Víctor H Pérez-Luna. Surface Modification of Colloidal Gold by Chemisorption of Alkanethiols in the Presence of a Nonionic Surfactant. *Langmuir*, 18(16):6059–6065, 8 2002.

A | S(T)EM size

S(T)EM imaging and imageJ image processing software were used, as described in section 3.5.2 to find S(T)EM-size. This Appendix presents the images used, and the resulting histograms of these measurments. Diameter was measured for spherical structures (Citrate@Au NSs, CTAB@Au NSs, and CTAB@Au NPs spiky). Rods(CTAB@Au NRs OA and CTAB@Au NRs TA) were measured with major and minor axis. Aspect ratio were found dividing lenght of major axis by lenght of minor axis.

A.1 Citrate@Au NSs

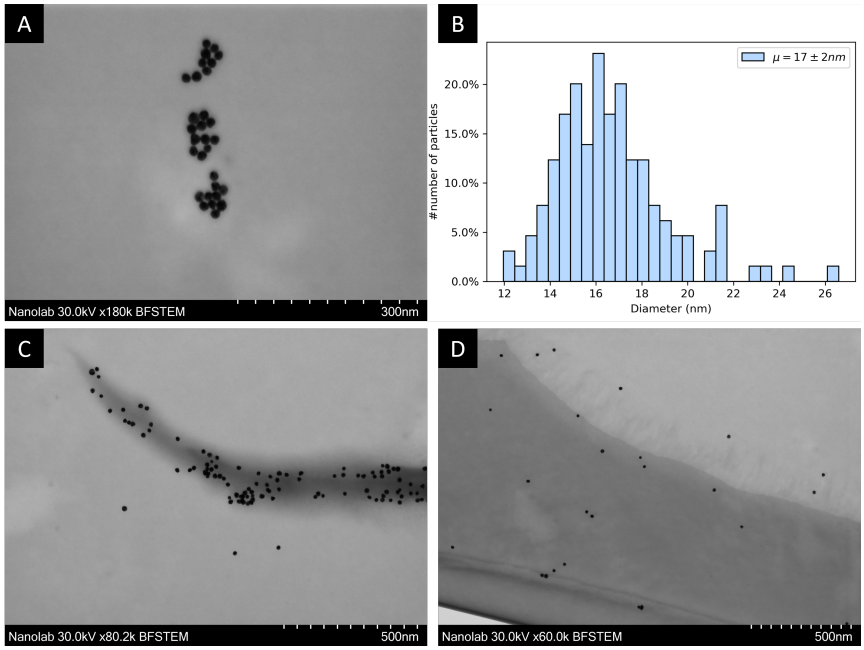

Figure A.1.1: 135 particles, 29 from image A, 82 from image C and 23 from image D, were measured to find STEM-size of Citrate coated Nanospheres. Figure B show the resulting histogram of measured diameter. Average diameter was found to be 17 ± 2 nm.

A.2 CTAB@Au NSs

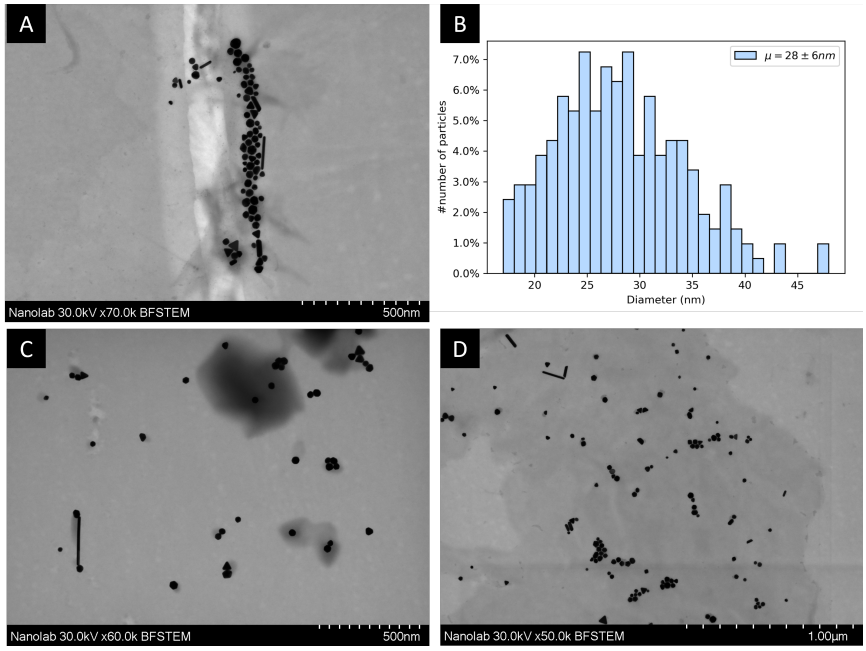

Figure A.2.1: 203 particles, 33 from image A, 67 from image C and 103 from image D, were measured to find STEM-size of Citrate coated Nanospheres. Figure B show the resulting histogram of measured diameter. Average diameter was found to be 28 ± 6 nm.

A.3 CTAB@Au NRs OA

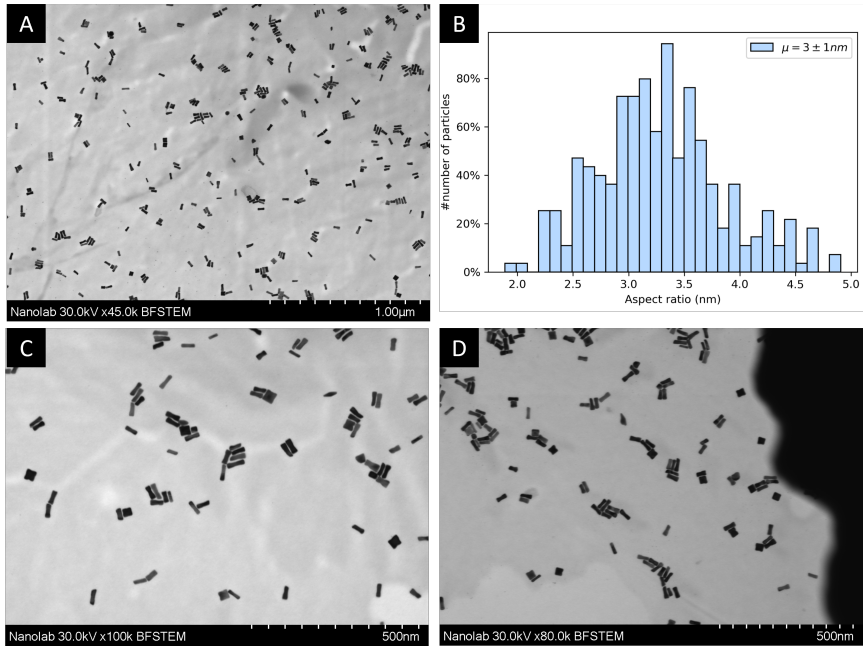

Figure A.3.1: 275 particles, 139 from image A, 58 from image C and 78 from image D, were measured to find STEM-size of CTAB coated OA Nanorods. Figure B show the resulting histogram of measured aspect ratio. Average major axis was 43 ± 5 nm and average minor axis was 13 ± 2 nm, giving a resulting average aspect ratio of 3 ± 1 nm.

A.4 CTAB@Au NRs TA

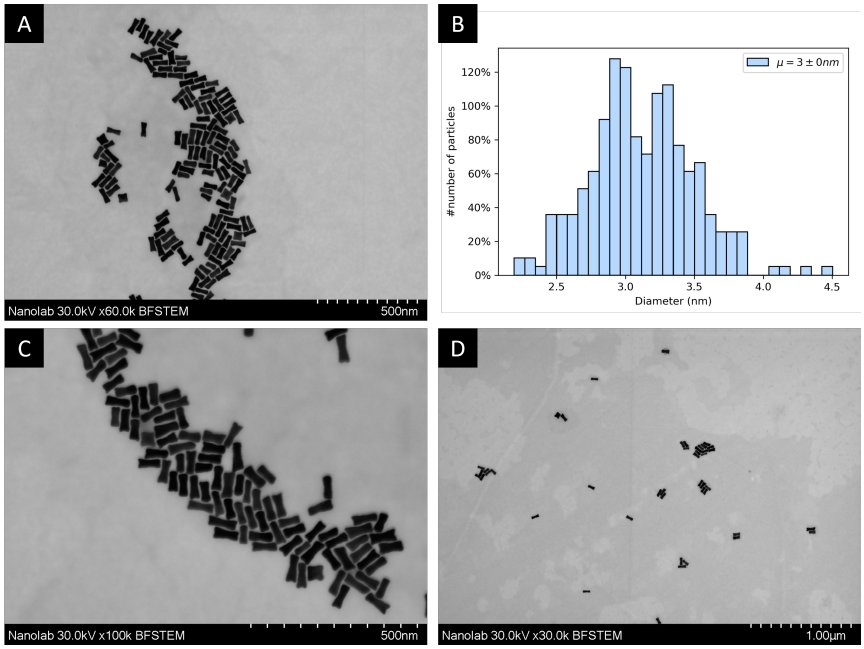

Figure A.4.1: 274 particles, 133 from image A, 81 from image C and 60 from image D, were measured to find STEM-size of CTAB@Au NRs TA. Figure B show the resulting histogram of measured aspect ratio. Average major axis was 70 ± 7 nm and average minor axis was 23 ± 3 nm, giving a resulting average aspect ratio of 3 ± 0 nm.

A.5 CTAB@Au NPs spiky

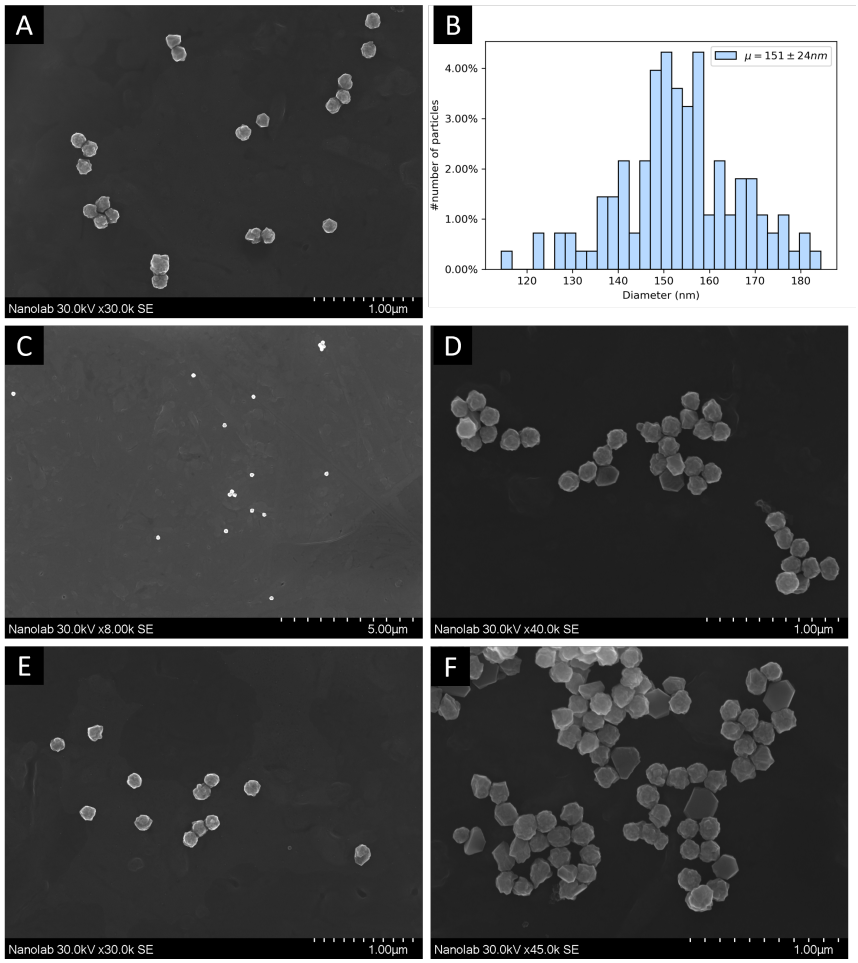

Figure A.5.1: 153 particles, 21 from image A, 15 from image C and 29 from image D, 12 from image E and 47 from image F, were measured to find STEM-size of CTAB@Au NPs spiky. Figure B show the resulting histogram of measured diameter. Average diameter was found to 153 *pm* 13 nm.

B | Concentration with MP-AES

B.1 Protocol for Digestion of Au NPs with HSE-measures

This section is written for future use by Particle Engineering Reasearch Group. The protocol is presented in under, and the setup is shown in Figure B.1.1. OBS! warning, the acids used in this protocol are very strong, it is very important carefully to risk access this process before conducting it.

Prepare:

- Au NPs
- Small glass vials, ca 20 ml
- Clean empty oilbath(ca 1 per 4 samples)
- Acid gloves
- Nitric acid
- Hcl
- 2 x 5 ml pipettes (green)
- 1 x 1 ml pipette (blue)
- Glass beaker for waste filled half way with water

Digestion step:

- Do your standard vortex and zonication routine for even redispersion of NPs
- Into a small gass vial, add:

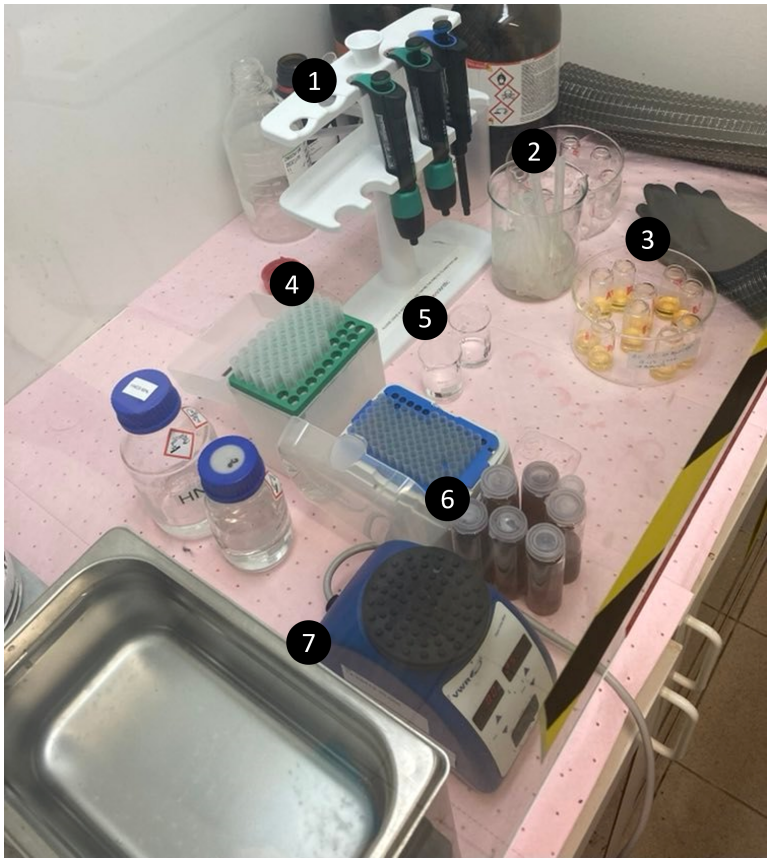

Figure B.1.1: Picture of the set up used for digestion of Au NPs. 1) is pipettes and pipette rack. 2) is waste beaker filled with water to dilute any excess acid in the pipette tips. 3) is empty oilbath for the samples to stand in. Any possible spills would end up in the glassware instead of in the lab. 4) pipette tips. 5) Beakers with HNO_3 and HCl. 6) Au NPs samples, and finally 7) Zonicator and vortex.

1. 3.4 ml HCl
2. 1.1 ml HNO_3
3. 0.5 ml NPs

⋆ Your pipette tips goes into the waste beaker with water)

⋆ Carefully place your small vials into the empty oil bath in the back of the fume hood. OBS! Fume hood needs to be closed the first 24 hours of digestion!!

⋆ Acid gloves can be washed as doing a normal handwash

- Let the particles digest for 24-48 hours

Step 2

- Add 15 ml MQ-water into each sample (= NPs in 1:40 dilution)
- The sample is know ready for MP-AES analysis

B.2 Tips for MP-AES measurments

The following list presents factors I struggeled with and found essential to get good MP - AES measurements.

- **Standards** - Choose your standards visely and evenly distributed linearly. Do not only make one single series dilution halfing the concentrations. I had good success with using 9 standards, made through two series dilutions, of concentration, 0, 0.38, 0.75, 1.13, 1.50, 2.25, 3.00, 4.50 and 6.00 mg/l
- **Sample concentration** - Samples should have concentrations in the middle of your standard-curve. Increasing the dilution to factor 100 can be a good option if samples are too concentrated
- **Settings to check on the MP-AES** :
  1. Pumping time - measurments are unsystematic if pumping time is to short. The whole sample volume must be pumped into the instrument.
  2. Cleanlyness - measurement have to low intensity if instrument is dirty. Be patient cleaning with 10 % HNO_3 before and after using the instrument. Look for droplets in the nebulizer, and contact engineer if any are obseved.

C | Surface Area Concentration

C.1 Geometrical Assumptions

Surface area concentrations and particle number concentrations were done using simple geometrical assumptions. Citrate@Au NSs, CTAB@Au NSs, and CTAB@Au NPs spiky were assumed to be the shape of a perfect sphere. Both CTAB@Au NRs were assumed the form of a perfect cylinder. Equations C.1 to C.4 is the equations of volume and surface area of the two shapes. d is the diameter of the sphere. a is the major axis, and b is the minor axis of the rod. Figure C.1.1 shows the resulting volumes for all shapes obtained with STEM and DLS measurements.

$$\text{Volume sphere} = \frac{4}{3}\pi(\frac{d}{2})^3 \tag{C.1}$$

$$\text{Surface area sphere} = 4\pi(\frac{d}{2})^2 \tag{C.2}$$

$$\text{Volume cylinder} = 2\pi(\frac{b}{2})^2 * a \tag{C.3}$$

$$\text{Surface area cylinder} = 2\pi(\frac{b}{2})^2 + 2\pi(\frac{b}{2}) * a \tag{C.4}$$

C.2 Surface Area Concentrations

Gold FCC cubic density at 19.3 kg/dm^3 and the following equations were used to find particle number concentrations with MP-AES methods. Surface area as found in the previous section were multiplied with particle number concentrations to find surface

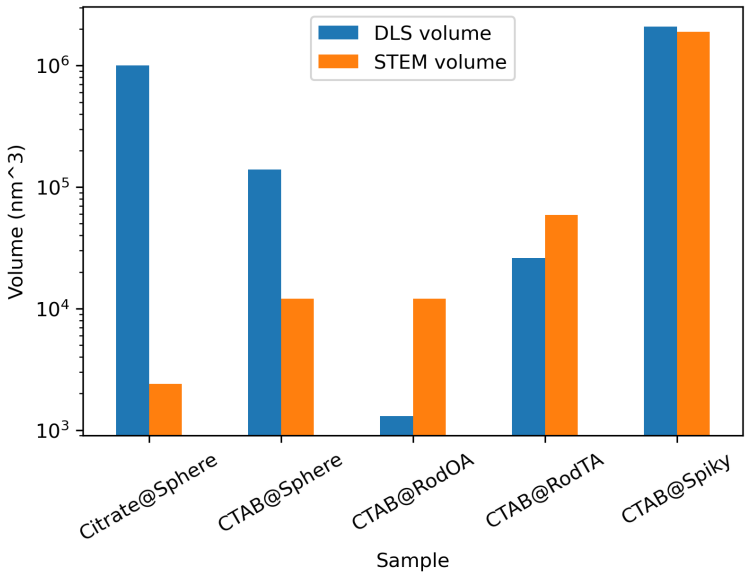

Figure C.1.1: Resulting volumes for all shapes obtained with STEM and DLS measurements.

area concentrations. Figure 4.2.2 showed the particle number concentrations, and Figure 4.2.2 showed resulting surface area concentrations.

$$\text{Particle weight} = volume * \text{FCC cubic density} \tag{C.1}$$

$$\#\text{Particles per ml} = \frac{\text{MP-AES concentration}}{\text{Particle weight}} \tag{C.2}$$

C.3 PEG chains per Surface Area

The PEG used in this thesis had molecular weight of 5000 Da. N_A is the Avogadro constant, $6.022 * 10^{23} mol^{-1}$. Added number of PEG chains per nm^2 is found using the following equations. Table 4.3 showed the results.

$$\#\text{ Added PEG chains} = \frac{\text{Added PEG (g)}}{\text{molecular weight (g/mol)}} N_A(\text{molecules/mol}) \tag{C.1}$$

$$\text{PEG chains per surface area} = \frac{\text{\# Added PEG chains}}{\text{surface area concentration}} \tag{C.2}$$

D | Au Concentration with UV-vis

This appendix presents an overview of the STEM sizes of the Au NPs used in the section reviewing methods for concentration with UV-vis. The experimental set used consists of the five different shapes synthesized for this thesis, six spherical citrate coated Au NPs with stepwise increasing sizes made in previous work[20], and three CTAB coated Au NRs from seed-mediated growth with TA from Tina Bruns Master Thesis[68] were used.

D.1 Characteristics of NPs

Figure D.1.1 show STEM size of the citrate coated Au NPs with stepwise increasing sizes. Figure D.1.2 show STEM sizes of the Au NRs made with TA.

D.2 Table of Results

Table D.1 presents all data used in the study. Samples 1-5, A1-A5 and B1-B5 correspond to 1- Citrate@Au NSs, 2-CTAB@Au NSs, 3-CTAB@Au NRs OA, 4-CTAB@Au NRs TA and 5-CTAB@Au NPs spiky. These were presented in Section 4.1. S1-S6 are Citrate Coated Au NPs with Stepwise Increasing Sizes, were S1-S5 correspons to steps 1-5, and S6 is step 0. K1-B1 - B3 are the CTAB coated rods made with TA.

Table D.1: All results used in section 2.1 review methods for to find Au concentration with UV-Vis.

	MP-AES			Uv-vis	
	Measured	Corrected for dilution		Digested Au NPs	NPs
	(mg/l)	(mg/ml)	mM	Abs400	Abs400
1	1.02E+00	4.08E-02	4.00E+01	2.61E-03	1.44E-01
2	6.40E-01	2.56E-02	2.51E+01	6.99E-03	2.35E-01
3	3.99E+00	1.60E-01	1.56E+02	1.33E-02	8.83E-01
4	4.77E+00	1.91E-01	1.87E+02	1.67E-02	8.88E-01
5	2.73E+00	1.09E-01	1.07E+02	1.00E-02	2.28E-01
A1	1.10E+00	4.40E-02	4.31E+01	1.78E-03	1.44E-01
A2	5.10E-01	2.04E-02	2.00E+01	6.21E-04	2.35E-01
A4	4.44E+00	1.78E-01	1.74E+02	9.94E-03	8.88E-01
A5	2.54E+00	1.02E-01	9.96E+01	4.86E-03	2.28E-01
B1	1.08E+00	4.32E-02	4.24E+01	1.71E-03	1.44E-01
B2	4.54E+00	1.82E-01	1.78E+02	2.42E-02	2.35E-01
B4	4.54E+00	1.82E-01	1.78E+02	9.50E-03	8.88E-01
B5	2.52E+00	1.01E-01	9.88E+01	5.76E-03	2.28E-01
S1	2.02E+00	8.08E-02	7.92E+01	3.82E-03	6.06E-02
S2	2.74E+00	1.10E-01	1.07E+02	5.57E-03	6.98E-02
S3	3.11E+00	1.24E-01	1.22E+02	6.33E-03	1.05E-01
S4	3.42E+00	1.37E-01	1.34E+02	6.27E-03	1.24E-01
S5	4.14E+00	1.66E-01	1.62E+02	8.07E-03	2.65E-01
S6	1.16E+00	4.64E-02	4.55E+01	1.67E-03	4.23E-02
K-B1	4.09E+00	1.64E-01	1.60E+02	2.49E-02	1.20E+00
K-B2	3.43E+00	1.37E-01	1.35E+02	2.04E-02	7.50E-01
K-B3	1.33E+00	5.32E-02	5.22E+01	8.06E-03	4.64E-01

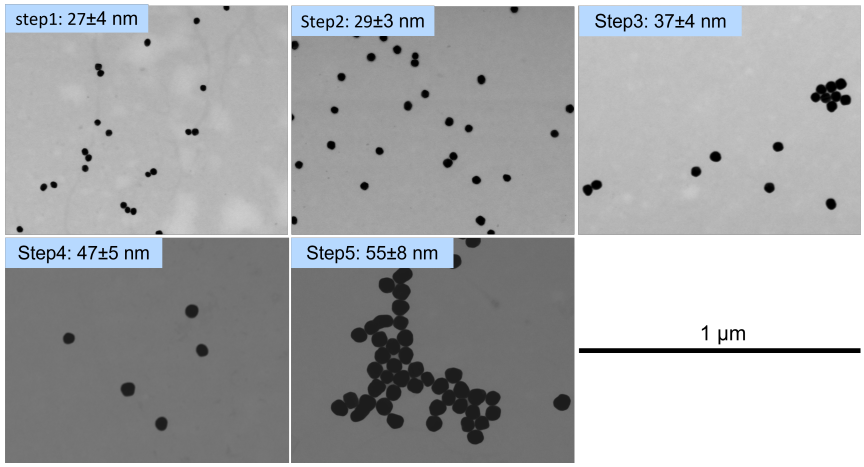

Figure D.1.1: STEM sizes of Citrate Coated Au NPs with Stepwise Increasing Sizes. Step 0 is Turkeivch NPs with size ca 17 nm. Image from [20].

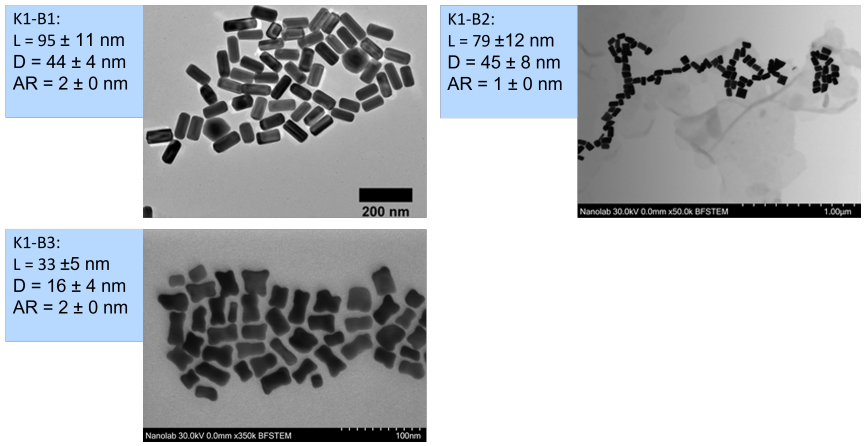

Figure D.1.2: STEM sizes of three CTAB coated Au NRs from seed-mediated growth with TA from Tina Bruns Master Thesis[68]. STEM imaging is from the previous reference.

Prestegård, Astrid

Shape Dependency in Functionalization of Gold Nanoparticles for Biosensing Applications

NTNU
Norwegian University of
Science and Technology